TECHNISCHE
UNIVERSITÄT
DARMSTADT

Physik

Limit Cycles in Quantum Systems

Vom Fachbereich Physik
der Technischen Universität Darmstadt

zur Erlangung des Grades
eines Doktors der Naturwissenschaften (Dr. rer. nat.)

genehmigte Dissertation von
Dipl.-Phys. Patrick Niemann
aus Emden

Darmstadt 2015
D17

Referent: Prof. Dr. Hans-Werner Hammer
Korreferent: Prof. Dr. Jens Braun

Tag der Einreichung: 22.1.2015
Tag der Prüfung: 27.4.2015

Zusammenfassung

In dieser Arbeit befassen wir uns mit *Grenzzyklen in Quantensystemen*. Grenzzyklen sind eine Topoplogie der Renormierungsgruppe (RG). Wenn Hochenergie-Freiheitsgrade ausintegriert werden, laufen die Kopplungskonstanten periodisch in einer geschlossenen Kurve. Grenzzyklen können allerdings auch auftreten, wenn Niederenergie-Freiheitsgrade ausintegriert werden. Eine notwendige Bedingung für das Auftreten von Grenzzyklen ist diskrete Skaleninvarianz. Eine Signatur der diskreten Skaleninvarianz und von Grenzzyklen ist logarithmisch-periodisches Verhalten.

Im ersten Teil dieser Arbeit untersuchen wir Grenzzyklen mit Hilfe der Ähnlichkeitsrenormierungsgruppe, im Englischen Similarity Renormalization Group (SRG) genannt. Grenzzyklen werden hauptsächlich mit Mitteln der konventionellen Renormierungsgruppe untersucht. Dabei werden Freiheitsgrade, die größer sind als ein zuvor festgelegter Cutoff, ausintegriert. Der Ansatz der SRG ist hingegen ein anderer. In der SRG werden Potentiale unitär transformiert und erhalten dabei eine banddiagonale Form. Die Breite der Bandstruktur kann dabei im Vergleich zur RG-Methode als eine andere Art von Cutoff angesehen werden.

Wir untersuchen das Auftreten von Grenzzyklen in der SRG-Entwicklung. Unser Ziel ist es dabei Signaturen des Grenzzyklus aus den entwickelten Potentialen sowie den Skalenfaktor zu extrahieren. Wir betrachten das $1/R^2$-Potential im Zweiteilchen-System sowie ein Dreiteilchen-System mit großer Streulänge. Beide Systeme weisen einen Grenzzyklus auf. Wir verwenden neben dem häufig genutzten kinetischen-Energie-Generator auch zwei weitere SRG-Generatoren, den exponentiellen und inversen Generator.

Der zweite Teil dieser Arbeit beschäftigt sich mit Grenzzyklen bei endlicher Dichte. Wir untersuchen dabei die Polstruktur der Streuamplitude für unterscheidbare Fermionen bei der Temperatur $T = 0$ im Medium. Unterschiedliche Massen der Fermionen werden ebenso angenommen wie eine vollständig gefüllte Fermikugel für jede Fermionensorte. Dabei konzentrieren wir uns auf den Bereich negativer Streulängen und den unitären Grenzfall. Wir diskutieren wie sich die Eigenschaften des Dreiteilchenspektrums verändern, wenn man anstatt des Vakuums eine endliche Dichte annimmt. Des Weiteren nutzen wir unsere Ergebnisse um Rückschlüsse auf die Phasenstruktur ultrakalter Fermigase zu ziehen.

Contents

1 Introduction

Universality is a fascinating topic in modern physics. It refers to physical systems with different short-range physics but which display identical behavior at large distances. Classically, universality is associated with phase transitions in condensed matter systems. A prominent example of universality is related to the behavior of liquid-gas systems near the critical point. The density coexistence curve of liquid and gas phases in the pressure versus temperature phase diagram ends at the critical point (T_c, P_C). The deviations of the coexistence curve from the critical density near the critical point follow the power-law $A|T_C - T|^\beta$. The coefficient depends on the substance, but the exponent is identical for all liquid-gas systems. Hence, independent of the underlying interactions and involved particles, universal behavior manifests itself at the macroscopic scale. Another example is the magnetization of ferromagnetic materials with one easy magnetization axis. Near the critical point the magnetization can also be described by a power-law $B|T_C - T|^\beta$, where the exponent β has the same value as in liquid-gas systems.

However, universality is in no way restricted to condensed matter systems. In few-body physics a large variety of universal properties exists. For short-range interactions and large scattering lengths there are low-energy observables, which are independent of the details of the interaction. To be more precise, universal in this context means that the observables are functions of the scattering length only and not of other properties of the interaction. An example is the binding energy $E_D = \hbar^2/ma^2$ of a two-body bound state, called dimer, for positive scattering lengths as well as the atom-dimer scattering length. The binding energies in three-body systems are also governed by a universal relation for large scattering lengths, which is called *Efimov effect*[1] [2]. The Efimov effect describes a geometric bound state spectrum. Adjacent bound states possess a binding energy ratio which is given by a universal number, which is ≈ 515 in the case of identical bosons. In the resonant limit $a \to \pm\infty$ the spectrum consists of an unlimited number of bound states with an accumulation point at zero energy. Many more universal properties can be found in few-body systems and probably some are still undiscovered.

The renormalization group (RG) has had great impact on the understanding of universal phenomena. In the RG the flow of the coupling constants is examined, when degrees of freedom are integrated out. The flow of the coupling constants can belong to different topologies. The simplest and best studied topology is the RG fixed point topology. The coupling constants flow towards a fixed point, where their evolution comes to an end. The described universal behavior of condensed matter systems near the critical point can be explained by the RG fixed point topology. The RG trajectories of these condensed matter systems are considered to flow to the same fixed point.

A more complex topology is the limit cycle. As the name indicates, the topology exhibits a cyclic structure. Instead of flowing towards a fixed point, the coupling constants flow periodically in a closed curve. This topology is also connected to universal behavior. It can be shown that the limit cycle is related to the Efimov effect. A necessary condition for the appearance of limit cycles is discrete scale invariance (DSI). Discrete scale invariance occurs in very different systems and phenomena like turbulences, earthquakes or the formation of black holes [3].

The limit cycle is investigated within different renormalization group frameworks like e.g. Wilson RG [4, 5] or functional RG [6, 7]. The first part of this thesis is concerned with the study of limit cycles with the similarity renormalization group (SRG). The SRG is a continuous series of unitary transformations of the Hamilton operator depending on a flow parameter. In nuclear physics the SRG is a successful method for softening potentials and thus reaching better numerical convergence. But it is also used in condensed matter physics, where it is referred to as flow equation approach. The low- and high-energy degrees of freedom decouple during the evolution of the SRG. As a consequence, the potential obtains a band-diagonal structure, which provides a different kind of cutoff compared to conventional RG.

An important goal is to find the transition between pionless and pionfull effective field theories (EFT) describing nucleon-nucleon interactions. In pionless EFTs contact interactions are considered, while chiral EFT with explicit pions is a more fundamental theory which considers pions to be the exchange particles of the nucleon-nucleon force. The origin of the nucleon-nucleon force is the strong interaction, which is described by QCD. However, the strong coupling constant becomes large at small energies and thus inhibits a direct calculation of nucleon-nucleon interactions. An alternative is the application of the mentioned effective field theories. Thereby, chiral EFTs respect the symmetries of QCD and exploit the approximate chiral symmetry. Both EFT approaches, pionless and chiral EFT with pions, are successfully applied in their particular energy region. In principle the pions can be integrated out in the low energy regime. Therefore, the pionless EFT should be deducible from the chiral EFT with explicit pions. Due to the success in nuclear physics, the SRG appears to be a practical method for deducing the pionless EFT. The approach can be sketched as follows. A three nucleon system with large scattering length is considered. The corresponding Hamiltonian, which is derived from a pionfull chiral

[1] There are some cases, in which the Efimov effect does not occur if identical fermions are involved. For further information see [1].

EFT, is then evolved with the SRG down to the region of pionless EFTs. During this evolution a limit cycle should then appear and thus indicate the pionless EFT.

In the first part of this thesis we try to lay the foundation for this approach. Our aim is to find general criteria for detecting limit cycles in SRG evolved potentials. To this end, we evolve different two- and three-body systems, which exhibit the limit cycle, and then try to extract signatures of the limit cycle in the evolution.

The second part of this thesis considers limit cycles at finite density. Finite density systems are a broad and exciting topic with many different aspects. Due to the interplay of many constituents new collective phenomena appear. Intriguing many-body phenomena are for example exhibited by ultracold gases. Well-known are Bose-Einstein condensates (BEC), for which universal behavior can also be found. In a sufficiently dilute homogeneous BEC the interaction energy per particle in the ground state is a universal quantity, which depends on the scattering length[2]. Another famous example is superfluidity. Superfluidity was first discovered in liquid helium, but a superfluid phase is e.g. also assumed to exist in neutron stars. The BCS theory, which originally considers superconductivity, is as well employed for describing superfluidity in fermionic systems. In essence, this is due to the formation of Cooper pairs in both phenomena. An example of the limit cycle can also be found in this context. In [8] a limit cycle was detected in a system described by a modified BCS Hamiltonian.

In general, ultracold atomic gases provide an important test ground for few- and many-body physics. A principal reason for this is the tunability of the scattering length by magnetic fields due to the Feshbach resonance. This special property allowed the first experimental evidence of the Efimov effect in ultracold atomic gases.

In this thesis we focus on three-component ultracold Fermi gases. To be more precise, we examine a three-body system with large scattering lengths and unequal masses in the presence of a Fermi sea for each fermion species at zero temperature. In the vacuum this physical system is well studied and displays the Efimov effect and the corresponding limit cycle. For this system we apply an EFT framework. Of particular interest is how the properties and the spectrum of the system are changed in the medium. We thereby focus on the negative scattering length region and on the unitary limit. Another aspect of this thesis are considerations concerning phase diagram properties.

This thesis is structured as follows. In chapter two the properties of limit cycles are discussed. Chapter three is concerned with general aspects of the similarity renormalization group. Among others, the origin of the diagonalization as well as the induction of higher-body forces is explained. In chapter four the $1/R^2$ potential in a two-body system is evolved in the SRG. Before, the characteristics of the potential and the corresponding limit cycle is briefly reviewed. In Chapter five we move on to the SRG in three-body systems. First, the applied framework is introduced. Subsequently, the SRG equations for the different generators are derived and the arising problems in the three-body space are discussed. A separable potential with large scattering length is evolved in two-ways, with and without induced three-body potential. In chapter six we turn to the topic of ultracold Fermi gases. We explain the effective field theory framework and deduce the Feynman rules. In chapter seven we calculate the dimer propagator and discuss the two-body pole structure. In chapter eight the three-body scattering amplitude is deduced and the spectra as well as other properties of the bound states are presented. This thesis is concluded with a summary and an outlook.

[2] Note that there are nonuniversal corrections to it.

2 Limit Cycles

In this section we discuss the nature and signatures of renormalization group (RG) limit cycles. We mainly follow the description of the review [1] and start with a short introduction of the RG approach.

In the standard renormalization group approach high-energy degrees of freedom are integrated out, while keeping the low-energy observables unchanged. In momentum space this is commonly implemented by introducing a cutoff Λ which is then lowered. Expanding the Hamiltonian in an operator basis

$$\mathscr{H} = \sum_n g_n \mathscr{O}_n \,, \tag{2.1}$$

the elimination of the high-energy degrees of freedom is compensated by a change in the coupling constants g_n. The resulting change in the coupling constants can be written as a differential equation

$$\Lambda \frac{d}{d\Lambda} \mathbf{g} = \beta(\mathbf{g}) \,, \tag{2.2}$$

with $\mathbf{g} = (g_1, g_2, \ldots)$ and the beta function $\beta(\mathbf{g})$, which is in general a complicated nonlinear function. The flow of the coupling constants during the decrease of the cutoff is referred to as RG trajectory. This flow can have very complex topologies. The simplest one is the fixed point topology. In this topology the coupling constants flow towards a fixed point $\mathbf{g}_*$, where they remain unchanged. The fixed point Hamiltonian is independent of the change of the cutoff and for its coupling constants holds $\mathbf{g}(\Lambda) = \mathbf{g}_*$. Hence, the fixed point is a solution of

$$\beta(\mathbf{g}_*) = 0 \,. \tag{2.3}$$

Since Λ provides a scale and the fixed point Hamiltonian is independent of the cutoff, the fixed point Hamiltonian has to describe a scale invariant system.

Universality of condensed matter systems near a critical point can be related to the fixed point topology. Examples are the universal behavior of ferromagnetic materials or liquid-gas systems near the critical point. The universal behavior can be explained in the framework of the renormalization group. The different systems displaying the universal behavior are represented by Hamiltonians, which are located in different regions in the space of coupling constants but flow towards the same fixed point. Although the systems can be very distinct and can be located in widely separated regions, their trajectory leads to the same fixed point.

Limit cycles are a more complicated RG topology. Instead of flowing towards a fixed point, the limit cycle trajectory is a closed curve in the space of coupling constants. The coupling constants run through the entire curve. Every time the cutoff is reduced by a factor λ_0 a full cycle is completed and the coupling constants return to their value $\mathbf{g}(\Lambda) = \mathbf{g}(\Lambda/\lambda_0)$. The factor λ_0 is called scaling factor and depends on the considered system. The limit cycle trajectory $\mathbf{g}_c$ can thus be parametrized by an angle θ

$$\mathbf{g}(\Lambda) = \mathbf{g}_c(\theta + 2\pi \ln(\Lambda/\Lambda_0)/\ln(\lambda_0)) \,, \tag{2.4}$$

with a starting point $\mathbf{g}(\Lambda_0) = \mathbf{g}_c(\theta)$. The possibility of a limit cycle trajectory was first considered by Wilson in [9].

A necessary condition for the appearance of limit cycles is the invariance under a discrete scale transformation $\mathbf{r} \to \lambda_0^n \mathbf{r}$ for all integers n. Consider a system with degrees of freedom with length scales $\geq 1/\Lambda$. If the degrees of freedom between $1/\Lambda$ and λ_0/Λ are integrated out, the behavior of the system remains unchanged. This is only possible if the system exhibits discrete scale invariance. This condition results in log-periodic behavior of physical observables. Consequently, logarithmic periodicity in physical systems is a signature of limit cycles.

In general, limit cycles do not appear in systems with dimensions $D < 3$. This can be justified by the c-theorem in two spatial dimensions [10]. However, there exists a counterexample [11].

An example of a physical system exhibiting the limit cycle is a non-relativistic three-particle system with large two-body scattering lengths. In this system the Efimov effect occurs. If the scattering lengths a_i are in the unitary limit ($a_i \to \pm\infty$), there are infinitely many three-body bound states with an accumulation point at zero energy. The ratio of adjacent bound state energies is fixed by $E_T^{(n+1)}/E_T^{(n)} \to \lambda_0^{-2}$ as $n \to \infty$ and $a_i \to \pm\infty$. This ratio is the inverse square of the discrete scaling factor, which depends on the statistics and the masses of the three particles. Hence, in this case the bound state spectrum displays a signature of the limit cycle. For an extensive description and the details when the Efimov effect occurs we refer to [1].

Up to now there are only few systems known where a limit cycle is present. Besides the mentioned three-body system, which is relevant in nuclear and atomic physics, there are e.g. a two-body system with the $1/R^2$ potential [12], an extended BCS Hamiltonian [8] and a simple discrete Hamiltonian model [13,14], which we will discuss in the following. Additionally, limit cycles were observed in quantum field theory models [11,15] and S-matrix models [16,17]. Because there are rather few and special systems which display the limit cycle, in contrast to the RG fixed point, the study of limit cycles is rather in its infancy. However, discrete scale invariance appears in many different systems like earthquakes and turbulences [3]. It is therefore assumed that limit cycles occur more often than the current situation indicates.

In this thesis we examine the appearance of limit cycles using the similarity renormalization group (SRG) in the $1/R^2$ potential as well as in the three-body system with large two-body scattering lengths. Additionally, we investigate the three-body system in the medium. Therefore, we will go into more detail about the limit cycle in these systems in chapter 4.2, 5.5 and 8.2.

To obtain a better insight into the appearance of limit cycles we briefly discuss the mentioned extended BCS Hamiltonian and then present in more detail a simple discrete Hamiltonian model exhibiting a limit cycle.

In [8] an extension to the BCS Hamiltonian is applied, which is used to describe ultrasmall superconducting grains [18]. The reduced BCS Hamiltonian is modified by adding a time reversal breaking term. Instead of a constant coupling the potential is now given by

$$V_{jj'} = \begin{cases} G + i\delta\theta & \text{if} \quad \epsilon_j > \epsilon_{j'} \\ G & \text{if} \quad \epsilon_j = \epsilon_{j'} \\ G - i\delta\theta & \text{if} \quad \epsilon_j < \epsilon_{j'} \,, \end{cases} \tag{2.5}$$

with the electron pair energies ϵ_j, the level spacing 2δ and the coupling constant $G = g\delta$. The standard BCS variational ansatz is still applicable and thus the gap equation can be calculated. However, in this model one obtains an infinite number of BCS eigenstates and the corresponding condensates for large system sizes. In the weak coupling limit the ratios of the condensation energies of adjacent BCS eigenstates are given by $e^{-2\lambda_e}$ with $\lambda_e = \pi/\theta$. Applying the RG approach by integrating out the highest energy levels one finds a limit cycle in the coupling constant g with the scaling factor $e^{-\lambda_e}$. The coupling constant exhibits discontinuous jumps from $+\infty$ to $-\infty$, whenever the lowest condensate vanishes from the spectrum [8]. These discontinuous jumps can also be observed in the discrete model of Glazek and Wilson.

This discrete model was discussed in [13,14]. A short summary can be found in [1]. The discrete Hamiltonian is defined by its matrix elements

$$\langle m|H_N|n\rangle = H_{mn}(g_N, h_N) = (E_m E_n)^{1/2} \left[\delta_{mn} - g_N - i h_N s_{mn}\right] , \tag{2.6}$$

where δ_{mn} is the Kronecker delta and s_{mn} is zero if $m = n$. For $m \neq n$ holds $s_{mn} = (m-n)/|m-n|$. The energies are given by $E_n = b^n$ with $b > 1$. They are the eigenvalues of the noninteracting Hamiltonian H_0 with $\langle m|H_0|n\rangle = H_{mn}(0,0)$. The model has an ultraviolet cutoff, which is given by b^N. According to this for all subscripts $m, n \leq N$ holds. A lower boundary M to the indices can also be introduced to obtain a finite size matrix. In the general case M is assumed to be $M = -\infty$.

We consider the interacting case of this model with $g_N \neq 0$ and $h_N \neq 0$. In this case the Hamiltonian can exhibit a limit cycle as N goes to infinity or it can also exhibit chaotic behavior. In the continuum limit with $b \to 1$ the negative bound states form a geometric series with an accumulation point at $E = 0$. Thus, this model has some similarities with the three-body system with large scattering lengths.

The renormalization group method can be applied to this model. In the first step the state $|N\rangle$ is integrated out which results in a smaller size Hamiltonian H_{N-1}. Subsequently, the state $|N-1\rangle$ is eliminated and so on. This leads to a discrete sequence of cutoffs. The procedure keeps low energy eigenvalues fixed as long as the energy is much smaller than the cutoff. The elimination can be performed by considering the eigenvalue problem

$$\sum_{n=-\infty}^{N} H_{mn}\Psi_n = E\Psi_m \tag{2.7}$$

and using Gaussian elimination. Astonishingly, the Hamilton matrix retains its form during the renormalization group transformation. However, the coupling constants change and of course the size of the matrix is reduced. The first step, the elimination of state $|N\rangle$, yields for the coupling constants

$$g_{N-1} = g_N + (g_N^2 + h_N^2)/(1 - g_N) \quad \text{and} \quad h_{N-1} = h_N \,. \tag{2.8}$$

The coupling constant h_N remains unchanged by the RG procedure. Integrating out p states one obtains the following formula

$$g_{N-p} = h_N \tan\left[\arctan(g_N/h_N) + p\arctan(h_N)\right] \,. \tag{2.9}$$

If h_N is chosen to be $h_N = \tan(\pi/p)$, it holds $g_N = g_{N-p}$. Consequently, after p iterations the coupling constant returns to its original value and one cycle is completed. The scaling factor λ_0 is then given by

$$\lambda_0 = b^{\pi/\arctan(h)}\,. \tag{2.10}$$

In the continuum limit the coupling constant becomes a continuous function of the cutoff Λ. The functional dependence is given by

$$\frac{g(\Lambda)}{h} = \frac{\frac{g(\Lambda_0)}{h} - \tan[c\ln(\Lambda/\Lambda_0)]}{1 + \frac{g(\Lambda_0)}{h}\tan[c\ln(\Lambda/\Lambda_0)]}\,, \tag{2.11}$$

with $c = \arctan(h)/\ln(b)$. The function $g(\Lambda)$ is depicted in Fig. 2.1. As Λ is increased the coupling constant $g(\Lambda)$ decreases to $-\infty$ and then jumps to $+\infty$, where it again decreases. This behavior is repeated every cycle. Jumps do always appear in the RG trajectory if there is only one coupling constant which is affected by the RG procedure. If there are two or more coupling constants, $\mathbf{g}(\Lambda)$ can be a continuous function.

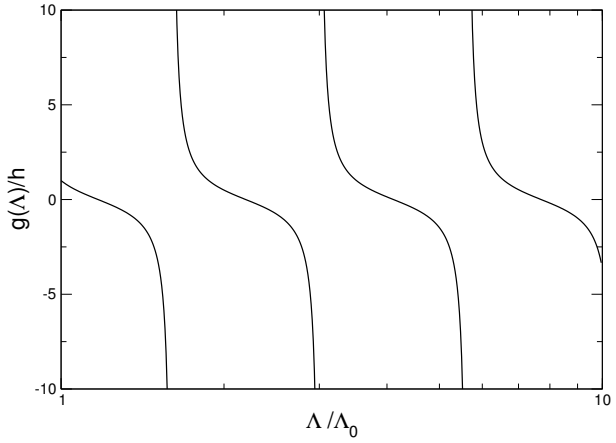

Figure 2.1.: The coupling constant $g(\Lambda)/h$ is depicted as a function of Λ/Λ_0 with $g(\Lambda_0)/h = 1$ and $c = 5$. Note the logarithmic periodicity.

Part I.
Limit Cycles in SRG

3 General SRG

The concept of the similarity renormalization group (SRG) was independently developed by Wegener [19] and Glazek and Wilson [20, 21]. Glazek and Wilson named this approach in their early work similarity renormalization scheme, whereas Wegener called his approach flow equations. The SRG approach is frequently applied in condensed matter physics as well as low energy nuclear physics. Its main feature is the decoupling of low- and high-energy degrees of freedom, which results in improved numerical convergence. A good introduction to this approach is given in [22]. Information about the application of the SRG in nuclear physics can e.g. be found in [23–25].

As discussed in Chapter 2, in standard renormalization group (RG) methods high- and low-energy degrees of freedom are decoupled by integrating out high-energy degrees of freedom. To keep physical observables invariant, coupling constants are modified and counterterms are introduced in order to absorb the contribution of the states which are integrated out. The size of the Hilbert space is reduced in this method.

Decoupling is advantageous because fewer states are needed for the computation of low-energy observables. Additionally, it leads to better numerical convergence. The SRG method decouples low- and high-energy degrees of freedom in a different way. The potential becomes band diagonal during the evolution while keeping the size of the Hilbert space constant. This band diagonal structure obviously implicates the decoupling of low- and high-energy states. In Fig. 3.1 these two different approaches are depicted.

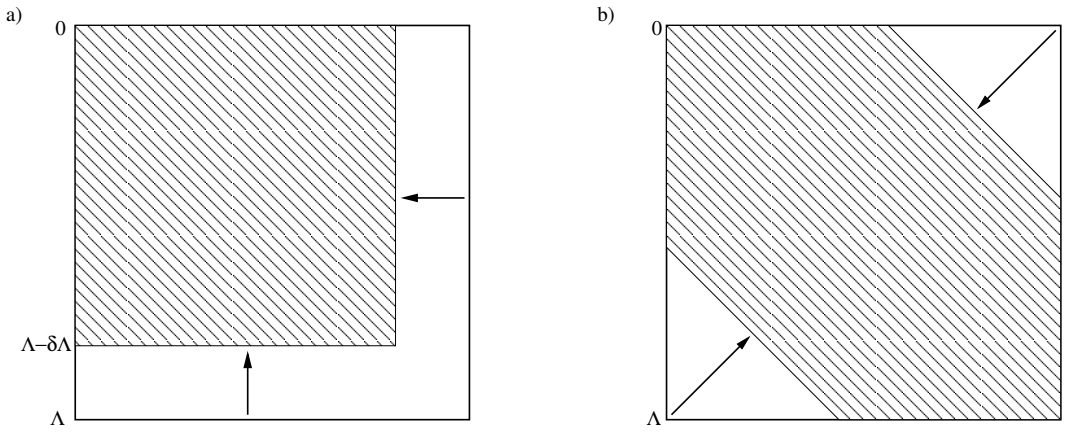

Figure 3.1.: Decoupling of a potential $V(k,k')$. a) conventional RG evolution (e.g. $V_{low\,k}$ [26] evolution): states within the range $[\Lambda-\delta\Lambda,\Lambda]$ are integrated out. b) SRG evolution: all states are maintained, but the potential becomes band diagonal. Adapted from [22].

The SRG is a continuous series of unitary transformations depending on the flow parameter s

$$H(s) = U(s)H(s=0)U^{\dagger}(s) = T + V(s)\,. \tag{3.1}$$

Since we focus in this section on the general properties of the SRG and for readability, we will write out the flow parameter s as an explicit variable. In subsequent sections the dependency on the flow parameter is mostly not explicitly labeled.

Because this transformation is unitary, all observables stay constant during the evolution. The flow parameter s can run from zero to infinity with the starting point $s=0$ of the evolution with $H(s=0)=H$ and the initial Hamiltonian H. The kinetic energy T is independent of the flow parameter so that the potential is the only constituent of the Hamiltonian which depends on s. The evolution of the Hamilton operator is determined by the differential equation

$$\frac{dH(s)}{ds} = [\eta(s), H(s)]\,, \tag{3.2}$$

with the antihermitean generator

$$\eta(s) = -\eta(s)^{\dagger}\,. \tag{3.3}$$

This differential equation is in practice used to evolve the potential. In principle, every antihermitian generator η can be chosen for the SRG evolution. However, band diagonalization, for example, is only achieved for certain generators. Usually, $\eta(s)$ is constructed by

$$\eta(s) = [G(s), H(s)] \,, \tag{3.4}$$

which leads to the common SRG equation

$$\frac{dH(s)}{ds} = [[G(s), H(s)], H(s)] \,. \tag{3.5}$$

This definition of the generator as a commutator of two Hermitian operators automatically results in an antihermitian η. There is a still a free choice left for $G(s)$, which is Hermitian and can depend on s. The relative kinetic energy T_{rel} is commonly chosen for G. Since the center of mass kinetic energy commutes with H, this is equivalent to choosing the total kinetic energy. For convenience, we will therefore denote the relative kinetic energy by T. A different choice for $G(s)$ suggested by Wegner is e.g. the diagonal part of $H(s)$. In this thesis we also use two other generators, where G is a function of the kinetic energy operator T

$$\begin{aligned} G_e &= -\sigma^2 \exp(-T/\sigma^2) \\ G_i &= \frac{-\sigma^2}{1 + T/\sigma^2} \end{aligned} \tag{3.6}$$

and σ is a parameter. We refer to them as exponential and inverse generator [27], respectively. Their properties will be explained in Chapter 4.1.

Before considering further details, we show that Hamiltonians generated by the differential equation (3.2) are unitarily equivalent to the initial Hamiltonian. We follow the derivation in [22] and define $U(s)$ by

$$U(s) = T_s \exp\left(\int_0^s ds' \, \eta(s') \right) \tag{3.7}$$

$$= 1 + \sum_{n=1}^{\infty} \frac{1}{n!} \int_0^s ds_1 \ldots ds_n T_s\{\eta(s_1) \ldots \eta(s_n)\} \,. \tag{3.8}$$

T_s is the s-ordering operator, which is similarly defined as the well-known time ordering operator

$$T_s\{\eta(s_1) \ldots \eta(s_n)\} := \eta(s_{\pi(1)}) \ldots \eta(s_{\pi(n)}) \,, \tag{3.9}$$

with the permutation $\pi \in S_n$, which ensures $s_{\pi(1)} \geq s_{\pi(2)} \geq \ldots \geq s_{\pi(n)}$. It is easy to verify that $U(s)$ is an unitary operator. In the next step we differentiate $H(s)$

$$\frac{d}{ds}\left(U(s) H(s=0) U^\dagger(s) \right) = \frac{dU(s)}{ds} U^\dagger(s) H(s) + H(s) U(s) \frac{dU^\dagger(s)}{ds} \,. \tag{3.10}$$

Using (3.7) we obtain

$$\frac{dU(s)}{ds} U^\dagger(s) = \eta(s) U(s) U^\dagger(s) = \eta(s) \,. \tag{3.11}$$

As a consequence it yields

$$\frac{d}{ds}\left(U(s) H(s=0) U^\dagger(s) \right) = [\eta(s), H(s)] \,. \tag{3.12}$$

Thus, we have shown that $H(s)$, obtained form the unitary transformation $H(s) = U(s) H(s=0) U^\dagger(s)$, fulfills the differential equation (3.2). Taking also into account that the initial condition is fulfilled, we can deduce unitary equivalence.

One characteristic of the SRG evolution is that many-body forces are generated during the evolution. Assume for example that the initial Hamilton operator contains only two-body forces. Then, during the evolution three-, four- and higher-body forces are induced. In general, N-body forces with arbitrarily large N are generated. The only limit is the number of particles inside the system. Hence, in principle all interactions up to N-body interactions have to be incorporated in the SRG evolution, where N is the total particle number of the system. However, for systems with large particle number the use of truncation schemes for many-body interactions may be necessary. To illustrate how many-body interactions are generated, we write down a Hamilton operator with a two-body force in second quantization

$$H = T + V_2 = \sum_i T_i a_i^\dagger a_i + \sum_{pklm} V_2(p,k,l,m) \, a_p^\dagger a_k^\dagger a_l a_m \,. \tag{3.13}$$

We consider bosons and use the common T generator. Therefore, it yields $[a_i, a_j^\dagger] = \delta_{ij}$. Using the relation for general operators A, B, C, D

$$[AB, CD] = A[B,C]D - C[D,A]B + CA[B,D] - [C,A]BD\,, \tag{3.14}$$

the generator η can be written as

$$\eta = [T,H] = [T,V_2] = \sum_{pklm} V_2(p,k,l,m)(T_k + T_p - T_m - T_l)(a_p^\dagger a_k^\dagger a_l a_m)\,. \tag{3.15}$$

The SRG evolution in this case is given by $dH/ds = [\eta, H] = [\eta, T] + [\eta, V_2]$. We compute the second commutator with the abbreviation $A_{pklm} = V_2(p,k,l,m)(T_k + T_p - T_m - T_l)$

$$\begin{aligned}[\eta, V_2] &= \sum_{pklm} A_{pklm} \sum_{ijuv} V_2(i,j,u,v)\,[a_p^\dagger a_k^\dagger a_l a_m, a_i^\dagger a_j^\dagger a_u a_v] \\ &= \sum_{pklm} A_{pklm} \sum_{ijuv} V_2(i,j,u,v)\left(a_p^\dagger a_k^\dagger [a_l a_m, a_i^\dagger a_j^\dagger] a_u a_v - a_i^\dagger a_j^\dagger [a_u a_v, a_p^\dagger a_k^\dagger] a_l a_m\right)\,. \end{aligned} \tag{3.16}$$

Both terms of the difference have the same structure. So we only write down the first term

$$\begin{aligned}&\sum_{pklm} A_{pklm} \sum_{ijuv} V_2(i,j,u,v)\, a_p^\dagger a_k^\dagger [a_l a_m, a_i^\dagger a_j^\dagger] a_u a_v \\ =&\sum_{pklm} A_{pklm} \sum_{ijuv} V_2(i,j,u,v)\, a_p^\dagger a_k^\dagger (a_j^\dagger a_l \delta_{mi} + a_i^\dagger a_m \delta_{jl} + a_i^\dagger a_l \delta_{mj} + a_j^\dagger a_m \delta_{il} + \delta_{mi}\delta_{lj} + \delta_{jm}\delta_{il}) a_u a_v\,. \end{aligned} \tag{3.17}$$

One directly sees that two- and three-body potentials are obtained. After all remaining commutators are included, the three-body terms do not cancel each other. Consequently, a three-body interaction has to be included in order to maintain unitarity if the considered system contains at least three particles. This in turn leads to an induction of a four-body potential and so forth, as can be shown with some effort. The induction of arbitrarily high many-body interactions is a direct consequence of the commutator structure.

Nevertheless, the SRG evolution of an N-body potential is fully determined by the N-body system. Higher-body interactions have no influence on the evolution of lower-body interactions. Thus, the evolution of an A-body potential $V_A(s)$ is unaffected by the total particle number $N \geq A$ in a system, equal initial potentials $V_i(s=0)$ for all $i \leq A$ presupposed. This can also be demonstrated in the second quantization framework similar to the preceding calculation. We denote an N-body interaction in second quantization by

$$V_N = \sum_{p_1 \ldots p_N} \sum_{k_1 \ldots k_N} V_N(p_1, \ldots, p_N, k_1, \ldots, k_N) \left(\prod_{i=1}^N a_{p_i}^\dagger\right) \left(\prod_{j=1}^N a_{k_j}\right)\,. \tag{3.18}$$

The SRG equation is given by

$$\frac{dH}{ds} = \sum_i \frac{dV_i}{ds} = [\eta, T + \sum_i V_i] = [\eta, T] + \sum_i [\eta, V_i]\,, \tag{3.19}$$

where we again apply the kinetic energy generator

$$\eta = [T, T + \sum_i V_i] = \sum_i [T, V_i]\,. \tag{3.20}$$

In general, an N-body interaction contributes to an A-body interaction if on the right hand side of Eq. (3.19) terms with A annihilation and creation operators and a coefficient including the potential function $V_N(\ldots)$ are created. Due to the nature of the T operator, the only terms relevant to this structure are of the kind $[[T, V_i], V_j]$, see (3.19) and (3.20). We will now consider the general term $[[T, V_N], V_A]$. If this commutator produces terms with M annihilation and creations operators, where M is smaller than the maximum of N and A, higher-body interactions influence the evolution of lower-body interactions. As seen for the two-body potential, the T operator in $[T, V_N]$ gives only an additional factor. Hence, we can write this commutator as $[T, V_N] = \sum_{p_1 \ldots p_N} \sum_{k_1 \ldots k_N} B_N(p_1, \ldots, p_N, k_1, \ldots, k_N) \left(\prod_{i=1}^N a_{p_i}^\dagger\right) \left(\prod_{j=1}^N a_{k_j}\right)$. It follows

$$\begin{aligned}[[T, V_N], V_A] = &\sum_{p_1 \ldots p_N} \sum_{k_1 \ldots k_N} \sum_{l_1 \ldots l_A} \sum_{t_1 \ldots t_A} B_N(p_1, \ldots, p_N, k_1, \ldots, k_N) V_A(l_1, \ldots, l_A, t_1, \ldots, t_A) \\ &\left[\left(\prod_{i=1}^N a_{p_i}^\dagger\right)\left(\prod_{j=1}^N a_{k_j}\right), \left(\prod_{m=1}^A a_{l_m}^\dagger\right)\left(\prod_{n=1}^A a_{t_n}\right)\right]\,. \end{aligned} \tag{3.21}$$

Using Eq. (3.14) the remaining commutator in (3.21) can be written as

$$\left(\prod_{i=1}^{N} a_{p_i}^\dagger\right)\left[\left(\prod_{j=1}^{N} a_{k_j}\right),\left(\prod_{m=1}^{A} a_{l_m}^\dagger\right)\right]\left(\prod_{n=1}^{A} a_{t_n}\right)-\left(\prod_{m=1}^{A} a_{l_m}^\dagger\right)\left[\left(\prod_{n=1}^{A} a_{t_n}\right),\left(\prod_{i=1}^{N} a_{p_i}^\dagger\right)\right]\left(\prod_{j=1}^{N} a_{k_j}\right). \tag{3.22}$$

Considering only the annihilation and creation operators outside the commutators and noting that the total number of creation and annihilation operators has to be equal, one finds that the commutator in (3.22) produces at least a M-body interactions, where M is the maximum of N and A. Consequently, an interaction can not contribute to the evolution of an interaction with a smaller number of involved particles.

We now elaborate on the decoupling mechanism. For this purpose, we consider the T generator and write down the SRG evolution for two particles

$$\frac{dV_2}{ds} = 2TV_2T - V_2TT - TTV_2 + TV_2V_2 + V_2V_2T - 2V_2TV_2\,. \tag{3.23}$$

In the two-body evolution the angular momentum decouples. Therefore, for each partial wave l using a relative momentum basis the SRG evolution can be written as

$$\frac{d}{ds}V_2(p,q,l,s) = -(p^2-q^2)^2\,V_2(p,q,l,s) + \int_0^\infty dk\,k^2(p^2+q^2-2k^2)V_2(p,k,l,s)V_2(k,q,l,s)\,, \tag{3.24}$$

where we set the mass to one for convenience. The definition of the applied basis will be given in the following chapter. Crucial for the decoupling of low- and high-momentum states is the first term in (3.24). Considering the weak coupling limit, the second term in (3.24) can be neglected. We thus obtain the equation

$$\frac{d}{ds}V_2(p,q,l,s) = -(p^2-q^2)^2\,V_2(p,q,l,s)\,, \tag{3.25}$$

which is solved by

$$V_2(p,q,l,s) = V_2(p,q,l,s=0)\exp(-s(p^2-q^2)^2)\,. \tag{3.26}$$

The exponential function suppresses matrix elements of momentum states with large energy difference. As a consequence, the evolved potential becomes more and more band diagonal with growing flow parameter s. In this context we introduce a different flow parameter λ. It is defined by

$$\lambda = \frac{1}{s^{1/4}} \tag{3.27}$$

and has the dimension of momentum, which can be seen by (3.26). The parameter λ can be regarded as an effective momentum cutoff and is a measure for the width of the band diagonal structure of the evolved potential.

We have neglected the second term in (3.24) in this consideration. But it turns out that the suppressing exponential function is a dominant part of the SRG evolution and leads to decoupling. To illustrate this, we have plotted a composite S-Wave Yukawa-Potential as an example

$$V_{yuk}(p,q,l=0,s=0) = -\frac{2}{\pi}\left(\frac{g_1}{4pq}\log\left(\frac{(p-q)^2+\mu_1^2}{(p+q)^2+\mu_1^2}\right)+\frac{g_2}{4pq}\log\left(\frac{(p-q)^2+\mu_2^2}{(p+q)^2+\mu_2^2}\right)\right) \tag{3.28}$$

for four different values of s in Fig. 3.2. The initial potential is apparently far away from having a band diagonal structure. The plots show how the potential becomes more and more diagonal during the SRG evolution. Note that there is a free length scale l_0 in the system. We therefore state the quantities in dimensions of l_0 in Fig. 3.2.

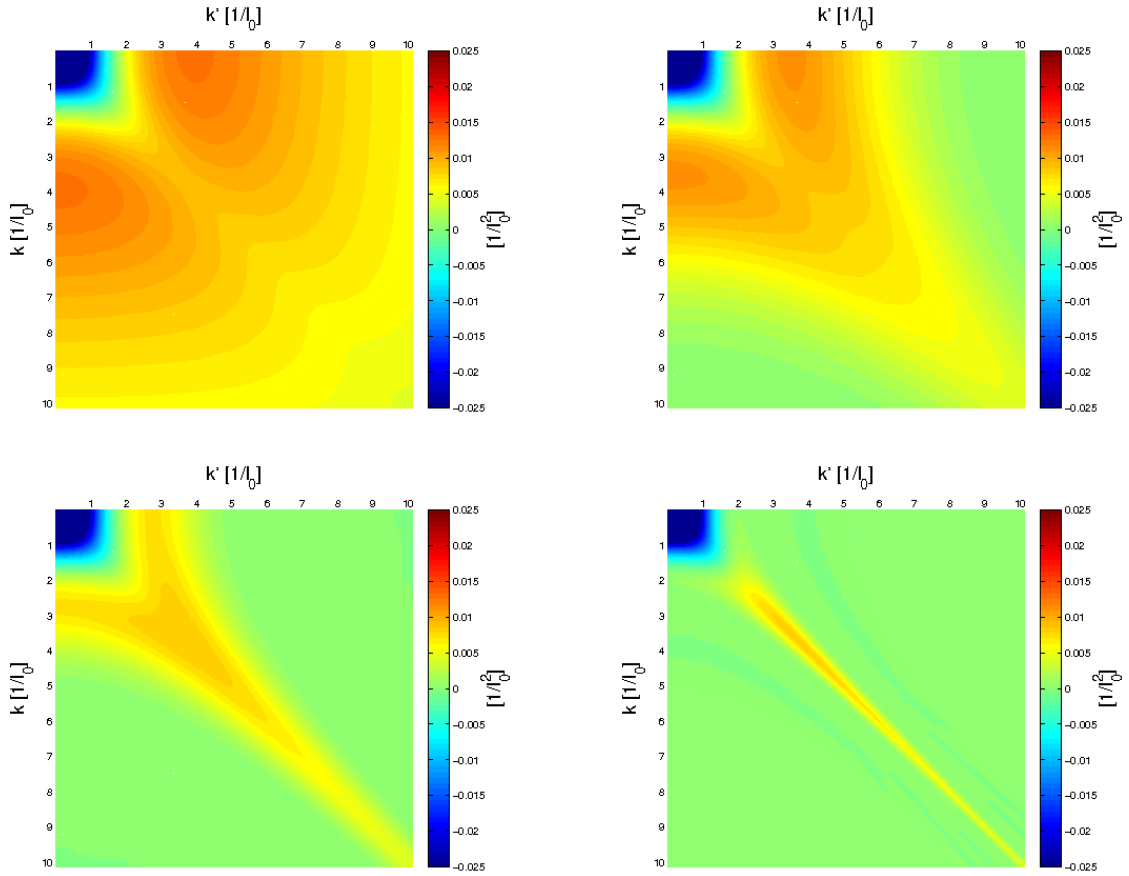

Figure 3.2.: Evolution of the S-wave Yukawa potential, defined in (3.28). The flow parameter values s are approximately 0, 0.00048, 0.0055 and 0.1 in units of $[l_0^4]$ from top left to bottom right (The corresponding values of the flow parameter λ are approximately given by ∞, 6.76, 3.67 and 1.78 in units of $[1/l_0]$). The parameters of the potential are given by $g_1 = -0.15\, l_0^{-4}$, $g_2 = +1.5\, l_0^{-4}$, $\mu_1 = 1\, l_0^{-2}$ and $\mu_2 = 6\, l_0^{-2}$.

4 Two-body SRG

In this chapter we consider the $1/R^2$ potential in the SRG framework. The $1/R^2$ potential possesses a limit cycle under RG transformations in the two-body system. We start with this simple system and try to find signatures of the limit cycle when the potential is evolved with the SRG. We consider bosons and set the mass $m = 1$ as well as $\hbar = 1$. This chapter is structured as follows. First, we briefly discuss some features of the two-body SRG. Subsequently, the $1/R^2$ potential and the appearing limit cycle are described. In the last section we discuss the results of the SRG evolution of the potential.

4.1 Basics of Two-body SRG

In the two-body system the implementation of the SRG is rather simple. First a generator has to be chosen. The most common choice is the kinetic energy generator. In this chapter we will use the kinetic energy generator, as well as the inverse and exponential generators, which are discussed later in this section. We start with the derivation of the SRG flow equation for the kinetic energy generator, which is straightforward. The Hamilton operator is given by $H = T + V_2$. The SRG generator is chosen to be

$$\eta = [T, H] = [T, T + V_2] = [T, V_2] \,. \tag{4.1}$$

Using this, we are left with the computation of the commutators and obtain the SRG equation

$$\frac{dV_2}{ds} = [[T, V_2], T + V_2] = 2TV_2T - V_2TT - TTV_2 + TV_2V_2 + V_2V_2T - 2V_2TV_2 \,. \tag{4.2}$$

A suitable basis is the partial wave momentum basis. The basis states are given by $|plm_l\rangle$, where p is the absolute value of the relative momentum, l is the angular momentum of the two-body system and m_l is the corresponding magnetic quantum number. The scalar product is given by

$$\langle \mathbf{p}'|plm_l\rangle = (2\pi)^{3/2} \frac{\delta(p'-p)}{pp'} Y_{lm_l}(\hat{\mathbf{p}}') \,, \tag{4.3}$$

with the spherical harmonic functions $Y_{lm_l}(\hat{\mathbf{p}}')$, where $\hat{\mathbf{p}}'$ denotes the angular components of $\mathbf{p}'$, $\mathbf{p}' = \hat{\mathbf{p}}' p'$. The normalization is given by $1 = \int (d^3k/(2\pi)^3) |\mathbf{k}\rangle\langle\mathbf{k}|$. The basis states are complete and orthonormal

$$\sum_{lm_l} \int_0^\infty dp\, p^2 |plm_l\rangle\langle plm_l| = 1 \,, \tag{4.4}$$

$$\langle plm_l|qjm_j\rangle = \frac{\delta(q-p)}{pq} \delta_{lj}\delta_{m_l m_j} \,. \tag{4.5}$$

Interchanging the particles results in $|plm\rangle \to (-1)^l |plm\rangle$. If identical spinless bosons are considered, only even l are allowed. For spherically symmetric potentials we can make use of $\langle plm_l|V_2|qjm_j\rangle = \delta_{lj}\,\delta_{m_l m_j} V_2(p,q,l)$ and obtain the SRG equation directly from (4.2)

$$\frac{d}{ds} V_2(p,q,l) = -(p^2-q^2)^2\, V_2(p,q,l) + \int_0^\infty dk\, k^2 (p^2+q^2-2k^2)\, V_2(p,k,l) V_2(k,q,l) \,, \tag{4.6}$$

where we have used $T|plm_l\rangle = p^2|plm_l\rangle$. Next we briefly discuss the properties of the inverse and exponential generators. We refer to [27] for a detailed discussion. The two generators are defined by the operators

$$\begin{aligned} G_e &= -\sigma^2 \exp(-T/\sigma^2) \\ G_i &= \frac{-\sigma^2}{1 + T/\sigma^2} \,. \end{aligned} \tag{4.7}$$

Expanding the two operators in a Taylor series one observes that the operators reduce to the kinetic energy operator T plus a constant term for small momenta or large σ. However, the constant drops out in the commutator in Eq. (3.4). Therefore, the evolution for small momenta is similar to the evolution using the kinetic energy generator[1]. For larger momenta the evolution is suppressed. This results in a computational speedup and it is possible to evolve to higher values of the flow-parameter s. Of central interest for our consideration is, however, the property that the evolution of the potential is suppressed in a large region of the momentum space. Keep in mind that small values of σ lead to larger suppressed regions.

The SRG equation for the exponential generator is given by

$$\begin{aligned}\frac{d}{ds}V_2(p,q,l) = \sigma^2(p^2-q^2)\left(e^{-p^2/\sigma^2}-e^{-q^2/\sigma^2}\right)V_2(p,q,l) \\ +\sigma^2\int_0^\infty dk\,k^2\left(-e^{-p^2/\sigma^2}-e^{-q^2/\sigma^2}+2e^{-k^2/\sigma^2}\right)V_2(p,k,l)V_2(k,q,l)\end{aligned} \tag{4.8}$$

and for the inverse generator by

$$\begin{aligned}\frac{d}{ds}V_2(p,q,l) = \sigma^2(p^2-q^2)\left(\frac{1}{1+p^2/\sigma^2}-\frac{1}{1+q^2/\sigma^2}\right)V_2(p,q,l) \\ +\sigma^2\int_0^\infty dk\,k^2\left(-\frac{1}{1+p^2/\sigma^2}-\frac{1}{1+q^2/\sigma^2}+\frac{2}{1+k^2/\sigma^2}\right)V_2(p,k,l)V_2(k,q,l)\,.\end{aligned} \tag{4.9}$$

Since σ has dimensions of momentum, the translation of s to an effective momentum cutoff is more subtle for the alternative generators. The solutions in the weak interaction limit are

$$\begin{aligned}G_e:&\quad V_2(p,q,l,s) = V_2(p,q,l,s=0)\exp\left(-s\sigma^2\left(q^2-p^2\right)\left(e^{-p^2/\sigma^2}-e^{-q^2/\sigma^2}\right)\right) \\ G_i:&\quad V_2(p,q,l,s) = V_2(p,q,l,s=0)\exp\left(-s\sigma^2\left(q^2-p^2\right)\left(\left(1+p^2/\sigma^2\right)^{-1}-\left(1+q^2/\sigma^2\right)^{-1}\right)\right)\,.\end{aligned} \tag{4.10}$$

Thus, the effective momentum cutoff is $\lambda \sim \sigma^{-1}s^{-1/2}$. Dropping the irrelevant constant σ, we define

$$\lambda_a \equiv s^{-1/2} \tag{4.11}$$

for the alternative generators G_e and G_i. This will have important consequences when extracting limit cycle periods in this chapter.

Before we continue, we briefly discuss some numerical implementation aspects. The differential equations can be readily discretized using a momentum grid. The discretized SRG differential equations can then be solved numerically using e.g. Runge-Kutta methods. We employ the routines given in GSL (GNU Scientific Library) as well as MATLAB. Both implementations work sufficiently well. In general, no severe problems concerning the numerical implementation arise during the evolution of the $1/R^2$ potential. In the two-body system there is only one momentum variable in the incoming and outgoing state. Therefore, a sufficient amount of grid points can be used. As a benchmark for the correct implementation of the SRG equation as well as numerical errors we used the deviation of the binding energies from the initial value during the flow. We found the deviations to be negligibly small.

4.2 Discussion of the $1/R^2$ Potential

In this section, we discuss the quantum mechanical $1/R^2$ potential. It is a singular potential which displays an exact limit cycle. We start by reviewing the renormalization of the $1/R^2$ potential in an effective field theory framework. Here, the limit cycle becomes manifest in the behavior of a counterterm. We follow the discussion in Ref. [12], where further details can be found. In the subsequent section, we investigate the $1/R^2$ potential in the SRG framework and provide general criteria for isolating limit cycle behavior in the interaction.

Using natural units with $\hbar = m = 1$, the $1/R^2$ potential can be written in position space as

$$V(R) = \frac{c}{R^2}\,, \tag{4.12}$$

with $R := |\mathbf{R}|$. For subcritical coupling constants $c > -\frac{1}{4}$, the potential is well behaved and leads to a unique solution of the Schrödinger equation. For critical and supercritical values $c \leq -\frac{1}{4}$, however, the potential is singular and displays

[1] The definition of small momenta certainly depends on the parameter σ.

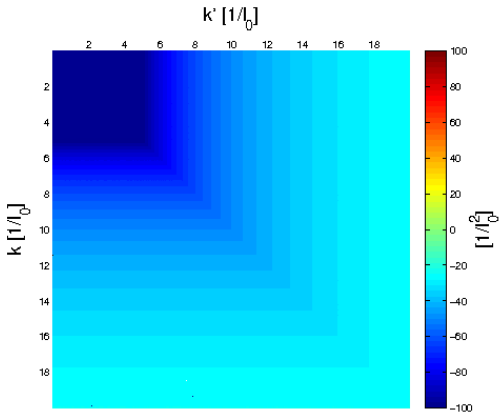

Figure 4.1.: S-Wave projected $1/R^2$ potential $V_S(k,k')$ for $\nu = 5$.

a limit cycle[2]. In this case, it is useful to define a parameter ν that characterizes the period of the limit cycle via $\nu := \sqrt{-c - \frac{1}{4}}$.

The momentum space representation of the potential can be defined via a Fourier transform in D dimensions,

$$V(Q) = \lim_{D\to 3} \int d^D\mathbf{R}\, e^{i\mathbf{Q}\cdot\mathbf{R}} V(R) = \frac{2\pi^2 c}{Q}\,, \tag{4.13}$$

where Q is the momentum transfer.

In the following, we consider only S-waves. For the momentum space matrix elements of the S-wave projected potential, we get

$$V_S(p,q) = 2\pi^2 c \left(\frac{\theta(p-q)}{p} + \frac{\theta(q-p)}{q}\right)\,, \tag{4.14}$$

where q (p) are the incoming (outgoing) momenta. The potential is depicted in Fig. 4.1. The physical observables can be obtained from the Lippmann-Schwinger equation

$$t_E(p,p') = V_S(p,p') + \frac{1}{2\pi^2}\int_0^\Lambda \frac{dq\, q^2}{E - q^2 + i\epsilon} V_S(p,q) t_E(q,p')\,, \tag{4.15}$$

where

$$k\cot\delta = ik - \frac{4\pi}{t_E(k,k)\big|_{E=k^2}} \tag{4.16}$$

and the binding energies are given by the solutions of the corresponding homogeneous equation. As discussed in [12], Eq. (4.15) has no unique solution for $\Lambda \to \infty$ and requires renormalization. We regulate the equation with a sharp momentum cutoff Λ and absorb the cutoff dependence by introducing a momentum independent counterterm $\delta V(\Lambda)$

$$V_S(p,q) \to V_S(p,q) + \delta V(\Lambda) = 2\pi^2 c \left(\frac{\theta(p-q)}{p} + \frac{\theta(q-p)}{q} + \frac{H(\Lambda)}{\Lambda}\right)\,. \tag{4.17}$$

Demanding invariance of the zero-energy solution under changes of Λ, one finds

$$H(\Lambda) = \frac{1 - 2\nu\tan(\nu\ln(\Lambda/\Lambda_*))}{1 + 2\nu\tan(\nu\ln(\Lambda/\Lambda_*))} = -1 + \frac{2}{1 + 2\nu\tan(\nu\ln(\Lambda/\Lambda_*))}\,, \tag{4.18}$$

where Λ_* is a low-energy constant. Including this counterterm in Eq. (4.15) keeps all low-energy observables fixed. One can immediately see that the counterterm $H(\Lambda)$ displays a limit cycle with a preferred scaling factor $\exp(\pi/\nu)$ since the tangent is a periodic function with period π. If the cutoff Λ is changed by multiples of $\exp(\pi/\nu)$, the counterterm returns to the same value.

[2] A discussion of singular potentials can be found in [28].

The bound state spectrum satisfies a geometrical scaling relation analog to the Efimov case,

$$\frac{E^{(n)}}{E^{(n+1)}} = e^{2\pi/\nu}\,, \tag{4.19}$$

and presents an ideal test case for the application of SRG methods to limit cycles. In the following, we will investigate the limit cycle in the inverse square potential using the SRG framework.

We remark that the S-wave projected potential here has a different normalization than the S-wave potential in the partial wave momentum basis presented in section 4.1. The S-wave potentials differ by the multiplicative constant

$$V_2(p,p',l=0) = \frac{1}{2\pi^2} V_S(p,p')\,. \tag{4.20}$$

Using this relation the presented SRG equations can be applied directly. In order to compare to the framework in [12], we will consider $V_S(p,p')$ in the next section.

4.3 $1/R^2$ Potential and SRG

In this section, we consider the $1/R^2$ potential in the SRG framework. Since SRG transformations are unitary, all observables stay constant during the evolution by definition. This implies that in contrast to the explicit construction of the counterterm in the effective field theory treatment of the previous section, we need to extract a signal for the limit cycle from the evolved interaction. In order to define such a signal, we investigate the SRG evolution of the $1/R^2$ potential for critical and subcritical couplings and different generators. In the following we give all results in units of the free length scale l_0.

4.3.1 Qualitative Features

First, we consider the standard T generator for the SRG transformation. In Fig. 4.2, we show the evolution of the potential for $\nu = 9$ and an initial cutoff in Eq. (4.15) of $\Lambda = 20\ l_0^{-1}$. Introducing this regulator is required in order to ensure that Eq. (4.15) has a unique solution. Changing the value of Λ corresponds to changing the short-distance behavior of the starting interaction. Striking is the appearance of separated regions in the potential with positive and negative sign. To make them clearly visible, we choose a rather small maximum value for the coloring of the potential. As the evolution progresses, these regions are constantly emerging and vanishing while the total number of regions increases. At the beginning of the evolution, two positive valued regions appear. During the further progress more and more positive and negative regions emerge. The size of these structures also decreases, which is related to the general suppression of off-diagonal matrix elements in the SRG evolution for the T generator. In the last picture, one can clearly see the large number of small regions. We also note that this behavior occurs on a logarithmic scale of the flow parameter s.

To confirm that the appearance of these features is indeed related to the limit cycle, we have evolved $1/R^2$ potentials with subcritical coupling $c > -\frac{1}{4}$ where no limit cycle occurs and critical couplings $c \leq -\frac{1}{4}$ where it is present. In Fig. 4.3, four potentials are depicted, which were all evolved to $\lambda = 1\ l_0^{-1}$. All parameters of the potentials except for the coupling constant c are kept constant. For $c < -\frac{1}{4}$, the scaling factor is given by $\exp(\pi/\nu)$. Thus, if c approaches the critical value $-\frac{1}{4}$ the scaling factor diverges. In Fig. 4.3, the evolved potentials beneath and at the critical value do not exhibit these features. Only the effective diagonalization of V_S from the SRG transformation is clearly visible. For $\nu = 1$, two separated regions with opposite signs are observable up to this point in the evolution and for $\nu = 2$ several structures are already visible. This observation clearly supports our conjecture that the appearance of these features is related to the limit cycle.

Next, we consider the inverse and exponential generators. We expect a similar qualitative signature of the limit cycle. However, the alternative generators contain a free dimensionful parameter σ which divides the potential into two different regions. For small momenta compared to σ, the exponential and inverse generators reduce to the T generator. For large momenta, the generators approach zero and the evolution is suppressed. As an example, we have plotted the evolved potential for $\nu = 9$, $\Lambda = 20\ l_0^{-1}$ and $\sigma = 2\ l_0^{-1}$ in Fig. 4.4 for both the inverse and the exponential generator.

Notable is the fact that the features become compressed in a rather small area in the $k - k'$ plane, whose size depends on σ. We remark that the qualitative behavior of the exponential and inverse generators is very similar. Thus, we will not distinguish their traits here. As in the case of the standard T generator, the structures only appear if the coupling constant is supercritical.

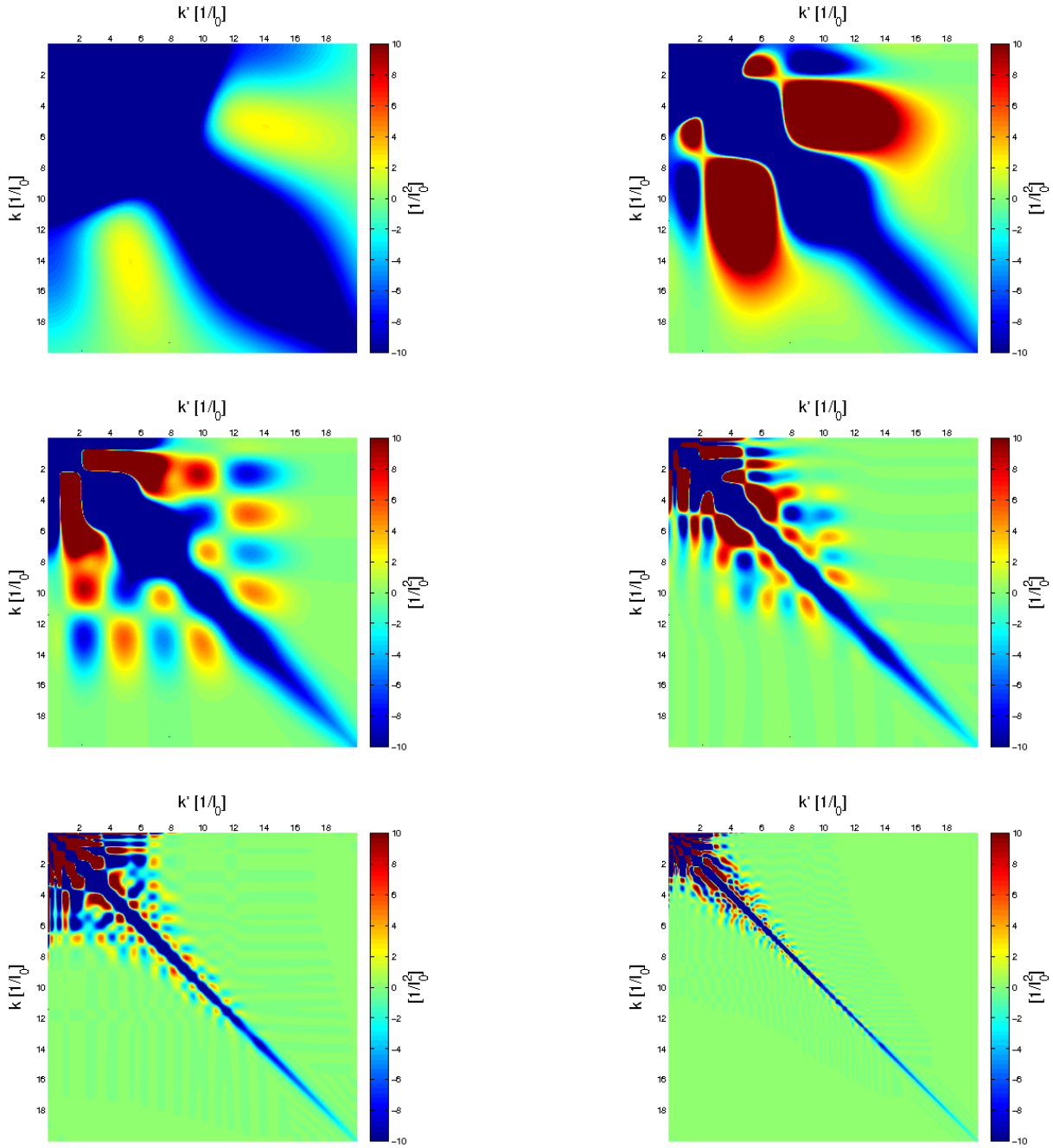

Figure 4.2.: Evolution of the S-wave $1/R^2$ potential for the T generator with $v = 9$ and initial cutoff $\Lambda = 20\ l_0^{-1}$. The potential $V_S(k, k', \lambda)$ is shown for $\lambda \approx$ 21.09, 13.67, 8.86, 5.74, 3.72 and 2.41 in units of $[1/l_0]$ from top left to bottom right.

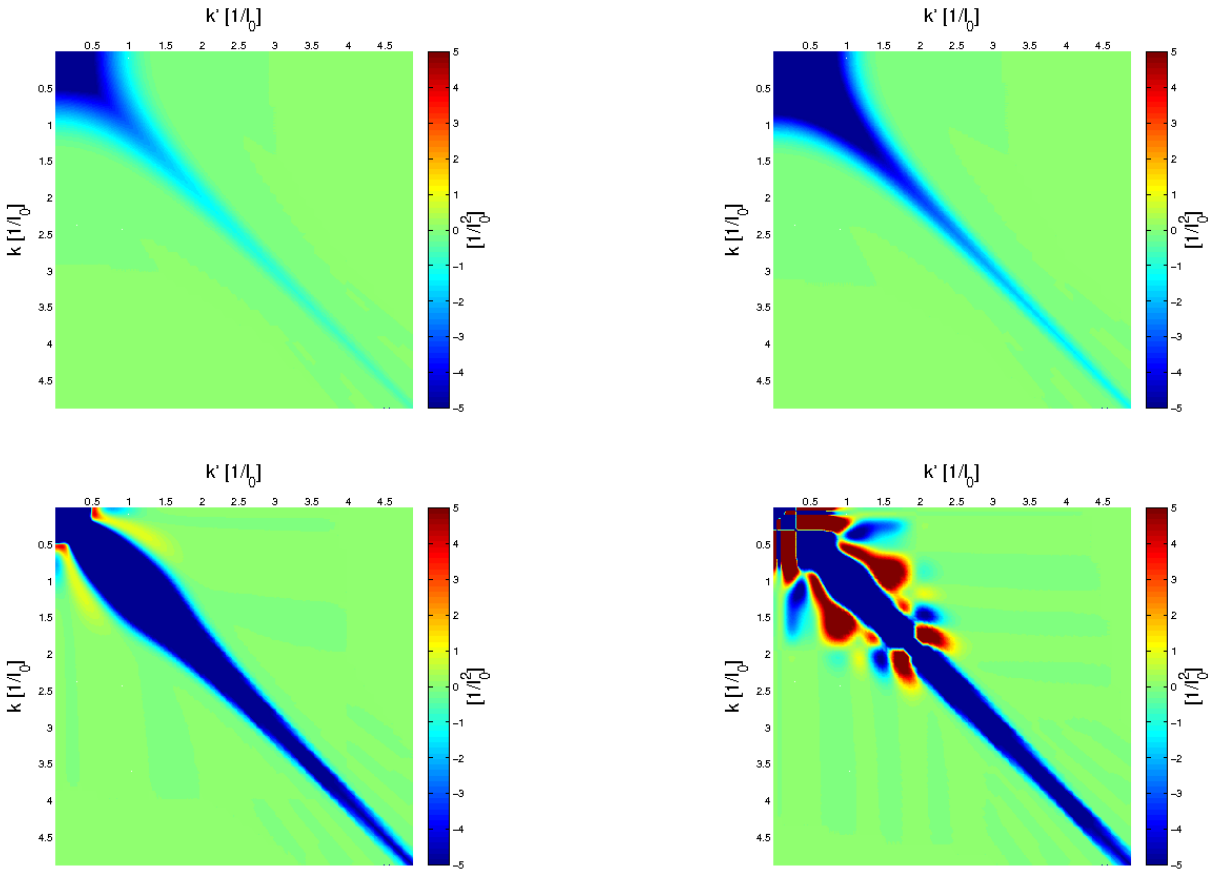

Figure 4.3.: S-wave $1/R^2$ potential evolved with the T generator to $\lambda = 1\ l_0^{-1}$ with initial $\Lambda = 20\ l_0^{-1}$. The potential strengths are $c = -0.125$, $c = -0.25$, $c = -0.25 - 1^2$ and $c = -0.25 - 2^2$ in the order from top left to bottom right.

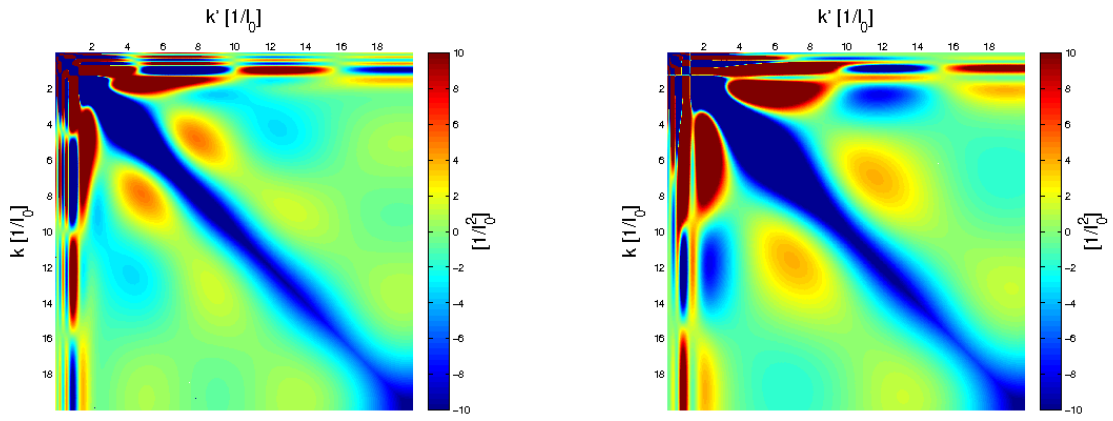

Figure 4.4.: Evolved $1/R^2$ potential with parameters $\nu = 9$, $\Lambda = 20\ l_0^{-1}$ and $\sigma = 2\ l_0^{-1}$ for G_e and G_i. Left panel: Evolution with the exponential generator G_e to $\lambda_a \approx 8.35\ l_0^{-1}$. Right panel: Evolution with the inverse generator G_i to $\lambda_a \approx 10.75\ l_0^{-1}$.

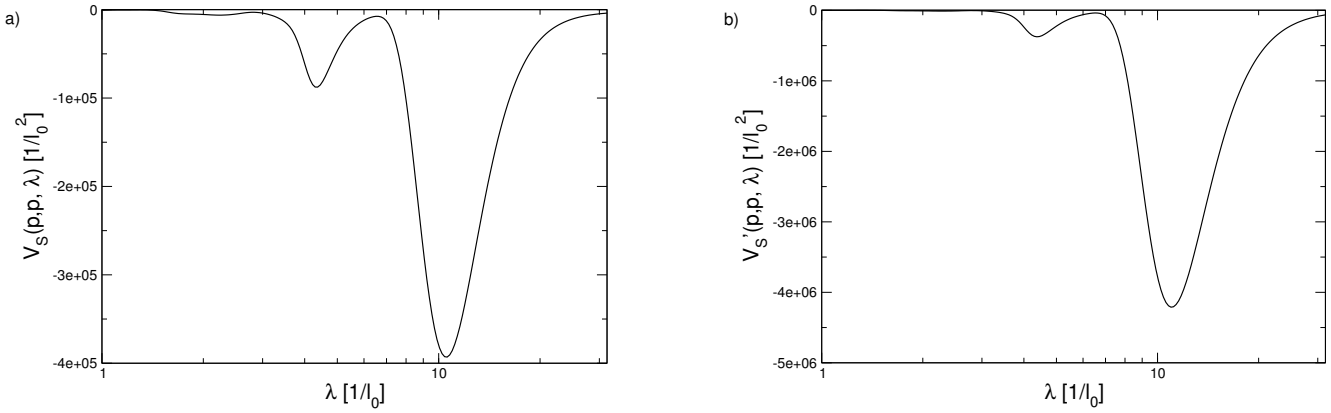

Figure 4.5.: a) Diagonal element $V_S(p,p,\lambda)$ in dependence on λ for $p \approx 0.84\, l_0^{-1}$. b) $(V_S(p,p,\lambda) - V_S(p,p,\lambda=\infty)) \cdot \lambda$ in dependence on λ for $p \approx 0.84\, l_0^{-1}$. The parameters of the potential are $\nu = 9$ and $\Lambda = 20\, l_0^{-1}$. The evolution was carried out with the standard T generator.

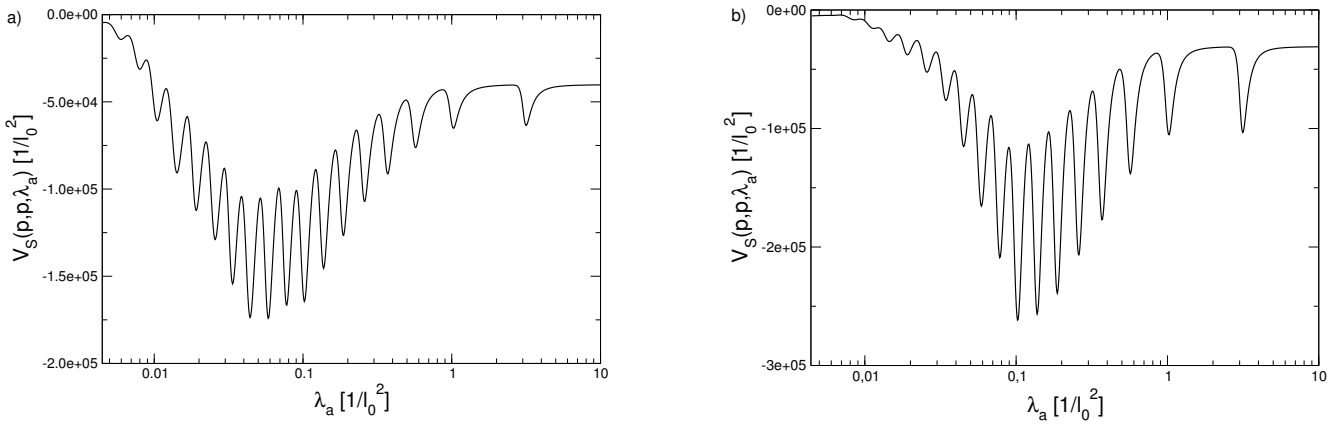

Figure 4.6.: Evolution of the diagonal elements $V_S(p,p,\lambda_a)$ with $\nu = 11$, $\Lambda = 30\, l_0^{-1}$ and $\sigma = 0.05\, l_0^{-1}$. a) Applied exponential generator with $p \approx 1.19\sigma$ b) Applied inverse generator evolved with $p \approx 1.55\sigma$.

Next we focus on the question of how to extract the discrete scaling factor as the main characteristic of the limit cycle from the evolved potential. To observe a log-periodic signal, we investigated several different strategies, which will be discussed in the following.

First, we examined the diagonal elements of the evolved potential in dependence on the flow parameter. This is motivated by the diagonalizing factor $\exp(-s(p^2-q^2)^2)$ from Eq. (3.26). On the diagonal of the potential matrix incoming and outgoing momenta are identical so that the exponential function is one. Hence, the diagonal elements are the only ones, which do not approach zero during the evolution. So, we expect a log-periodic signal to be most prominent on the diagonal. A similar strategy was followed by Glazek [29] in the analysis of a discrete model displaying a limit cycle.

We start with the standard T generator. In Fig. 4.5 a) a typical diagonal element is depicted in dependence on the flow parameter. The diagonal elements show some irregular oscillations but a clear signature of the limit cycle period can not be extracted. This is also true if we subtract the initial potential from the evolved potential and multiply by λ in order to isolate the analog of the counterterm $H(\lambda)$ from Eq. (4.18) above:

$$V_S'(p,p,\lambda) = (V_S(p,p,\lambda) - V_S(p,p,\lambda=\infty)) \cdot \lambda\,, \quad \text{where} \quad \lambda = s^{-1/4}\,. \tag{4.21}$$

In Fig. 4.5 b), we show $V_S'(p,p,\lambda)$ for the same diagonal matrix element as in Fig. 4.5 a). Again a clear signature of the limit cycle period could not be extracted.[3]

[3] This was also the case for the difference in Eq. (4.21) with different powers of λ.

oscillation	$\nu = 11$		$\nu = 5$	
	maxima	minima	maxima	minima
1	2.94	3.08	3.26	3.36
2	1.76	1.80	2.11	2.11
3	1.52	1.54	1.91	1.91
4	1.42	1.43	1.87	1.85
5	1.38	1.39	1.83	1.81
6	1.36	1.36	1.85	1.80
7	1.35	1.34	1.84	1.79
8	1.31	1.32		1.78
9	1.33	1.33		
10	1.34	1.33		
11	1.30	1.31		
12	1.33	1.31		
13	1.34	1.34		
14	1.38	1.35		
15	1.36	1.36		
16	1.33	1.31		
17		1.34		

Table 4.1.: Example of extracted ratios $\lambda_a^{(i)}/\lambda_a^{(i+1)}$ for the exponential generator, where the $\lambda_a^{(i)}$ are the flow parameter values of the maxima (minima) of $V_S(p,p,\lambda_a)$ with $p \approx 1.19\sigma$ for $\nu = 11$ and $\nu = 5$. The parameter values are $\Lambda = 30\, l_0^{-1}$ and $\sigma = 0.05\, l_0^{-1}$. The exact scaling factors are $\exp(\pi/11) \approx 1.33$ and $\exp(\pi/5) \approx 1.87$.

Using the standard T generator only very few irregular oscillations could be observed. In a second step, we therefore try the same strategy for the exponential and inverse generators that allow for a further evolution in s. Here, a completely different behavior is found. In Fig. 4.6, we plot a diagonal element with momentum p close to the parameter σ in dependence on the flow parameter for both generators. One can now clearly see regular oscillations for both generators. The graphs look like log-periodic functions combined with another function. The extracted distances between the maxima and minima are relatively constant, except for the first few oscillations, see Table 4.1 for explicit values of an example. The fact that the period of the first oscillations is distinctly larger, may be related to cutoff effects. The exact scaling factor is approached for subsequent oscillations.

The extracted periods of those curves depend on the strength of the initial potential ν. Larger values of ν result in smaller periods. We find that the extracted periods are in quite good agreement with the formula $\exp(\pi/\nu)$. The agreement is better for larger values of ν, where many oscillations can be seen.

We will now elaborate on the appearance of the oscillations on the entire diagonal. To this end, diagonal elements for four different momenta are displayed in Fig. 4.7 as a function of the flow parameter λ_a. The clearest oscillations can be extracted in the region where p is close to σ. For larger momenta p the amplitudes of the oscillations become smaller, cf. Fig. 4.7 c) and d). If p is further increased, the graph resembles a series of step functions but with a decreasing number of steps. Fig. 4.7 a) demonstrates that choosing momenta smaller than σ on the diagonal leads to a smaller number of clear oscillations. For small λ_a the graph looks planed and smeared. If p is further decreased, the number of oscillations with large amplitude is reduced and the graph resembles diagonal elements of potentials evolved with the T generator. This resemblance can be explained with the properties of the inverse and exponential generator. Remember that the inverse and exponential generators behave like the T generator in the low-energy region. Thus, the evolved diagonals should show similar behavior in this region.

This connection might also give a hint, why no signal is found for the T generator. A plausible answer is that the log-periodic function is superimposed by other SRG effects. For the exponential and inverse generator the evolution of the region with large momenta compared to σ is suppressed. This may reduce the overlaying effects.

We briefly return to Fig. 4.7 b). As one can see, for smaller λ_a the amplitudes of the oscillation decreases and at some point no oscillation is visible anymore. The number of observable oscillations is strongly dependent on σ. We found that oscillations can be seen until λ roughly approximates the value of σ. This may be due to the fact that matrix elements with binding momenta smaller than σ are located in a region whose evolution is similar to the T generator case. Assuming that the oscillations are correlated to the crossing from λ over binding momenta explains why choosing smaller values of σ leads to more visible oscillations for the exponential and inverse generator.

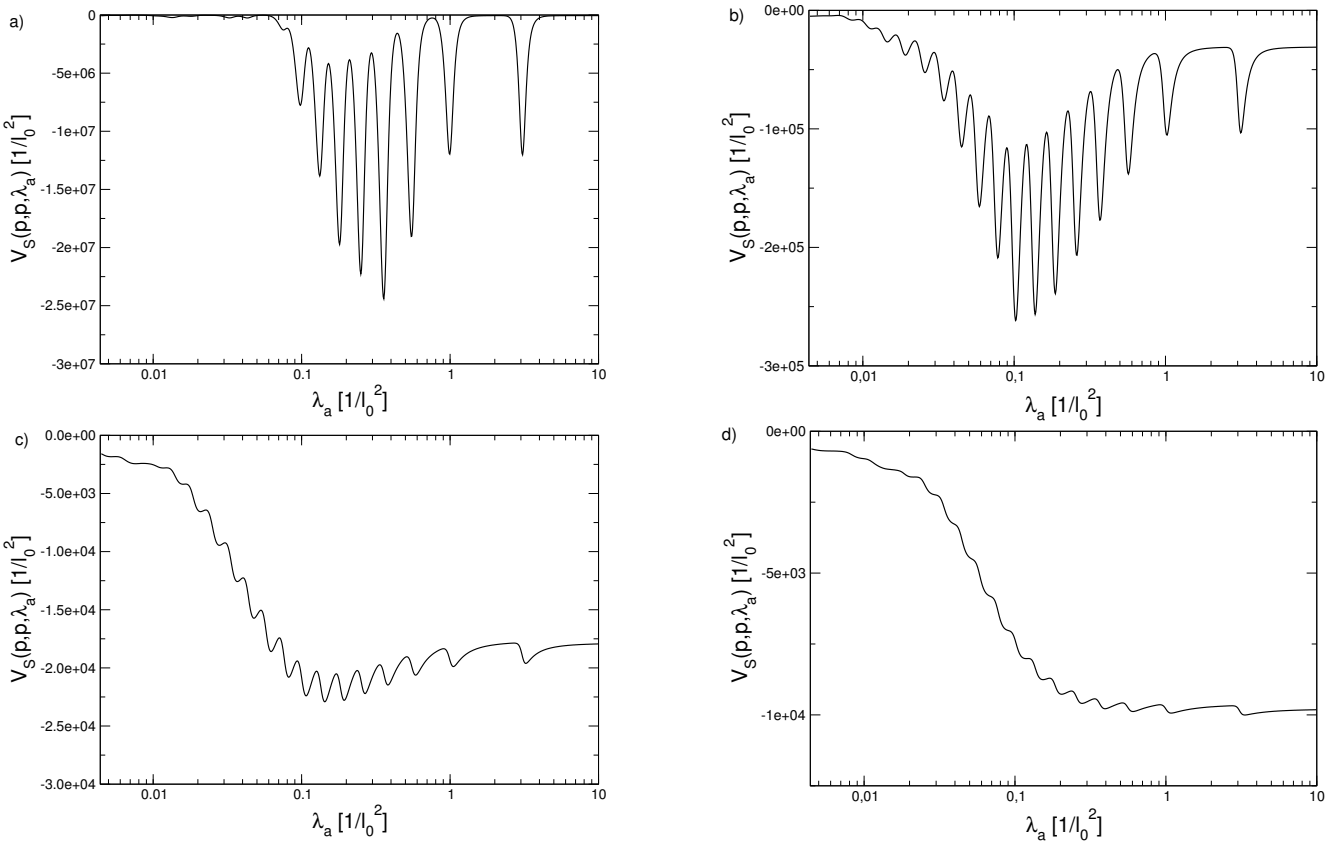

Figure 4.7.: Diagonal elements $V_S(p,p,\lambda_a)$ evolved with the inverse generator for four different momenta p with constants $\nu = 11$, $\Lambda = 30\, l_0^{-1}$ and $\sigma = 0.05\, l_0^{-1}$: a) $p \approx 0.96\sigma$, b) $p \approx 1.55\sigma$, c) $p \approx 2.68\sigma$, d) $p \approx 4.88\sigma$.

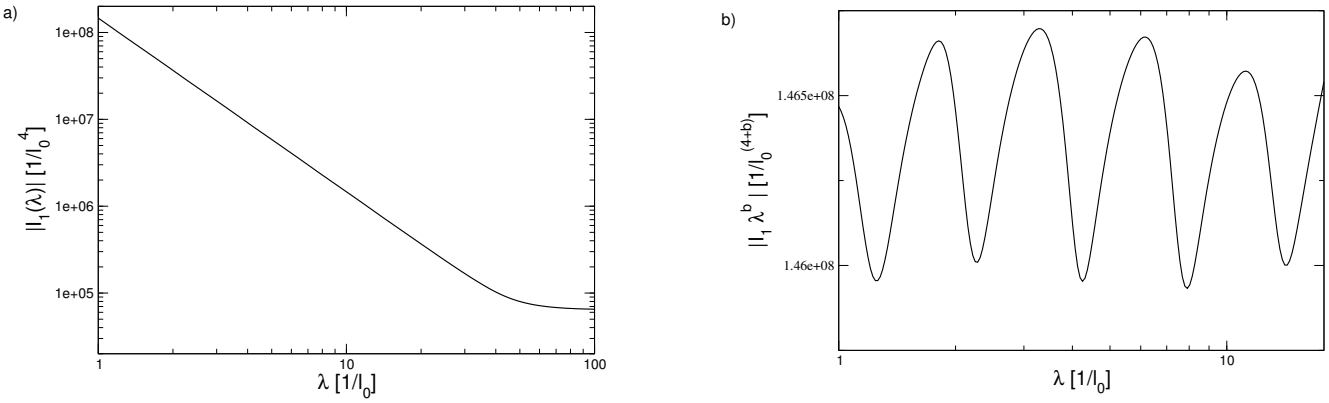

Figure 4.8.: a) Integral $|I_1(\lambda)|$ as a function of λ. b) $|I_1(\lambda) \cdot \lambda^b|$ as a function of λ with $b \approx 2$. The potential ($\nu = 9$, $\Lambda = 20\, l_0^{-1}$) was evolved with the T generator.

Besides the diagonal elements for the exponential and inverse generator, we examined the quantity $(V_S(p,p,\lambda) - V_S(p,p,\lambda=\infty)) \cdot \lambda^a$ for different powers a. But this did not result in the detection of a significantly improved signal.

In order to find also a log-periodic signal when the T generator is used, we tried another approach. Thinking of the evolved potential as an effective theory expansion

$$V_S(k,k',\lambda) = C_0(\lambda) + \frac{C_2(\lambda)}{2}(k^2 + k'^2) + \dots \tag{4.22}$$

our aim is to extract the C_0 constant as a function of λ. Since the matrix element $V_S(0,0,\lambda)$ is not accessible due to the singularity of the $1/R^2$ potential, we tried to extract the counterterm by extrapolation. However, this approach was not successful. We therefore examined the following two quantities

$$I_1(\lambda) \equiv \int\int dk dk' V_S(k,k',\lambda) \qquad \text{and} \qquad I_2(\lambda) \equiv \int dk V_S(k,k,\lambda)\,. \tag{4.23}$$

$I_1(\lambda)$ is the integral over the whole evolved potential and $I_2(\lambda)$ is the integral over the diagonal of the evolved potential. In Fig. 4.8 a) $I_1(\lambda)$ is plotted for the T generator in a double logarithmic representation. After the beginning of the evolution the graph goes to a polynomial function. A fit reveals the graph to be proportional to λ^{-b}, where b is very close to 2. We tested different potential strengths v and always found the exponent b to be very close to 2. A similar behavior was found for the integrated diagonal $I_2(\lambda)$. Certainly, the exponent in this case is very close to 4.

In the next step we divided $I_1(\lambda)$ by λ^{-b}, see Fig. $I_1(\lambda)$ b). There we could find an oscillatory function in the range, where I_1 behaves as λ^{-b}. In principle this is an expected behavior, an oscillatory function overlaid by another function of λ, in this case λ^{-b}. Puzzling to us is the fact that the period of this function is independent of the potential strength v, which is in distinct contrast to the RG approach. So we are not able to put this signal into context. Dividing $I_2(\lambda)$ by λ^{-b}, with $b \approx 4$, does not exhibit a comparable signal.

Using the inverse and exponential generator, $I_1(\lambda)$ and $I_2(\lambda)$ also display the functional dependence λ^{-b} after the starting phase of the transformation. The constant b is also found to be close to 2 resp. 4. However, $I_1(\lambda)$ and $I_2(\lambda)$ remain in this functional form only in a certain region of the flow parameter. For smaller λ the graph no longer follows a simple power law.

5 Three-body SRG

This chapter is concerned with the SRG transformation of a three-body system consisting of indistinguishable bosons. Because our aim is in general to find limit cycle signatures in the SRG evolution, we assume the simplest conditions for a three-body system which exhibits a limit cycle. We consider a pure S-wave separable two-body potential. The bosons are spinless and the total three-body angular momentum L is assumed to be zero. The mass m of the bosons is set to one as well as $\hbar = 1$. This chapter is structured as follows.

At first we define the applied basis states and discuss the theoretical framework. Subsequently, the SRG equation is computed for different generators and numerical implementation details are explained. Afterwards the appearance of the limit cycle in the RG framework in this system is briefly outlined. Finally, we consider the SRG evolution of this system with neglected and included induced three-body interactions.

5.1 Theoretical Framework

5.1.1 Basis States

We begin with the discussion of the employed basis states. For more information about the theoretical framework we refer to [30]. We consider a system of three bosons in momentum space with momenta $\mathbf{k_i}$. Instead of using these momenta in our calculations, we use Jacobi coordinates. They allow a separation of the total momentum $\mathbf{K} = \sum_{i=1}^{3} \mathbf{k_i}$. Because of translational invariance, we can set $\mathbf{K} = 0$. This already reduces the number of momentum variables. The two remaining coordinates are defined for the first Jacobi set as follows

$$\begin{aligned} \mathbf{p}_1 &= \tfrac{1}{2}(\mathbf{k}_2 - \mathbf{k}_3) \\ \mathbf{q}_1 &= \tfrac{2}{3}[\mathbf{k}_1 - \tfrac{1}{2}(\mathbf{k}_2 + \mathbf{k}_3)] \,. \end{aligned} \tag{5.1}$$

The $\mathbf{p}_1$ coordinate is defined as the relative momentum of the two-body subsystem composed of particles 2 and 3. The remaining momentum $\mathbf{q}_1$ is determined by the momentum of particle 1 relative to the center of mass momentum of the two-body subsystem. Using these coordinates, it is easy to incorporate the two-body potential between particles 2 and 3 because it depends on the relative momentum $\mathbf{p_1}$ only. Implementing the other two-body potentials is not that simple. We will come back to this later.

The momentum $\mathbf{p}_1$ depends on the relative momentum of particles 2 and 3. Alternatively, we could choose two different subsystems consisting of particles 1 and 2 or 1 and 3. Thus, in total there exist three sets of Jacobi coordinates. The other two are defined analogously

$$\begin{aligned} \mathbf{p}_2 &= \tfrac{1}{2}(\mathbf{k}_3 - \mathbf{k}_1) & \mathbf{p}_3 &= \tfrac{1}{2}(\mathbf{k}_1 - \mathbf{k}_2) \\ \mathbf{q}_2 &= \tfrac{2}{3}[\mathbf{k}_2 - \tfrac{1}{2}(\mathbf{k}_3 + \mathbf{k}_1)] & \mathbf{q}_3 &= \tfrac{2}{3}[\mathbf{k}_3 - \tfrac{1}{2}(\mathbf{k}_1 + \mathbf{k}_2)] \,. \end{aligned} \tag{5.2}$$

The basis states can now be written as $|\mathbf{p}\,\mathbf{q}\rangle_i$, where the index i denotes the Jacobi set and the total momentum is set to zero. The sets are of course equivalent $|\mathbf{p}_1\,\mathbf{q}_1\rangle_1 = |\mathbf{p}_2\,\mathbf{q}_2\rangle_2 = |\mathbf{p}_3\,\mathbf{q}_3\rangle_3$ and the momenta of the different sets can be converted using the following relation

$$\begin{aligned} \mathbf{p}_2 &= -\tfrac{1}{2}\mathbf{p}_1 - \tfrac{3}{4}\mathbf{q}_1 & \mathbf{p}_3 &= -\tfrac{1}{2}\mathbf{p}_1 + \tfrac{3}{4}\mathbf{q}_1 \\ \mathbf{q}_2 &= \mathbf{p}_1 - \tfrac{1}{2}\mathbf{q}_1 & \mathbf{q}_3 &= -\mathbf{p}_1 - \tfrac{1}{2}\mathbf{q}_1 \,. \end{aligned} \tag{5.3}$$

Since we consider spherically symmetric potentials, we can employ partial wave projected basis states, which eases the numerical calculation. The partial wave basis states are given by $|p\,q\,(lj)LM\rangle$, where we have dropped the index of the Jacobi set. Generally, if the Jacobi index is omitted, we refer to the first Jacobi set. The absolute values of $\mathbf{p}$ and $\mathbf{q}$ are p and q, respectively. The orbital angular momentum quantum number of particles 2 and 3 is denoted by l and the angular momentum number of the third particle relative to the pair is denoted by j. Together $\mathbf{l}$ and $\mathbf{j}$ couple to the total angular momentum of the system $\mathbf{L}$ with the magnetic quantum number M. The scalar product of these two representations is given by

$$\langle \mathbf{p}'\mathbf{q}'|pq(lj)LM\rangle = \frac{\delta(p-p')}{pp'}\frac{\delta(q-q')}{qq'}\mathscr{Y}_{lj}^{LM}(\hat{\mathbf{p}}',\hat{\mathbf{q}}')\,, \tag{5.4}$$

with the tensor product of two spherical harmonics

$$\mathscr{Y}_{lj}^{LM}(\hat{\mathbf{p}},\hat{\mathbf{q}}) = \left\{\mathbf{Y}_l(\hat{\mathbf{p}})\otimes\mathbf{Y}_j(\hat{\mathbf{q}})\right\}_{LM} = \sum_{m_1,m_2}\begin{bmatrix} l & j & L \\ m_1 & m_2 & M\end{bmatrix} Y_{l,m_1}(\hat{\mathbf{p}})Y_{j,m_2}(\hat{\mathbf{q}})\,, \tag{5.5}$$

which is an eigenfunction of $\mathbf{l}^2$, $\mathbf{j}^2$, $\mathbf{L}^2$ and L_z. The Clebsch–Gordan coefficient, where $\mathbf{l}$ and $\mathbf{j}$ couple to $\mathbf{L}$, is thereby written as

$$\begin{bmatrix} l & j & L \\ m_1 & m_2 & M\end{bmatrix}. \tag{5.6}$$

The normalization is assumed to be $\int\int\int d\mathbf{p}\,d\mathbf{q}\,d\mathbf{K}\,|\mathbf{p}\,\mathbf{q}\,\mathbf{K}\rangle\langle\mathbf{p}\,\mathbf{q}\,\mathbf{K}| = 1$. A complete set of states is given by

$$\sum_\alpha \int_0^\infty dp\,p^2 \int_0^\infty dq\,q^2 |p\,q\,\alpha\rangle\langle p\,q\,\alpha| \;= 1, \tag{5.7}$$

where α is an abbreviation for all angular momentum quantum numbers. The states are normalized according to

$$\langle p'q'(l'j')L'M'|pq\,(lj)\,LM\rangle = \frac{\delta(p-p')}{pp'}\frac{\delta(q-q')}{qq'}\delta_{ll'}\delta_{jj'}\delta_{LL'}\delta_{MM'}\,, \tag{5.8}$$

and the kinetic energy is given by

$$T|pq\,(lj)\,LM\rangle = (p^2+\tfrac{3}{4}q^2)|pq\,(lj)\,LM\rangle\,. \tag{5.9}$$

We consider identical spinless bosons. So, it is sufficient to employ only orbital angular momentum variables in the basis states and no spin variables. The symmetry properties of these three-body basis states are not that simple in contrast to the two-body system. Interchanging particles 2 and 3 in $|pq(lj)LM\rangle_1$ yields a factor of $(-1)^l$ [1]. Due to the bosonic nature of the system, only even values of l are allowed. Hence, the basis states are unchanged if the particles 2 and 3 are interchanged, as it should be. However, the states are not symmetric under the interchange of particle 1 with particle 2 or 3. Therefore, the states are only partially symmetric. Due to the implementation of the two-body potentials we do not apply fully symmetrized states.

5.1.2 Permutation Operator

In the following computations it is useful to apply permutation operators. The application of the permutation operators eases the calculation of the binding energy, which is presented in appendix B, and the SRG evolution. We define the permutation operator P_{ij} which permutes particles i and j. Using the permutation operator the different Jacobi states can be related to each other in the following way

$$\begin{aligned} P_{12}P_{23}|\mathbf{pq}\rangle_1 &= |\mathbf{pq}\rangle_2 \\ P_{13}P_{23}|\mathbf{pq}\rangle_1 &= |\mathbf{pq}\rangle_3\,. \end{aligned} \tag{5.10}$$

The two-body potentials $V_2^{(i)}$ can also be converted

$$\begin{aligned} V_2^{(2)} &= P_{13}P_{23}V_2^{(1)}P_{12}P_{23} \\ V_2^{(3)} &= P_{12}P_{23}V_2^{(1)}P_{13}P_{23}\,. \end{aligned} \tag{5.11}$$

The potential $V_2^{(i)}$ thereby denotes the two-body interaction between particles j and k with $i \neq j \neq k$. These relations are advantageous because $V_2^{(2)}$ and $V_2^{(3)}$ have to be implemented in the employed Jacobi set. Some additional relations, which will be needed later, are

$$\begin{aligned} P_{13}P_{23}P_{13}P_{23} &= P_{12}P_{23} \\ P_{12}P_{23}P_{12}P_{23} &= P_{13}P_{23} \\ P_{23}P_{12}P_{23}P_{23} &= P_{13}P_{23}\,. \end{aligned} \tag{5.12}$$

[1] Here, we explicitly indicate the Jacobi set of the basis state to prevent misconceptions.

Next we consider the permutation operators in the partial wave basis. It can be shown that the permutation operators $P_{13}P_{23}$ and $P_{12}P_{23}$ are equal in this basis

$$\langle pq\alpha|P_{12}P_{23}|p'q'\alpha'\rangle = \langle pq\alpha|P_{13}P_{23}|p'q'\alpha'\rangle \,. \tag{5.13}$$

We follow the proof in [30]. For identical spinless bosons

$$\begin{aligned}\langle pq\alpha|P_{13}P_{23}|p'q'\alpha'\rangle =& \langle pq\alpha|P_{23}P_{12}P_{23}P_{23}|p'q'\alpha'\rangle = (-1)^{l}(-1)^{l'}\langle pq\alpha|P_{12}P_{23}|p'q'\alpha'\rangle \\ =& \langle pq\alpha|P_{12}P_{23}|p'q'\alpha'\rangle\end{aligned} \tag{5.14}$$

holds. In the first step we use the last relation of Eq. (5.12). Then the outer permutation operators P_{23} are applied to the states. The states are unchanged but we obtain the factors $(-1)^l$ and $(-1)^{l'}$. The overall sign is nevertheless positive. Consequently, the two matrix elements are the same. Due to this relation we can rewrite the potentials in a simpler form. Keep in mind that his relation holds for the first Jacobi set.

We define the permutation operator P to be

$$P = P_{12}P_{23} + P_{13}P_{23} \tag{5.15}$$

so that we can write for convenience the potentials in the following form in the partial wave basis

$$\begin{aligned}V_2^{(2)} =& \tfrac{1}{4}PV_2^{(1)}P \\ V_2^{(3)} =& \tfrac{1}{4}PV_2^{(1)}P \,.\end{aligned} \tag{5.16}$$

Certainly the matrix element $\langle pq\alpha|P|p'q'\alpha'\rangle$ has to be computed. The elements are presented in appendix A.

5.2 SRG Equations

In this section we derive the SRG equation for the three-body system. Compared to the two-body system this is more laborious. We start with the derivation using the T generator. The derivation for the T generator in one dimension can e.g. also be found in [31, 32]. Afterwards we discuss the appearance of disconnected terms as well as the consequences for the exponential generator. Subsequently, we derive the SRG equation for two different approaches concerning the exponential generator.

5.2.1 T Generator

We apply the kinetic energy generator in the three-body system

$$\eta_3 = [T, H] = [T, \overline{V}_2 + V_3] \,, \tag{5.17}$$

with the total two-body potential $\overline{V}_2$ which is defined by

$$\overline{V}_2 = \sum_{i=1}^{3} V_2^{(i)} \,. \tag{5.18}$$

The SRG equation is thus given by

$$\begin{aligned}\frac{dH}{ds} =& [[T, \overline{V}_2 + V_3], T + \overline{V}_2 + V_3] \\ =& 2TV_3T - V_3TT - TTV_3 + TV_3V_3 + V_3V_3T - 2V_3TV_3 \\ &+ TV_3\overline{V}_2 + \overline{V}_2V_3T + T\overline{V}_2V_3 + V_3\overline{V}_2T - 2V_3T\overline{V}_2 - 2\overline{V}_2TV_3 \\ &- \overline{V}_2TT - TT\overline{V}_2 + 2T\overline{V}_2T + T\overline{V}_2\overline{V}_2 + \overline{V}_2\overline{V}_2T - 2\overline{V}_2T\overline{V}_2 \,.\end{aligned} \tag{5.19}$$

The derivative of the Hamilton operator is the sum of the following derivatives

$$\frac{dH}{ds} = \frac{dV_3}{ds} + \frac{dV_2^{(1)}}{ds} + \frac{dV_2^{(2)}}{ds} + \frac{dV_2^{(3)}}{ds} \,. \tag{5.20}$$

The evolution of the two-body potential is determined by the two-body system. We are therefore only interested in the evolution of V_3. The last line of Eq. (5.19) contains terms of the two-body evolution. These terms can be subtracted, which will be explained in more detail in the next section. We thus obtain

$$\frac{dV_3}{ds} = O_3 + O_{23} + O_2 \,, \tag{5.21}$$

with

$$\begin{aligned} O_3 =& 2TV_3T - V_3TT - TTV_3 + TV_3V_3 + V_3V_3T - 2V_3TV_3 \\ O_{23} =& \sum_{i=1}^{3} \left(TV_3V_2^{(i)} + V_2^{(i)}V_3T + TV_2^{(i)}V_3 + V_3V_2^{(i)}T - 2V_3TV_2^{(i)} - 2V_2^{(i)}TV_3 \right) \\ O_2 =& \sum_{i\neq j} \left(TV_2^{(i)}V_2^{(j)} + V_2^{(i)}V_2^{(j)}T - 2V_2^{(i)}TV_2^{(j)} \right) \,. \end{aligned} \tag{5.22}$$

The operators are labeled in the following way. The operator O_3 contains all terms which include the three-body potential V_3 only. The terms in O_{23} are products of the two- and three-body potentials and O_2 contains only two-body potentials. Therefore, O_2 is the origin of the induced three-body interactions. If there is no initial three-body potential, O_3 and O_{23} are zero. However, O_2 is nonzero and leads to the induction of V_3. The operator O_3 has a structure similar to the right hand side of the two-body SRG equation (4.2) and contains the diagonalizing terms.

When the operators are expressed in the partial wave momentum basis, there is a difficulty. As already mentioned, the basis corresponds to one set i of the Jacobi coordinates. Therefore, only $V_2^{(i)}$ can be expressed in this basis in a simple manner. As a consequence, we use the permutation operator, introduced in the previous section, to express the other two-body potentials in terms of the selected $V_2^{(1)}$. As throughout this thesis we make the arbitrary choice to employ the first Jacobi set. Therefore, if no upper index is given in the three-body system, $V_2 = V_2^{(1)}$. Next we will rewrite the operators using the permutation operator P. The operator O_3 is unchanged since it contains no two-body potential. We obtain

$$\begin{aligned} O_2 =& T(\tfrac{1}{2}PV_2PV_2 + \tfrac{1}{2}V_2PV_2P + \tfrac{1}{4}PV_2PV_2P) + (\tfrac{1}{2}PV_2PV_2 + \tfrac{1}{2}V_2PV_2P + \tfrac{1}{4}PV_2PV_2P)T \\ & - PV_2PTV_2 - V_2TPV_2P - \tfrac{1}{2}PV_2PTV_2P \end{aligned}$$

$$\begin{aligned} O_{23} =& TV_3V_2 + V_2V_3T + TV_2V_3 + V_3V_2T - 2V_3TV_2 - 2V_2TV_3 \\ & + \tfrac{1}{2}(TV_3PV_2P + PV_2PV_3T + TPV_2PV_3 + V_3PV_2PT) - V_3TPV_2P - PV_2PTV_3 \,. \end{aligned} \tag{5.23}$$

Keep in mind that the kinetic energy T commutes with the permutation operator. Before we continue with the exponential generator, we discuss the subject of disconnected terms in the SRG equation.

5.2.2 Disconnected Contributions

In this section we change the notation a bit to make the distinction between the different subsystems more obvious. The Hamiltonian is now written as

$$H = T + V_2^{12} + V_2^{13} + V_2^{23} + V_3 \,, \tag{5.24}$$

where the upper index of the two-body potential V_2 now denotes the two involved particles. The kinetic energy can be split up into $T = T_{12} + T_3 = T_{13} + T_2 = T_{23} + T_1$. This partition of the kinetic energy is defined according to the Jacobi coordinates: $T_{23} \leftrightarrow p_1^2$ and $T_1 \leftrightarrow \frac{3}{4}q_1^2$.

This section is concerned with the treatment of disconnected terms, which arise in the three-body SRG equation. "Disconnected" in this context means contributions with two interacting particles and one unaffected spectator particle. Using the T generator, an exemplary disconnected term is $TV_2^{12}V_2^{12}$. Since the potential acts only between particles 1 and 2, the third particle is unaffected. Applying a momentum basis, we obtain a delta function for the incoming and outgoing momenta of particle 3. These delta functions cause problems, when the SRG equation is solved numerically. Hence, we try to avoid these disconnected terms.

First we regard the situation when the T generator is used. Because we are only interested in the appearance of disconnected terms, the connected terms are not explicitly stated. In addition, the SRG equation is symmetric under the interchange of particles. Consequently, we obtain the same disconnected terms for every particle combination. For ease of reading, we write down the disconnected terms explicitly for the particle combination 12 and abbreviate the others by

$\{12 \to 23\}$ and $\{12 \to 13\}$. This notation means that only the indices have to be replaced. The SRG differential equation can now be written as

$$\begin{aligned}\frac{dH}{ds} &= [[T, V_2^{12} + V_2^{23} + V_2^{13} + V_3], T + V_2^{12} + V_2^{23} + V_2^{13} + V_3] \\ &= \{2TV_2^{12}T - V_2^{12}TT - TTV_2^{12} - 2V_2^{12}TV_2^{12} + TV_2^{12}V_2^{12} + V_2^{12}V_2^{12}T\} \\ &\quad + \{12 \to 23\} + \{12 \to 13\} + (\text{connected terms})\,. \end{aligned} \tag{5.25}$$

From the two-body evolution we know

$$\begin{aligned}\frac{dV_2^{12}}{ds} &= [[T_{12}, V_{12}], T + V_{12}] \\ &= 2T_{12}V_2^{12}T_{12} - V_2^{12}T_{12}T_{12} - T_{12}T_{12}V_2^{12} - 2V_2^{12}T_{12}V_2^{12} + T_{12}V_2^{12}V_2^{12} + V_2^{12}V_2^{12}T_{12}\,. \end{aligned} \tag{5.26}$$

We want to compute the equation for the evolution of the three-body potential V_3. Therefore, the two-body SRG equations have to be subtracted from Eq. (5.25). It is obvious that Eq. (5.26) is contained in Eq. (5.25). Consequently, these terms cancel out directly. Next we compute what happens to the remaining disconnected parts

$$\begin{aligned}\frac{dV_3}{ds} &= \frac{dH}{ds} - \frac{dV_2^{12}}{ds} - \frac{dV_2^{23}}{ds} - \frac{dV_2^{13}}{ds} = \\ &= \{2(T_{12}V_2^{12}T_3 + T_3V_2^{12}T_{12} + T_3V_2^{12}T_3) - V_2^{12}(T_{12}T_3 + T_3T_{12} + T_3T_3) - (T_{12}T_3 + T_3T_{12} + T_3T_3)V_2^{12} \\ &\quad - 2V_2^{12}T_3V_2^{12} + T_3V_2^{12}V_2^{12} + V_2^{12}V_2^{12}T_3\} + \{12 \to 23\} + \{12 \to 13\} + (\text{connected terms}) \\ &= \{2T_3(T_{12}V_2^{12} + V_2^{12}T_{12} + V_2^{12}T_3) - T_3V_2^{12}(2T_{12} + T_3) - T_3(2T_{12} + T_3)V_2^{12} \\ &\quad - 2T_3V_2^{12}V_2^{12} + T_3V_2^{12}V_2^{12} + T_3V_2^{12}V_2^{12}\} + \{12 \to 23\} + \{12 \to 13\} + (\text{connected terms}) \\ &= 0 + (\text{connected terms})\,, \end{aligned} \tag{5.27}$$

where we have used that T_3 and V_2^{12} commute since the motion of the center of mass of particles 1 and 2 as well as the motion of particle 3 is unaffected by the potential V_2^{12}. All disconnected terms are contained in the two-body evolution and the rest cancels out. Thus, only connected terms contribute to the evolution of the three-body potential V_3 and no delta functions which cause numerical problems are present anymore.

A different situation is given when the exponential generator is applied. To avoid distracting details, we set $\sigma = 1$ for the remainder of this section. The SRG equation can be written as

$$\begin{aligned}\frac{dH}{ds} &= [[-e^{-T}, V_2^{12} + V_2^{23} + V_2^{13} + V_3], T + V_2^{12} + V_2^{23} + V_2^{13} + V_3] \\ &= \{-e^{-T}V_2^{12}T - TV_2^{12}e^{-T} + V_2^{12}e^{-T}T + Te^{-T}V_2^{12} - e^{-T}V_2^{12}V_2^{12} - V_2^{12}V_2^{12}e^{-T} + 2V_2^{12}e^{-T}V_2^{12}\} \\ &\quad + \{12 \to 23\} + \{12 \to 13\} + (\text{connected terms})\,. \end{aligned} \tag{5.28}$$

The two-body SRG equation is given by

$$\begin{aligned}\frac{dV_2^{12}}{ds} &= -e^{-T_{12}}V_2^{12}T_{12} - T_{12}V_2^{12}e^{-T_{12}} + V_2^{12}e^{-T_{12}}T_{12} + T_{12}e^{-T_{12}}V_2^{12} \\ &\quad - e^{-T_{12}}V_2^{12}V_2^{12} - V_2^{12}V_2^{12}e^{-T_{12}} + 2V_2^{12}e^{-T_{12}}V_2^{12}\,. \end{aligned} \tag{5.29}$$

The crucial difference to the T generator case is that the exponential function e^{-T} can not be separated into a sum consisting of a contribution of particles 1 and 2 and a contribution of particle 3, like $T = T_{12} + T_3$. Instead we obtain a product $\exp(-T) = \exp(-T_{12}) \cdot \exp(-T_3)$. We rewrite Eq. (5.28) as follows

$$\begin{aligned}\frac{dH}{ds} &= \{-e^{-T_{12}}e^{-T_3}V_2^{12}(T_{12} + T_3) - (T_{12} + T_3)V_2^{12}e^{-T_{12}}e^{-T_3} + V_2^{12}e^{-T_{12}}e^{-T_3}(T_{12} + T_3) \\ &\quad + (T_{12} + T_3)e^{-T_{12}}e^{-T_3}V_2^{12} - e^{-T_{12}}e^{-T_3}V_2^{12}V_2^{12} - V_2^{12}V_2^{12}e^{-T_{12}}e^{-T_3} + 2V_2^{12}e^{-T_{12}}e^{-T_3}V_2^{12}\} \\ &\quad + \{12 \to 13, T_3 \to T_2\} + \{12 \to 23, T_3 \to T_1\} + (\text{connected terms}) \\ &= \Big\{e^{-T_3}\Big(-e^{-T_{12}}V_2^{12}(T_{12} + T_3) - (T_{12} + T_3)V_2^{12}e^{-T_{12}} + V_2^{12}e^{-T_{12}}(T_{12} + T_3) \\ &\quad + (T_{12} + T_3)e^{-T_{12}}V_2^{12} - e^{-T_{12}}V_2^{12}V_2^{12} - V_2^{12}V_2^{12}e^{-T_{12}} + 2V_2^{12}e^{-T_{12}}V_2^{12}\Big)\Big\} \\ &\quad + \{12 \to 13, T_3 \to T_2\} + \{12 \to 23, T_3 \to T_1\} + (\text{connected terms}) \\ &= \left\{+e^{-T_3}\left(\frac{dV_2^{12}}{ds}\right) - e^{-T_3}e^{-T_{12}}V_2^{12}T_3 - e^{-T_3}T_3V_2^{12}e^{-T_{12}} + e^{-T_3}V_2^{12}e^{-T_{12}}T_3 + e^{-T_3}T_3e^{-T_{12}}V_2^{12}\right\} \\ &\quad + \{12 \to 13, T_3 \to T_2\} + \{12 \to 23, T_3 \to T_1\} + (\text{connected terms}) \\ &= \left\{+e^{-T_3}\left(\frac{dV_2^{12}}{ds}\right)\right\} + \{12 \to 13, T_3 \to T_2\} + \{12 \to 23, T_3 \to T_1\} + (\text{connected terms})\,. \end{aligned} \tag{5.30}$$

From this follows

$$\frac{dV_3}{ds} = \frac{dH}{ds} - \frac{dV_2^{12}}{ds} - \frac{dV_2^{23}}{ds} - \frac{dV_2^{13}}{ds} = \left\{ \left(e^{-T_3} - 1\right) \left(\frac{dV_2^{12}}{ds} \right) \right\} + \{12 \to 13, T_3 \to T_2\} + \{12 \to 23, T_3 \to T_1\} + (\text{connected terms}) \,. \tag{5.31}$$

Obviously, the disconnected terms persist in the SRG equation for the three-body potential in contrast to the T generator case. Thus, we can not apply the exponential generator in this way in the three-body system.

We have tried two different methods to solve this problem. The first is to modify the generator

$$\eta = [-e^{-T}, V_2^{12} + V_2^{23} + V_2^{13} + V_3] \to [-e^{-T}, V_3] + [-e^{-T_{12}}, V_2^{12}] + [-e^{-T_{23}}, V_2^{23}] + [-e^{-T_{13}}, V_2^{13}] \,. \tag{5.32}$$

These commutators were chosen such that all disconnected terms cancel in the SRG equation except for those which add up to the two-body SRG equation. Hence, in the evolution of the three-body potential only connected terms appear and the evolution of the two-body potential is unaffected. However, the connected terms are also modified.

A different approach is to modify the evolution of the two-body potential in the three-body system [33]. The original SRG equation,

$$\frac{dV_2^{12}}{ds} = [[-e^{-T_{12}}, V_{12}], T_{12} + V_{12}] \,, \tag{5.33}$$

is modified by using the full three-body kinetic energy operator $T = T_{12} + T_3$

$$\frac{dV_2^{12}}{ds} = [[-e^{-T}, V_2^{12}], T + V_2^{12}] = [[-e^{-T_{12}-T_3}, V_2^{12}], T_{12} + T_3 + V_2^{12}] \,. \tag{5.34}$$

Of course, the equations of the two other potentials V_2^{23} and V_2^{13} are modified in the same way. This procedure leaves the connected terms unaffected. But the two-body potentials now have an additional momentum dependency. In the next two sections we discuss the SRG equations derived with both methods.

5.2.3 Subtracted Exponential Generator

We return to the usual notation and start with the two-body evolution. The generator of the two-body system is unchanged and given by

$$\eta_2 = \left[-\sigma^2 e^{-T_p^{(i)}/\sigma^2}, V_2^{(i)} \right] \,, \tag{5.35}$$

where $T_p^{(i)}$ is the relative kinetic energy of subsystem i. It is given by $T_p^{(i)} = p_i^2$ with the Jacobi momentum p_i. The SRG equation is given by

$$\begin{aligned} \frac{dV_2^{(i)}}{ds} =& \left[\left[-\sigma^2 e^{-T_p^{(i)}/\sigma^2}, V_2^{(i)} \right], T_p^{(i)} + V_2^{(i)} \right] \\ =& \sigma^2 \left(-e^{-T_p^{(i)}/\sigma^2} V_2^{(i)} T_p^{(i)} + V_2^{(i)} e^{-T_p^{(i)}/\sigma^2} T_p^{(i)} + T_p^{(i)} e^{-T_p^{(i)}/\sigma^2} V_2^{(i)} - T_p^{(i)} V_2^{(i)} e^{-T_p^{(i)}/\sigma^2} \right. \\ & \left. - e^{-T_p^{(i)}/\sigma^2} V_2^{(i)} V_2^{(i)} - V_2^{(i)} V_2^{(i)} e^{-T_p^{(i)}/\sigma^2} + 2 V_2^{(i)} e^{-T_p^{(i)}/\sigma^2} V_2^{(i)} \right) \,. \end{aligned} \tag{5.36}$$

This is the usual SRG equation for the exponential generator in the two-body system. As mentioned in the previous section, we modify the generator of the three-body system in order to eliminate the disconnected terms. The three-body generator is then defined by

$$\eta_3 = [-\sigma^2 e^{-T/\sigma^2}, V_3] + \sum_i [-\sigma^2 e^{-T_p^{(i)}/\sigma^2}, V_2^{(i)}] \,. \tag{5.37}$$

The computation is straightforward and we finally obtain

$$\frac{dV_3}{ds} = O_3 + O_{23} + O_2 \,, \tag{5.38}$$

with

$$
\begin{aligned}
O_3 =& \sigma^2 \left(-e^{-T/\sigma^2} V_3 T + V_3 e^{-T/\sigma^2} T + T e^{-T/\sigma^2} V_3 - T V_3 e^{-T/\sigma^2} - e^{-T/\sigma^2} V_3 V_3 - V_3 V_3 e^{-T/\sigma^2} + 2 V_3 e^{-T/\sigma^2} V_3 \right) \\
O_{23} =& \sigma^2 \sum_i \Big(-e^{-T/\sigma^2} V_3 V_2^{(i)} + V_3 e^{-T/\sigma^2} V_2^{(i)} + V_2^{(i)} e^{-T/\sigma^2} V_3 - V_2^{(i)} V_3 e^{-T/\sigma^2} \\
& - e^{-T_p^{(i)}/\sigma^2} V_2^{(i)} V_3 + V_2^{(i)} e^{-T_p^{(i)}/\sigma^2} V_3 + V_3 e^{-T_p^{(i)}/\sigma^2} V_2^{(i)} - V_3 V_2^{(i)} e^{-T_p^{(i)}/\sigma^2} \Big) \\
O_2 =& \sigma^2 \sum_{i \neq j} \left(-e^{-T_p^{(i)}/\sigma^2} V_2^{(i)} V_2^{(j)} + V_2^{(i)} e^{-T_p^{(i)}/\sigma^2} V_2^{(j)} + V_2^{(j)} e^{-T_p^{(i)}/\sigma^2} V_2^{(i)} - V_2^{(j)} V_2^{(i)} e^{-T_p^{(i)}/\sigma^2} \right) .
\end{aligned}
$$

The structure of the operators is similar to the T generator case. In principle the operators differ only in the appearing functions of the kinetic energy for the different generators. The expressions of the operators using the permutation operator are thus straightforward. Therefore, we do not state this representation explicitly.

5.2.4 Exponential Generator with modified Two-body Evolution

In this section we present a second method to avoid the disconnected terms in the three-body evolution. The generator of the three-body evolution is not changed. Instead the two-body generator is modified. We use the kinetic energy of the three-body system in the two-body generator

$$
\eta_2 = \left[-\sigma^2 e^{-T/\sigma^2}, V_2^{(i)} \right] , \tag{5.39}
$$

which yields

$$
\begin{aligned}
\frac{dV_2^{(i)}}{ds} =& \sigma^2 e^{-T_q^{(i)}/\sigma^2} \Big(-e^{-T_p^{(i)}/\sigma^2} V_2^{(i)} T_p^{(i)} + V_2^{(i)} e^{-T_p^{(i)}/\sigma^2} T_p^{(i)} + T_p^{(i)} e^{-T_p^{(i)}/\sigma^2} V_2^{(i)} \\
& - T_p^{(i)} V_2^{(i)} e^{-T_p^{(i)}/\sigma^2} - e^{-T_p^{(i)}/\sigma^2} V_2^{(i)} V_2^{(i)} - V_2^{(i)} V_2^{(i)} e^{-T_p^{(i)}/\sigma^2} + 2 V_2^{(i)} e^{-T_p^{(i)}/\sigma^2} V_2^{(i)} \Big) .
\end{aligned} \tag{5.40}
$$

Here we have used the following notation for the three-body kinetic energy: $T = T_p^{(i)} + T_q^{(i)}$. The energy $T_q^{(i)}$ is the kinetic energy of the third particle relative to the subsystem i. If the momentum states of subsystem i are given by $|\mathbf{p}\,\mathbf{q}\rangle_i$, the energies can be written as $T_p^{(i)} = p^2$ and $T_q^{(i)} = \frac{3}{4} q^2$.

The evolution of the two-body potential $V_2^{(i)}$ now depends on an additional parameter, which is given by the kinetic energy of the spectator particle $T_q^{(i)}$. We therefore evolve the two-body potential in the three-body basis. The matrix elements in the partial wave momentum basis thus obey the following relation

$$
\langle pq(lj)LM | V_2 | p'q'(l'j')L'M \rangle = \langle pl | V_2(q) | p'l' \rangle \frac{\delta(q-q')}{qq'} \delta_{ll'} \delta_{jj'} \delta_{LL'} \delta_{MM'} . \tag{5.41}
$$

The three-body generator is given by

$$
\eta_3 = [-\sigma^2 e^{-T/\sigma^2}, H] . \tag{5.42}
$$

This leads to the following terms

$$
\begin{aligned}
O_3 =& \sigma^2 \left(-e^{-T/\sigma^2} V_3 T + V_3 e^{-T/\sigma^2} T + T e^{-T/\sigma^2} V_3 - T V_3 e^{-T/\sigma^2} - e^{-T/\sigma^2} V_3 V_3 - V_3 V_3 e^{-T/\sigma^2} + 2 V_3 e^{-T/\sigma^2} V_3 \right) \\
O_{23} =& \sigma^2 \sum_{i=1}^{3} \Big(-e^{-T/\sigma^2} V_3 V_2^{(i)} - e^{-T/\sigma^2} V_2^{(i)} V_3 - V_2^{(i)} V_3 e^{-T/\sigma^2} \\
& - V_3 V_2^{(i)} e^{-T/\sigma^2} + 2 V_3 e^{-T/\sigma^2} V_2^{(i)} + 2 V_2^{(i)} e^{-T/\sigma^2} V_3 \Big) \\
O_2 =& \sigma^2 \sum_{i \neq j} \left(-e^{-T/\sigma^2} V_2^{(i)} V_2^{(j)} - V_2^{(i)} V_2^{(j)} e^{-T/\sigma^2} + 2 V_2^{(i)} e^{-T/\sigma^2} V_2^{(j)} \right)
\end{aligned} \tag{5.43}
$$

for the three-body evolution.

5.3 Operators in the Partial Wave Basis

In this section we compute the operators O_3, O_{23} and O_2 for the T generator in our partial wave basis $|pq\,(lj)\,LM\rangle$. Since the expressions become very lengthy, we explicitly state only some terms from which the total operator can easily be deduced. The terms for the other generators are similar. In principle the kinetic energy function has to be adapted and for the exponential generator with modified two-body equation one has to take care of the additional momentum dependence.

We will now explicitly employ our assumptions of the system. We consider identical spinless bosons, which interact by a pure S-wave two-body potential. Thus, l has to be even. The total angular momentum L of the three-body system is conserved and assumed to be $L = 0$. Since the total angular momentum is zero, $l = j$ holds.

The matrix elements of the pure S-wave potential V_2 can be written as

$$\langle pq\,(lj)LM|V_2|p'q'\,(l'j')L'M'\rangle = \langle p|V_2|p'\rangle \frac{\delta(q-q')}{qq'}\delta_{ll'}\delta_{jj'}\delta_{LL'}\delta_{MM'}\delta_{l0}\,, \tag{5.44}$$

with $\langle p\,l=0\,m_l=0|V_2|p'\,l'=0\,m_{l'}=0\rangle =: \langle p|V_2|p'\rangle$. Keep in mind that V_2 represents $V_2^{(1)}$ and we use the first Jacobi set in the partial wave basis so that this simple relation holds. Additionally, we abbreviate the basis states

$$|pq\,(l)\rangle := |pq\,(l\,j=l)L=0\,M=0\rangle\,. \tag{5.45}$$

The operator O_3 can be expressed in this compact form

$$\begin{aligned}\langle pq\,(l)|O_3|p'q'\,(l')\rangle =& -(p^2+\tfrac{3}{4}q^2-p'^2-\tfrac{3}{4}q'^2)^2\,\langle pq\,(l)|V_3|p'q'\,(l')\rangle \\ &+(p^2+\tfrac{3}{4}q^2+p'^2+\tfrac{3}{4}q'^2)\sum_{l''}\int dp''dq''p''^2q''^2\langle pq\,(l)|V_3|p''q''\,(l'')\rangle\langle p''q''\,(l'')|V_3|p'q'\,(l')\rangle \\ &-2\sum_{l''}\int dp''dq''p''^2q''^2(p''+\tfrac{3}{4}q'')\langle pq\,(l)|V_3|p''q''\,(l'')\rangle\langle p''q''\,(l'')|V_3|p'q'\,(l')\rangle\,. \end{aligned}\tag{5.46}$$

Keep in mind that the angular momentum l'' is summed over even values. The expressions for the terms in O_2 and O_{23} are much more complex. We therefore write down basic parts of them. The next term is also readily to determine

$$\langle pq(l)|V_2TV_3|p'q'(l')\rangle = \int dk\,k^2T(k;q)\langle p|V_2|k\rangle\langle kq\,(0)|V_3|p'q'\,(l')\rangle\delta_{l0}\,, \tag{5.47}$$

with $T(p;q) = p^2 + \frac{3}{4}q^2$. Next we consider terms including the permutation operator.

$$\begin{aligned}\langle p\,q\,(l)|PV_2PV_2|p'\,q'\,(l')\rangle =& \sqrt{[l]}\int_{-1}^{1}dx\int_{-1}^{1}dy P_l(x)\langle\pi_1(p,q,x)|V_2|\tilde{\pi}_1(\pi_2(p,q,x),q',y)\rangle \\ &\times\langle\tilde{\pi}_2(\pi_2(p,q,x),q',y)|V_2|p'\rangle\,\delta_{l'0}\end{aligned}\tag{5.48}$$

$$\begin{aligned}\langle p\,q\,(l)|PV_2TPV_2|p'\,q'\,(0)\rangle =& \sqrt{[l]}\int_{-1}^{1}dx\int_{-1}^{1}dy\,P_l(x)\langle\pi_1(p,q,x)|V_2|\tilde{\pi}_1(\pi_2(p,q,x),q',y)\rangle \\ &\times\langle\tilde{\pi}_2(\pi_2(p,q,x),q',y)|V_2|p'\rangle\,T(\tilde{\pi}_2(\pi_2(p,q,x),q',y);q')\end{aligned}\tag{5.49}$$

$$\begin{aligned}\langle p\,q\,(l)|PV_2PV_2P|p'\,q'\,(l')\rangle =& \sqrt{[l][l']}\int_{-1}^{1}dx\int_{-1}^{1}dy\int_{-1}^{1}dz P_l(x)P_{l'}(y) \\ \times\langle\pi_1(p,q,x)|V_2|\tilde{\pi}_1(\pi_2(p,q,x),\pi_2(p',q',y),z)\rangle&\langle\tilde{\pi}_2(\pi_2(p,q,x),\pi_2(p',q',y),z)|V_2|\pi_1(p',q',y)\rangle\end{aligned}\tag{5.50}$$

$$\begin{aligned}\langle p\,q\,(l)|PV_2TPV_2P|p'\,q'\,(l')\rangle =& \sqrt{[l][l']}\int_{-1}^{1}dx\int_{-1}^{1}dy\int_{-1}^{1}dz P_l(x)P_{l'}(y) \\ \times\langle\pi_1(p,q,x)|V_2|\tilde{\pi}_1(\pi_2(p,q,x),\pi_2(p',q',y),z)\rangle&\langle\tilde{\pi}_2(\pi_2(p,q,x),\pi_2(p',q',y),z)|V_2|\pi_1(p',q',y)\rangle \\ &\times T(\tilde{\pi}_1(\pi_2(p,q,x),\pi_2(p',q',y),z);\pi_2(p,q,x))\end{aligned}\tag{5.51}$$

$$\langle p\,q\,(l)|PV_2PV_3|p'\,q'\,(l')\rangle = 2\int dq_2\,q_2^2 \sum_{l_2=0,2,4,\ldots}\int_{-1}^{1} dx \int_{-1}^{1} dy\,\sqrt{[l]}P_l(x)$$
$$b_{l_2}(\pi_2(p,q,x),q_2,\tilde{\pi}_2(\pi_2(p,q,x),q_2,y),y)\langle\pi_1(p,q,x)|V_2|\tilde{\pi}_1(\pi_2(p,q,x),q_2,y)\rangle$$
$$\langle\tilde{\pi}_2(\pi_2(p,q,x),q_2,y)\,q_2\,(l_2)|V_3|p'\,q'\,(l')\rangle \tag{5.52}$$

$$\langle p\,q\,(l)|PV_2PTV_3|p'\,q'\,(l')\rangle = 2\int dq_2\,q_2^2 \sum_{l_2=0,2,4,\ldots}\int_{-1}^{1} dx \int_{-1}^{1} dy\,\sqrt{[l]}P_l(x)$$
$$b_{l_2}(\pi_2(p,q,x),q_2,\tilde{\pi}_2(\pi_2(p,q,x),q_2,y),y)\langle\pi_1(p,q,x)|V_2|\tilde{\pi}_1(\pi_2(p,q,x),q_2,y)\rangle$$
$$\langle\tilde{\pi}_2(\pi_2(p,q,x),q_2,y)\,q_2\,(l_2)|V_3|p'\,q'\,(l')\rangle\,T(\tilde{\pi}_2(\pi_2(p,q,x),q_2,y);q_2) \tag{5.53}$$

The bracket $[l]$ is defined as $(2l+1)$ and the definitions of the function $b_{l'}(q,q',p',x)$ and the pi functions are given in appendix A. The other appearing terms can straightforwardly be deduced from this.

5.4 Numerical Implementation Details

The most relevant analytic expressions for the three-body SRG evolution have been calculated. However, the differential equation has to be solved numerically. In this section we discuss some numerical details of the implementation. Similar to the two-body case the differential equations can be solved using Runge-Kutta methods. The GSL package as well as MATLAB contain ordinary differential equation solving routines, which implement these methods. The main problem is to compute the different terms of O_2 and O_{23}. The computation of O_3 is rather simple. It is just a generalization of the two-body computation. The biggest problems arise from the use of the permutation operator. We will now explain this in more detail. The Jacobi momenta as well as the potentials are discretized. The permutation operators lead to the appearance of pi functions like $\pi_1(p,q,x)$, which are defined in appendix A. Except for some special cases the momenta returned from these functions are not part of the discretized momentum set. Therefore, the potential has to be evaluated on points between the grid. Only for the initial potential an analytic expression is given. During the SRG evolution the off-grid points of the evolved potential are unknown. These points can approximately be determined by an interpolation. For this purpose, we apply splines. Let $f(x)$ be a function which is known only for certain discrete values x_i. The function can now be approximated by

$$f(x) \approx \sum_i S_i(x) f(x_i)\,, \tag{5.54}$$

where $S_i(x)$ are known spline functions [30]. We apply special modified cubic spline functions given in [34].

The interpolation naturally leads to an increase of the numerical errors. As a side remark, note that the permutation operator also implies an additional integration over the angle in the pi functions. In contrast, in O_3 no permutation operator is present. Therefore, off-grid points do not appear and just integrations over the grid points have to be performed, which implies smaller numerical errors.

Our aim is to detect a signature of the limit cycle in the three-body evolution. It is necessary that the evolution passes several periods of the cycle before it is stopped. Consequently, large values of the flow parameter s should be reached. Due to the computational runtime this condition can be fulfilled in the two-body system with the $1/R^2$ potential. In the three-body system it is more difficult. Instead of one, there are now two momentum variables in the incoming and outgoing state. Hence, the potential matrix is now a $N^2 \times N^2$ instead of an $N \times N$ matrix, where N is the number of grid points. For included angular momenta larger than zero the matrix obviously grows.

It is essential to perform the computations in a high-performance way. Implementing loops in order to execute the integrations is therefore not practicable. Writing the SRG equations in a matrix form so that only matrix operations like addition or multiplication have to be executed leads to an enormous computational speedup. Therefore, we use this method for numerical computations. However, applying matrix calculations has a disadvantage in this case regarding the numerical error. Not all of the appearing terms in the SRG equation can be written in a matrix form with ordinary matrix operations. That is why we decided to use double interpolations [32]. Double interpolation in this context means that we have to interpolate the argument of the splines. Using double interpolation the operations can be expressed as matrix operations. We found this to be the best trade-off regarding numerical error and computational runtime. We explain the double interpolation in the following example. We regard the term

$$\int dq_2\,q_2^2\langle\pi_1(p,q,x)|V_2|\tilde{\pi}_1(\pi_2(p,q,x),q_2,y)\rangle\langle\tilde{\pi}_2(\pi_2(p,q,x),q_2,y)\,q_2\,(l_2)|V_3|p'\,q'\,(l')\rangle\,.$$

Applying splines for the off-grid points of the potentials and approximating the integration by a summation yields

$$S_a(\pi_1(p,q,x))\langle p_a|V_2|p_b\rangle S_b(\tilde{\pi}_1(\pi_2(p,q,x),p_d,y))S_c(\tilde{\pi}_2(\pi_2(p,q,x),p_d,y))\,w_d\,p_d^2\langle p_c\,p_d\,(l_2)|V_3|p'q'(l')\rangle\,, \tag{5.55}$$

with the weights w_i and where we used the same discretization p_i for both Jacobi momenta. As usual, repeated indices are summed over. Because the external momenta p and q appear in the middle spline functions S_b and S_c, it is not possible to rewrite this term in a matrix form using matrix operations like multiplication or element-wise matrix multiplication with matrices of the size $N^2 \times N^2$. Interpolating the argument of S_b and S_c gives

$$S_a(\pi_1(p,q,x))S_e(\pi_2(p,q,x))\langle p_a|V_2|p_b\rangle S_b(\tilde{\pi}_1(p_e,p_d,y))S_c(\tilde{\pi}_2(p_e,p_d,y))\,w_d\,p_d^2\langle p_c p_d(l_2)|V_3|p'q'(l')\rangle\,. \tag{5.56}$$

This expression can now be rewritten using matrices

$$S_1 * V_2 * S_2 * (V_3 .* W)\,, \tag{5.57}$$

where $*$ denotes a matrix multiplication and $.*$ an element-wise matrix multiplication. We define $a = \lfloor i/N \rfloor$, $b = \lfloor j/N \rfloor$, $c = i \mod N$ and $d = j \mod N$ with the Gaussian brackets $\lfloor\ \rfloor$. The matrices are then defined as follows

$$\begin{aligned}
(V_2)_{ij} =& \langle p_a|V_2|p_b\rangle\,\delta_{cd} \\
(V_3)_{ij} =& \langle p_a p_c\,(l_2)|V_3|p_b, p_d\,(l')\rangle \\
(S_1)_{ij} =& S_b(\pi_1(p_a,p_c,x))S_d(\pi_2(p_a,p_c,x)) \\
(S_2)_{ij} =& S_a(\tilde{\pi}_1(p_c,p_d,y))S_b(\tilde{\pi}_2(p_c,p_d,y)) \\
(W)_{ij} =& w_d\,p_d^2\,.
\end{aligned} \tag{5.58}$$

Thereby, we have also discretized the external momenta p, q, p' and q'. We focused on the spline functions in this example. Therefore, we assumed the angular momentum variables l_2, l' as well as the angle related variables x, y to be fixed. In the complete program the matrices have to be expanded in size to allow for arbitrary angular momentum and angular integrations have to be performed numerically. But this procedure is straightforward.

As demonstrated, the SRG equation can be written in a matrix form, which allows for faster calculations if double interpolation is used. However, it is essential to take care of the numerical errors. During the evolution, good indicators are the three-body binding energies. They are calculated using the Faddeev equations, see appendix B. The SRG transformation is a unitary transformation. Therefore, the binding energies should remain constant during the evolution. In the two-body system the deviations are in general negligible. This does not apply to the three-body system. There significant deviations can be observed. We will come back to this later. In this context we want to mention the role of the angular momenta. The initial potential is a pure S-wave two-body interaction and no initial three-body interaction is present. During the evolution a three-body force is induced. We consider a vanishing total angular momentum in the initial three-body system. The SRG equation decouples for the different total angular momenta. Therefore, the induced three-body potential has also zero total angular momentum. As already mentioned, there is still one free angular momentum variable l of the two-body subsystem in this case. During the evolution three-body potentials with arbitrary large and even l are induced. For the numerical implementation it is therefore necessary to set a maximum angular momentum l_{max} and neglect all potentials with higher angular momenta. Of course this leads to new errors. If the deviations from the initial binding energies become too large, the reason can be a too small l_{max}. However, the matrices are very large even for few mesh points. Accordingly, the computational runtime is also long. Hence, the maximal angular momentum is also restricted by the computational runtime.

5.5 Separable Potential

After the discussion of the theoretical framework we move on and briefly discuss the considered system. Similar to the two-body chapter, we present the limit cycle traits under an RG transformation. The subsequent sections are concerned with the results of the SRG evolution of the three-body system for two different cases. First, we neglect the induced three-body potentials so that $V_3 = 0$ for all s. Second, the induced three-body potentials are included. In both cases we search for signatures of the limit cycle.

Since our aim is to generally find and examine signatures of the limit cycle in SRG evolved potentials, we regard a simple three-body system, which exhibits the limit cycle, as test case. We briefly recap the properties of the considered system. The system consists of three indistinguishable spinless bosons, which interact via a pure S-wave two-body potential. The total angular momentum of the three-body system is assumed to be zero. The considered potential is a separable two-body potential consisting of a coupling constant regularized by a Gaussian cutoff

$$\langle \mathbf{p}|V_2|\mathbf{q}\rangle = -g_2 \exp(-(p^2+q^2)/\Lambda^2)\,. \tag{5.59}$$

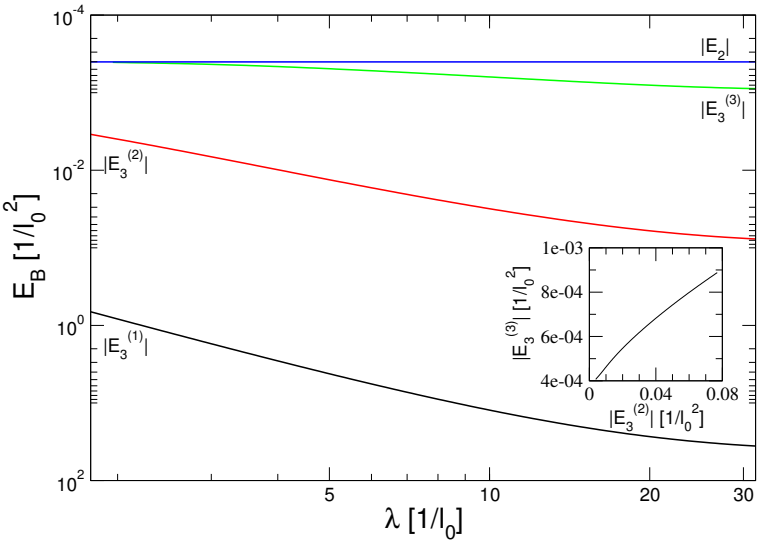

Figure 5.1.: T generator evolved binding energy spectrum as a function of λ. The blue line depicts the two-body binding energy $|E_2|$. In the inset $|E_3^{(3)}|$ is plotted against $|E_3^{(2)}|$. The cutoff of the separable potential is $\Lambda = 30\, l_0^{-1}$ and the coupling constant g_2 is chosen such that $|E_2| \approx 4.0 \cdot 10^{-4}\,[1/l_0^2]$.

The parameters are tuned to obtain large scattering lengths. This system of three particles with large scattering length is discussed in detail in chapter 8.2. However, the applied frameworks differ. Here, we consider a quantum mechanical framework with a regularized potential, whereas in chapter 8.2 this system is regarded in a field theoretical framework. Certainly, the traits of the system remain the same. Therefore, we will only briefly discuss the system at this point. For more information about the limit cycle in this quantum mechanical framework we refer to [35].

The renormalization of this separable potential in the three-body space is similar to the renormalization of the $1/R^2$ potential. To keep three-body low-energy observables constant, when changing the cutoff parameter Λ, a three-body potential is introduced

$$\langle \mathbf{p}\,\mathbf{q}|V_3|\mathbf{p}'\mathbf{q}'\rangle = g_3 \exp(-(p^2 + \tfrac{3}{4}q^2 + p'^2 + \tfrac{3}{4}q'^2)/\Lambda^2)\,, \tag{5.60}$$

with the incoming $\mathbf{p}, \mathbf{q}$ and the outgoing $\mathbf{p}', \mathbf{q}'$ Jacobi momenta. The coupling constant $g_2(\Lambda)$ is fully determined by renormalizing the two-body system. Thus, $g_3(\Lambda)$ is determined by three-body low energy constants.

The limit cycle manifests itself in $g_3(\Lambda)$. It can be shown that in the limit $\Lambda \to \infty$ the coupling constant exhibits the following behavior

$$g_3(\Lambda) = \frac{c}{\Lambda^4} \frac{\sin(s_0 \ln(\Lambda/\Lambda_*) - \arctan(1/s_0))}{\sin(s_0 \ln(\Lambda/\Lambda_*) + \arctan(1/s_0))}\,, \tag{5.61}$$

where Λ_* denotes a three-body parameter. The constant $s_0 \approx 1.0062$ is a transcendental number, which determines the period of the limit cycle. Note that g_3 vanishes for special values of Λ_* so that the three-body force is not coercive needed to calculate three-body observables. This justifies why we can set the three-body potential to zero at the starting point of our evolution.

5.5.1 SRG without induced Three-body Potential

In this section we evolve the separable two-body potential with large scattering length, but neglect the induced three-body potentials, i.e. $V_3(\lambda) = 0$. Hence, all two-body observables will stay constant but the three-body observables will no longer be conserved because of the violation of unitarity. We focus on the three-body bound states and apply again three different generators: T, exponential and inverse.

In Fig. 5.1 the three-body spectrum is plotted as a function of the flow parameter, where we employed the T generator. There the following behavior can be observed: All three bound states loose continuously energy. When the lowest bound state $E_3^{(3)}$ falls below the constant two-body binding energy, it vanishes. Next we apply the inverse and exponential generators. In Fig. 5.2 the evolution of the three-body spectrum in the unitary limit $a = \pm\infty$ is depicted for the inverse generator. One directly recognizes a striking difference to the T generator case. The ground state $E_3^{(1)}$ still continuously looses binding energy, but the behavior of the second $E_3^{(2)}$ and third $E_3^{(3)}$ bound state is different. At the beginning of the evolution they gain binding energy until a maximum is reached, then they continuously loose binding energy. Usually, we

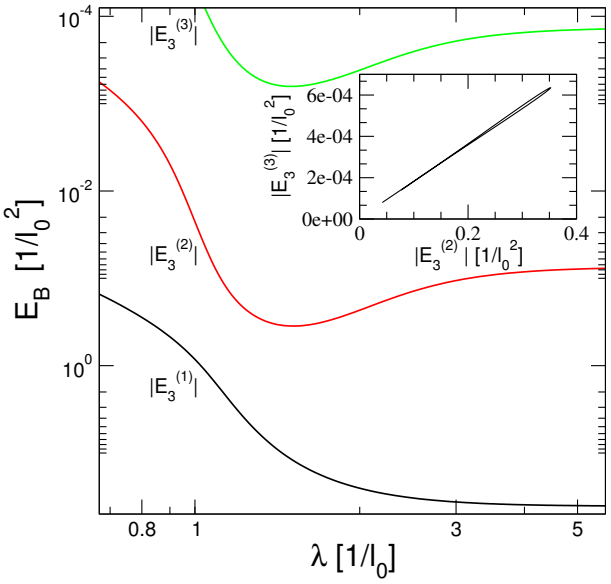

Figure 5.2.: Evolution of the three-body spectrum in the unitary limit. The inverse generator is applied with $\sigma = 1\ l_0^{-1}$. In the inset $|E_3^{(3)}|$ is plotted against $|E_3^{(2)}|$. The cutoff of the separable potential is $\Lambda = 30\ l_0^{-1}$ and E_B is the binding energy.

found the lowest bound state $E_3^{(3)}$ to disappear first, similar to the conventional RG-treatment of the separable potential when the cutoff is lowered. If the scattering length is finite, the shallowest bound state vanishes at the two-body binding energy threshold E_2. We remark that the shallowest bound state $E_3^{(3)}$ does not vanish at the minimal depicted energy in Fig. 5.2. This state vanishes for significantly smaller binding energies. However, the numerical errors become large for binding energies smaller than the depicted ones. Therefore, we have plotted the shallowest bound state only in the energy region where the numerical errors are not larger than a few percent. The numerical accuracy of the other two depicted states is significantly better. In principle, the states should disappear at the zero energy threshold in the unitary limit.

For Fig. 5.3 we employed the exponential generator with the same parameters. There we observe a similar behavior of the binding energies. Certainly, no bound state has disappeared up to this point in the evolution. For comparison, the spectrum evolved with the T generator in the unitary limit is depicted with the same parameters in Fig. 5.4. Note that the state $E_3^{(3)}$ is only depicted in the energy region where the numerical errors are not larger than a few percent.

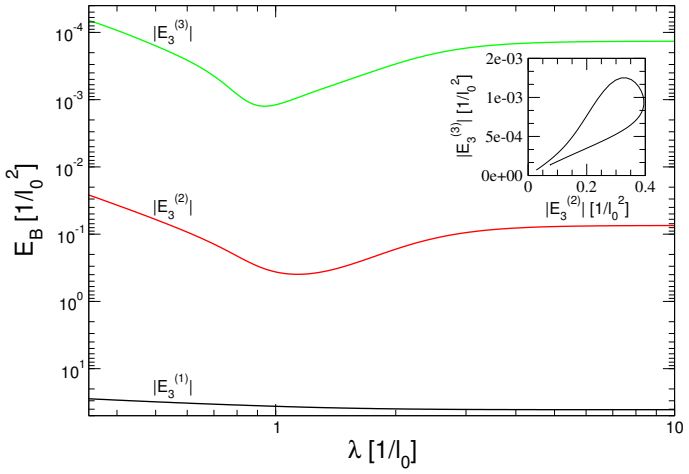

Figure 5.3.: Three-body binding energy spectrum evolved in the unitary limit. The exponential generator is applied with $\sigma = 1\ l_0^{-1}$. In the inset $|E_3^{(3)}|$ is plotted against $|E_3^{(2)}|$. The cutoff of the separable potential is $\Lambda = 30\ l_0^{-1}$.

Additionally, we have plotted $E_3^{(3)}(\lambda)$ against $E_3^{(2)}(\lambda)$ in the inset of several graphs. For the exponential and inverse generator we obtain a broad and a narrow loop, respectively. These two are typical loop forms, which we observed. There is however a restriction. The appearance of the loops is related to the above mentioned behavior of the bound

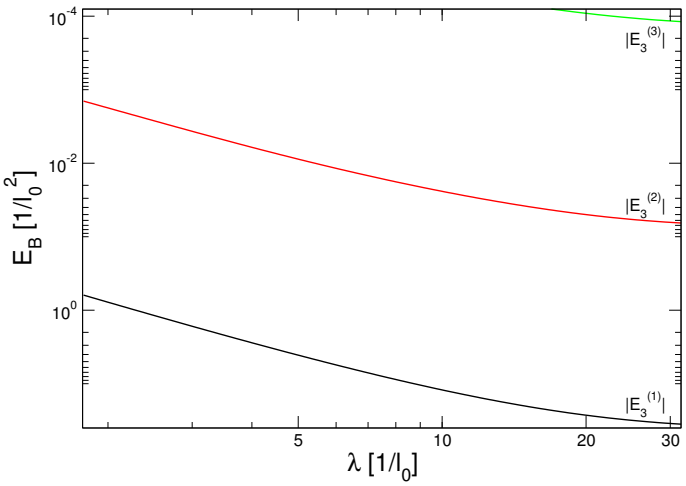

Figure 5.4.: Binding energy spectrum evolved with the T generator in the unitary limit. The cutoff of the separable potential is $\Lambda = 30\ l_0^{-1}$.

state spectra for the exponential and inverse generator. Thus, the evolution parameter σ has to be small enough in order to obtain these loops. Otherwise, for large σ, the inverse and exponential generators will reduce to the T generator. Additionally, σ influences the form of the spectrum and the loop. Generally, a larger value of σ leads to a narrower curve. This is plausible because there has to be a continuous transition to the T generator case.

Since the two-body observables remain constant during the evolution, we expect that the depicted curves in the insets are close to the universal scaling curve [1], which is a straight line for this case[2]. Therefore, the narrow loop meets our expectations, but not the broad loop. Apparently, the parameter σ affects the deviations from unitarity in the evolution.

We have to note that a loop can not be observed if $E_3^{(1)}$ is plotted against one of the other two bound states. This is related to the fact that the ground state $E_3^{(1)}$ continuously looses binding energy in contrast to the other states. We assume this to be due to cutoff effects. For all other states except the ground state, we expect the same behavior when their binding energies are plotted against each other. However, we are only able to obtain three bound states with the use of the Faddeev equation in this SRG framework for large scattering lengths.

In the case of neglected induced three-body potentials, we can evolve to small values of the flow parameter λ. However, the scaling factor in this system is ≈ 22.7 and hence relatively large. In contrast, the scaling factor of the $1/R^2$ potential is ≈ 1.87 for $\nu = 5$ and ≈ 1.33 for $\nu = 11$. The large scaling factor in this system poses a problem for the detection of signatures of the limit cycle.

5.5.2 SRG with induced Three-body Potential

In this section we discuss the SRG evolution of the separable potential with included induced three-body potentials up to a certain angular momentum l_{max}. The total angular momentum $L = 0$ is conserved during the flow. As opposed to the previous section the evolution in the three-body system is now in principle unitary. Only the truncation in l is a violation to it. So all three-body observables should stay constant within a certain range. Otherwise, higher partial waves should be included. As a benchmark we examined the deviation of the three-body binding energies.

In principle we expect the extraction of a limit cycle signature in the three-body system to be less complicated. In the presented RG method for the two-body system the log-periodic function is contained in the counterterm. If no counterterm is originally present, it has to be included when the cutoff is lowered. By analogy, in the two-body system the SRG evolution of the initial potential and the counterterm, which exhibits the limit cycle, can not be separated. The log-periodic signal has to be extracted from the evolved two-body potential. A different situation is present in the three-body system. As in the previous section, we employ the separable two-body potential with no initial three-body potential. During the evolution a three-body potential is induced, which in analogy plays the role of the counterterm and should thus contain the limit cycle. Recall that in the RG treatment the limit cycle is manifested in the three-body potential. This can also be regarded from a different angle. The evolution of the separable potential in the two-body space is independent of the evolution of higher-body interactions. Since there is no limit cycle present for the separable potential in the two-body system, the limit cycle should thus appear in the induced three-body potential. This is also the reason why no initial three-body potential is included. We wanted to avoid that the evolved initial three-body potential overlays signatures of the limit cycle, which we expect to be present in the induced three-body potentials.

[2] A universal scaling curve in nuclear physics is e.g. the Phillips line [36].

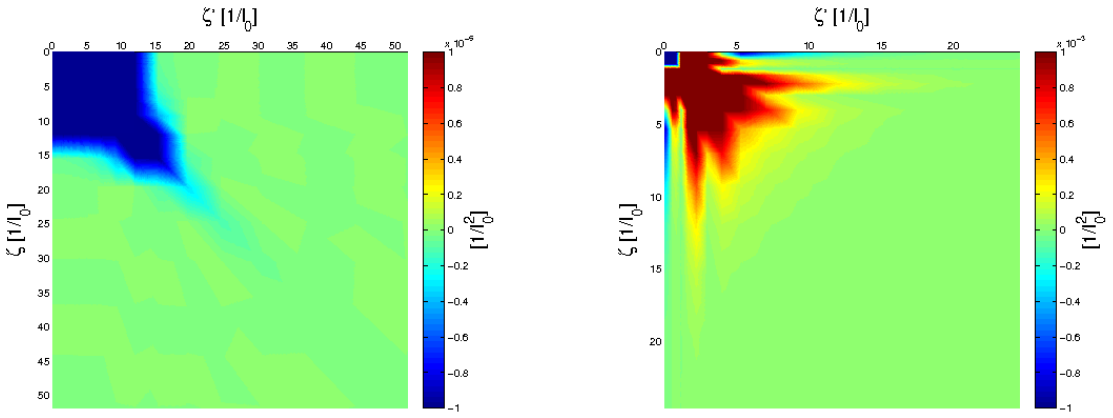

Figure 5.5.: Induced three-body potential with the hyperangle $\omega = \pi/2$. The incoming and outgoing angular momenta are $l = l' = 0$. The initial two-body separable potential is in the unitary limit with the cutoff $\Lambda = 20\, l_0^{-1}$. Left: Evolved with the T generator to $s = 10^{-4}\, l_0^4$ ($\lambda = 10\, l_0^{-1}$). Right: Evolved with the exponential generator with modified two-body evolution to $s = 0.5\, l_0^4$ ($\lambda \approx 1.19\, l_0^{-1}$) and $\sigma = 2\, l_0^{-1}$. In both cases the maximal deviation of the bound state energies from the initial values is within a few percent.

We applied the T generator, the subtracted exponential generator and the exponential generator with modified two-body evolution. No simple way is known to us to construct a subtracted inverse generator similar to the subtracted exponential generator in order to avoid the disconnected terms. Additionally, we found for the other systems that the inverse and exponential generators behave similar. Therefore, we focused on the exponential generators.

We applied an analysis similar to the presented analysis in chapter 4.3. But we could not find a signal, neither for the exponential generators nor for the T generator. A possible explanation is that we can not evolve the potential far enough.

For comparison to the $1/R^2$ plots, two induced three-body potentials are presented in Fig. 5.5, where the T as well as a exponential generator is applied. For the presentation we used the definition of the hypermomentum $\zeta = \sqrt{p^2 + \frac{3}{4}q^2}$ and the hyperangle $\omega = \arctan(\frac{\sqrt{3}p}{2q})$ as independent variables. We could not detect the structures we found for the evolved $1/R^2$ potential, whereas the graph for the exponential generator resembles rather the structures of the $1/R^2$ potential than the T generator. Note that the induced potential strongly depends on the angular momentum variables.

The two main obstacles for extending the range of the evolution are the computational runtime and the numerical errors. In contrast to the two-body system there are two incoming momenta p and q. In place of calculations including $N \times N$ matrices, where N is the number of grid points, the matrices enlarge to $N^2 \times N^2$ and the computation time of them scales with N^6. Hence, one step in the computation of the ODE (ordinary differential equation) solver takes considerably more time than in the two-body system.

Partly correlated to this is the alteration of the binding energy. The deviation of the binding energies during the evolution is substantially larger than in the two-body system. The deviations become so large that we aborted the evolution. This is mainly due to three reason, which are partly interconnected: 1. The number of grid points lies only in the order around $N = 30$ because of the scaling behavior of the runtime. 2. Splines have to be used because of the three different two-body subsystems in Jacobi coordinates. 3. The truncation in the angular momentum l. Apparently these reasons affect each other. A lower number of grid points leads to higher errors when splines are used. Including higher angular momenta leads to increased computation time.

In general, we evolve up the point where the deviation of a bound state energy from the initial value reaches the magnitude of $\sim 1\%$. Note that the deviation of the energies can differ by orders of magnitude. This can lead to a situation where the deviation of the ground state energy is very small but the deviation for the next state exceeds the one percent threshold.

The programs typically run a few days until the point where the evolution has to be aborted due to the error of the binding energy. This is already a long runtime. However, if the errors would stay in an acceptable range, one could try to evolve to larger values of s and choose a few parameter sets to run for a long time. Therefore, we spent much effort in trying to decrease the error. For example we applied several approaches to choose the sampling points of the momenta. However, the attempts did not lead to a significant improvement.

At the end we briefly expound some aspects of the generators. Using the exponential generators we can evolve to larger values of s compared to the use of the T generator. This behavior was expected and thus they are still the best candidate for detecting limit cycles. However, we prefer the exponential generator with modified two-body evolution.

Using the subtracted exponential generator results in a larger runtime compared to the other exponential generator. This is due to the fact that the subtracted generator implies more terms, which have to be computed. In addition, the subtracted generator has no benefits concerning the error of the binding energy. Since one objective is to reduce the runtime, we mainly focused on the exponential generator with modified two-body evolution.

Part II.
Limit Cycles at Finite Density

6 Theoretical Framework

At the beginning of the second part of this thesis we want to mention that the pole structure of the two- and three-body scattering amplitude in the medium was already examined for *equal masses* in my diploma thesis [37]. In this thesis we consider the case of *unequal masses*. In the following chapters we will explicitly state what was examined in my diploma thesis.

6.1 Ultracold Fermi Gases

Ultracold Fermi gases display a rich spectrum of different phenomena and are therefore intensively studied experimentally and theoretically. Commonly known are the emergence of Bose-Einstein condensation (BEC) and superfluidity, which can be described by the BCS theory for weak couplings. Depending on the scattering length the Fermi gas can be located in the BEC or BCS regime. The transition between these two states is called BEC-BCS crossover and is also subject of numerous studies. Focusing on the BCS region a rich phase structure can be explored. The BCS theory relates the appearance of superfluidity to the formation of Cooper pairs, which consist of two fermions with opposite momenta and spins. Due to the Pauli blocking, Cooper pairs can be formed for arbitrarily weak interactions. The order parameter Δ determines the gap of the single-particle excitation spectrum. Besides the BCS phase there exist different hypothetical superfluid phases like FFLO phases [38]. Considering systems with mass or spin imbalance the Fermi surfaces are in general mismatched. This can result in a preferred formation of Cooper pairs with a nonzero total momentum. Due to these pairs with finite momentum the order parameter in FFLO phases possesses a spatially periodic structure [38]. A different line of research is concerned with the phase structure of three-component Fermi gases. Theoretical results predict that generally one fermion species remains unpaired while the other two fermion species form pairs [39–42].

A summary of all research topics related to superfluid phases in ultracold Fermi gases is definitely beyond the scope of this thesis. We therefore mentioned only those topics which are most relevant to our approach. An interesting question is how the phase structure is altered when three-body physics becomes relevant. One part of this thesis is dedicated to this question. Here, we worked together with Prof. Dr. Jens Braun and Dietrich Roscher. They explore the phase structure of mass and spin imbalanced Fermi gases. In [43] their results for a one dimensional system are presented. They found that the bound state properties obtained by a two-body calculation qualitatively predict traits of the many-body phase diagrams similar to the BCS theory. We make the assumption that the same holds for the three-body calculation. To be more precise, we assume that our in-medium three-body calculation qualitatively predicts some properties of the phase diagram in the case where three-body physics like three-body bound states plays a role. We will go into more detail in the following chapters.

6.2 Effective Field Theory

For the computation of the pole structure of the two- and three-body system we use an effective field theory framework, which is presented in detail in [1]. As the name suggests, in this framework an effective interaction is considered instead of a realistic interaction. This method is applicable in the low energy domain, where the short range interaction can not be resolved. There the effective interaction correctly describes the low energy physics up to some error scale. This can be elucidated using the example of neutral atoms. If the relative momentum of two atoms is so small that the associated de Broglie wavelength is much larger than the spatial extent of the atoms, the structure of the electron cloud can not be resolved. In this case the atoms behave like point-like particles with short range interactions. The interaction can be described using delta potentials and derivatives of the delta potential. Hence, systems which display totally distinct behavior at short distances can be described by the same effective field theory as long as low-energy observables are considered. That is a huge advantage of this method. Thus, results can be applied to different systems like atoms and nucleons. This feature is particularly useful when universal aspects are examined.

However, the applied coupling constants are unphysical. To obtain quantitative results the coupling constants have to be matched to some low-energy observables. Afterwards other observables can be predicted.

It is crucial to be aware of the scale which sets the limit for the application of this approach. For neutral atoms the long range part of the inter-atomic potential is given by the van der Waals potential. According to this the limiting scale is given by the van der Waals length in this case. The van der Waals length is the spacing where the kinetic energy and the potential energy of the van der Waals potential have the same magnitude.

6.3 Feynman Rules

In this thesis we build on the effective field theory and the corresponding Lagrangian described in [1]. In [44] the Lagrangian with different masses in the vacuum is discussed. We consider the interaction of three distinguishable fermions, which can have different masses. The employed Lagrangian is thus given by

$$\mathscr{L} = \sum_{i=0}^{2} \Psi_i^\dagger \left(i\partial_t + \frac{\vec{\nabla}^2}{2m_i} \right) \Psi_i - \sum_{i<j=0}^{2} \frac{g_{ij}}{2} \Psi_i^\dagger \Psi_j^\dagger \Psi_i \Psi_j + h\, \Psi_0^\dagger \Psi_1^\dagger \Psi_2^\dagger \Psi_0 \Psi_1 \Psi_2 \,, \tag{6.1}$$

with the fermion fields Ψ_i and $i \in \{0,1,2\}$. Note that throughout this thesis we set $\hbar = 1$. As one can easily see we consider non-relativistic systems. The interactions are given by two- and three-body contact interactions. The three-body contact interaction determines the three-body spectrum. However, the dependence on this three-body interaction can be traded for a cutoff dependence. We will explain this in detail in chapter 8.2. We therefore leave out the three-body contact interaction. The Lagrangian then reduces to

$$\mathscr{L} = \sum_{i=0}^{2} \Psi_i^\dagger \left(i\partial_t + \frac{\vec{\nabla}^2}{2m_i} \right) \Psi_i - \sum_{i<j=0}^{2} \frac{g_{ij}}{2} \Psi_i^\dagger \Psi_j^\dagger \Psi_i \Psi_j \,. \tag{6.2}$$

Next we introduce auxiliary dimer fields d_k and $d_k^\dagger$. In principle the dimer fields destroy or create, respectively, two particles i and j at the same place. The Lagrangian can thus be rewritten as

$$\mathscr{L} = \sum_{i=0}^{2} \Psi_i^\dagger \left(i\partial_t + \frac{\vec{\nabla}^2}{2m_i} \right) \Psi_i + \sum_{k=0}^{2} \left(\Delta_k d_k^\dagger d_k - \frac{g_k}{2} \left(d_k^\dagger \Psi_i \Psi_j + \Psi_i^\dagger \Psi_j^\dagger d_k \right) \right) \,. \tag{6.3}$$

Here we denote the coupling constant g_{ij} by g_k with $k \in \{0,1,2\}$ and $k \neq i \neq j$. In other words the index k denotes the particle which does not participate in the interaction. The equivalence of the Lagrangians in Eq. (6.3) and Eq. (6.2) can be easily shown using the classical equations of motion. The sole condition is

$$\Delta_k = \frac{g_k}{2} \,. \tag{6.4}$$

The Feynman rules can readily be deduced from the Lagrangian Eq. (6.3). In this thesis we calculate physical quantities in the medium as well as in the vacuum. We will therefore state the vacuum and in-medium rules. The general derivation of Feynman rules can be found in [45] for the vacuum and in [46, 47] for the medium. We consider processes at zero temperature. Hence, all states inside the Fermi sea are filled up to the Fermi momentum k_F.

The coupling constants are independent of the medium. So the vertex factors are given by $-ig_k/2$, see Fig. 6.1. Since we consider three different cases, we have three different single-particle propagators in Fig. 6.2. The first one is the usual non-relativistic propagator in the vacuum. Since we introduced the dimer fields, we also obtain a bare dimer propagator. This dimer propagator provides no momentum dependence and basically corresponds to a coupling constant. Therefore, this propagator remains the same in the vacuum and in the medium. Left to consider are the two single-particle propagators in the medium. In general, we consider two cases regarding the Fermi sphere in this thesis. In the first case we consider a rigid Fermi sphere, which implies that no particle can enter the sphere and hence no holes can be formed. This case relates to c) in Fig. 6.2. Additionally, we also include hole propagation. This relates to the common in-medium propagator in d), which includes particle and hole propagation. We do not distinguish the propagators symbolically. From the context it will be evident which case we consider and hence which propagator has to be used.

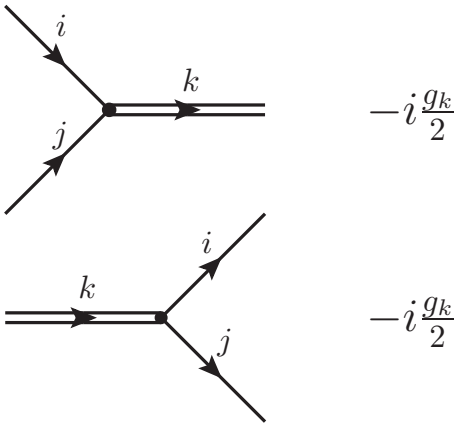

Figure 6.1.: Vertex factors with the convention $k \neq i \neq j$.

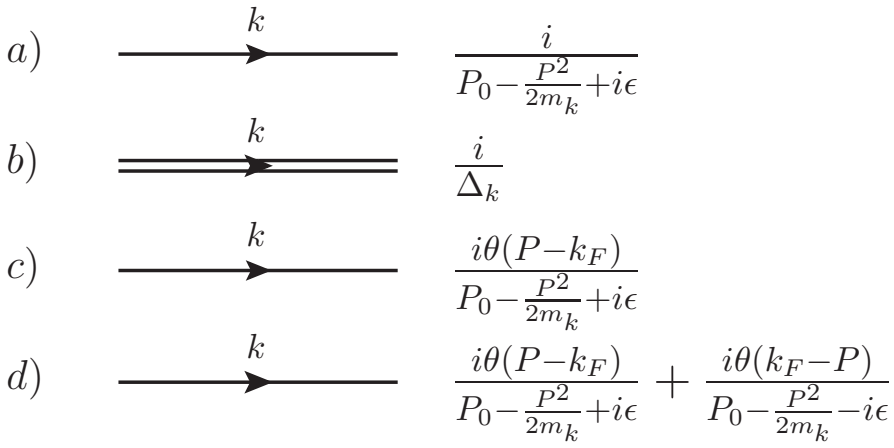

Figure 6.2.: Propagators used in this thesis: a) is the usual non-relativistic single-particle vacuum propagator, b) is the bare dimer propagator (in the vacuum as well as in the medium), c) is the in-medium single-particle propagator without hole propagation and d) is the common in-medium single-particle propagator with included particle and hole propagation.

7 Dimer Propagator

After introducing the applied theoretical framework, we calculate the full dimer propagator in this chapter. The full dimer propagator is needed for the calculation of the three-body scattering amplitude. Additionally, the two-body physics of the system is encoded in the full dimer propagator. We therefore discuss the pole structure of the in-medium dimer propagator and examine the effect of the included hole propagation.

The derivation of the full dimer propagator as well as the three-body scattering amplitude can e.g. also be found in [1] for identical bosons and in [44] for particles with unequal masses in the vacuum. The incorporation of the medium, however, implies significant changes. The derivation for equal masses in the medium can be found in my diploma thesis [37]. The derivation of the dimer propagator and the three-body scattering amplitude in the medium for unequal masses is very similar to the derivation in the case of equal masses in the medium. However, the calculation of the finite density loop integrals becomes far more complex.

7.1 Derivation of the Dimer Propagator

The bare dimer propagator does not possess a momentum dependency. We therefore introduce the full dimer propagator which is the solution of the diagrammatic equation in Fig. 7.1. Before we proceed with the calculation of the full dimer propagator, we discuss the assumptions on the considered system.

This thesis mainly deals with the following scenario. Two respectively three distinguishable fermions interact with each other in presence of a Fermi sea at zero temperature. This means there is a Fermi sea for each particle species and all states up the Fermi momentum are occupied. Due to the complicated boundary conditions of the dimer propagator, we consider the Fermi momentum to be the same for all fermions. The fermions can in general have different masses. Hence, we can consider e.g. different atoms with different masses or particles in different states likes hyperfine states, or a mixture of both. The only restriction is that the fermions have to be distinguishable. Consequently, they have to differ in at least one quantum number. Note that the Fermi momenta are equal in contrast to the Fermi energies in the case of unequal masses.

Additionally, we consider the two respectively three particles to exclusively interact among each other such that no interaction between the Fermi sphere and the selected particles is included. According to this we assume a rigid Fermi sphere where no holes are present. As an improvement to this approach, it was suggested to include hole propagation in the calculation of the dimer propagator. We will also consider this in-medium case and discuss the results in section 7.2.2. In advance, we just want to state that the inclusion of hole propagation does not fulfill the expectations. This is a reason why we focus on the original approach. If the hole propagation is included, we will explicitly states this. Unless specified otherwise, the term "in-medium" refers to the main scenario with rigid Fermi seas without holes.

In this context note that the Feynman diagrams depicted in Fig. 7.1 are not the only ones in the two-body system. If holes are included, new classes of diagrams appear that actually have to be included and summed up. However, we consider only the hole propagation in the Feynman diagrams in Fig. 7.1. In contrast, in our main scenario without hole propagation the depicted Feynman diagrams are the only ones present.

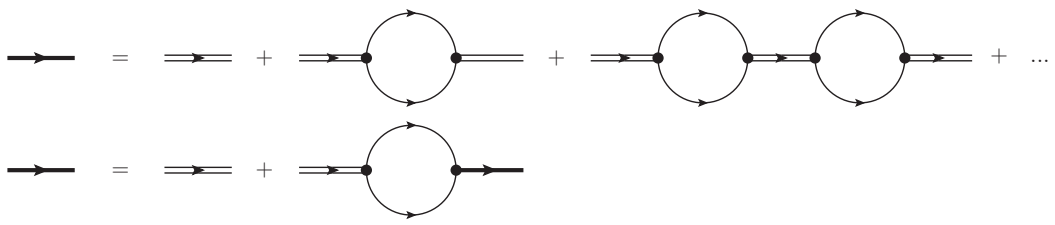

Figure 7.1.: The two equivalent Feynman graphs represent the diagrammatic equation for the full dimer propagator, which is symbolized by a thick line. Figure taken from my diploma thesis [37].

We proceed with the calculation of the full dimer propagator. In the following we will frequently omit the word "full" and just call it "dimer propagator". Using the Feynman rules, the full in-medium dimer propagator can be written as

$$\begin{aligned} iD_k(P_0,\mathbf{P}) &= \frac{i}{\Delta_k} + \frac{i}{\Delta_k}\left(\frac{-ig_k}{2}\right) iI_k(P_0,\mathbf{P}) \left(\frac{-ig_k}{2}\right) iD_k(P_0,\mathbf{P}) \\ \Leftrightarrow iD_k(P_0,\mathbf{P}) &\left(1 - \frac{g_k^2}{4\Delta_k} I_k(P_0,\mathbf{P})\right) = \frac{i}{\Delta_k} \\ \Leftrightarrow iD_k(P_0,\mathbf{P}) &= \frac{i}{\Delta_k\left(1 - \frac{g_k^2}{4\Delta_k} I_k(P_0,\mathbf{P})\right)}, \end{aligned} \tag{7.1}$$

with the definition of the loop integral

$$iI_k(P_0,\mathbf{P}) = \int_{|\mathbf{q}|<\Lambda} \frac{d^4q}{(2\pi)^4} \left(\frac{i\Theta(|\frac{m_i}{M_k}\mathbf{P}+\mathbf{q}|-k_F)}{\frac{m_i}{M_k}P_0 + q_0 - \frac{1}{2m_i}(\frac{m_i}{M_k}\mathbf{P}+\mathbf{q})^2 + i\epsilon} \frac{i\Theta(|\frac{m_j}{M_k}\mathbf{P}-\mathbf{q}|-k_F)}{\frac{m_j}{M_k}P_0 - q_0 - \frac{1}{2m_j}(\frac{m_j}{M_k}\mathbf{P}-\mathbf{q})^2 + i\epsilon} \right). \tag{7.2}$$

Note that Eq. (7.1) applies for all considered cases. Only the loop Integral $I_k(P_0,P)$ has to be adjusted.

We denote the total mass of the two particles by $M_k = m_i + m_j$ and the reduced mass by $\frac{1}{\mu_k} = \frac{1}{m_i} + \frac{1}{m_j}$ with the convention $k \neq i \neq j$. Equally, the index k of the dimer propagator $D_k(P_0,\mathbf{P})$ indicates the particle which is not included in the dimer propagator. Since we consider two- and three-body interactions, this notation is unique.

We choose the momenta of the propagators in the loop to be $\frac{m_i}{M_k}\mathbf{P}+\mathbf{q}$ as well as $\frac{m_j}{M_k}\mathbf{P}-\mathbf{q}$. This choice leads to a separation of the total kinetic energy into the kinetic energy of the center of mass and the reduced system in the denominator after the contour integration. The Fermi sea restricts the phase space of the loop integral, which is encoded in the theta functions. The calculation of the loop integral is very lengthy and complex. The detailed derivation can therefore be found in appendix C. The result will be given later in this section. Before, we address the renormalization of the dimer propagator.

The loop integrals in the medium as well as in the vacuum are divergent for large momenta. The cutoff Λ is therefore introduced. The cutoff is, however, an artificial, arbitrary parameter. To make physical predictions we have to get rid of the cutoff dependence. Hence, the dimer propagator has to be renormalized. To this end, we match the dimer propagator to the two-body scattering length. This procedure leads to a relation between the scattering length and the cutoff Λ. Subsequently, we can eliminate the dependence of the dimer propagator on the unphysical parameter Λ.

Note that the Fermi sea primarily affects the low momentum region[1]. The region of high momenta (ultraviolet region) stays unaffected. Therefore, the vacuum and the in-medium dimer possess the same cutoff dependence and can be renormalized in the same way.

We proceed in the following way. First, we renormalize the full dimer propagator in the vacuum and then apply the results for the renormalization of the in-medium propagator. For that purpose the dimer propagator in the vacuum has to be calculated. This computation can be outlined in a few lines, in contrast to the in-medium case. The loop integral in the medium and in the vacuum differ only by the theta functions. Hence, the theta functions in Eq. (7.2) have to be omitted in order to obtain the loop integral in the vacuum

$$\begin{aligned} iI_k(P_0,\mathbf{P})_{vac} &= \int_{|\mathbf{q}|<\Lambda} \frac{d^4q}{(2\pi)^4} \frac{i}{\frac{m_i}{M_k}P_0 + q_0 - \frac{1}{2m_i}(\frac{m_i}{M_k}\mathbf{P}+\mathbf{q})^2 + i\epsilon} \frac{i}{\frac{m_j}{M_k}P_0 - q_0 - \frac{1}{2m_j}(\frac{m_j}{M_k}\mathbf{P}-\mathbf{q})^2 + i\epsilon} \\ &= i\int_{|\mathbf{q}|<\Lambda} \frac{d^3q}{(2\pi)^3} \frac{1}{P_0 - \frac{P^2}{2M_k} - \frac{q^2}{2\mu_k} + i\epsilon} \\ &= \frac{i\mu_k}{\pi^2}\int_0^\Lambda dq\, \frac{q^2}{b_k - q^2} \\ &= \frac{i\mu_k}{\pi^2}\left[-q - \frac{\sqrt{b_k}}{2}\left(\ln\left(q-\sqrt{b_k}\right) - \ln\left(q+\sqrt{b_k}\right)\right)\right]_0^\Lambda \\ &= \frac{i\mu_k}{\pi^2}\left[-\Lambda - \frac{\sqrt{b_k}}{2}\left(\ln\left(\Lambda-\sqrt{b_k}\right) - \ln\left(\Lambda+\sqrt{b_k}\right)\right) + \frac{\sqrt{b_k}}{2}\left(\ln\left(-\sqrt{b_k}\right) - \ln\left(\sqrt{b_k}\right)\right)\right] \\ &= \frac{i\mu_k}{\pi^2}\left[-\Lambda + \frac{\pi}{2}\sqrt{-b_k}\right], \end{aligned} \tag{7.3}$$

[1] which of course depends on the Fermi momentum k_F.

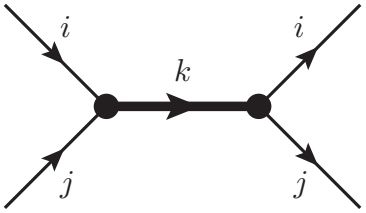

Figure 7.2.: A two-body scattering process in the vacuum. The full dimer propagator (thick solid line) can be used to express the scattering process. Figure taken from my diploma thesis [37]

with $b_k = 2\mu_k(P_0 - \frac{P^2}{2M_k} + i\epsilon)$. We made use of the fact that $\Lambda \gg b_k$. In addition, the partial fraction decomposition $\frac{q^2}{b-q^2} = -1 - \frac{\sqrt{b}}{2}\left(\frac{1}{q-\sqrt{b}} - \frac{1}{q+\sqrt{b}}\right)$ was utilized. Since b_k has a positive imaginary part, $i\sqrt{b_k} = -\sqrt{-b_k}$ holds as well. Note that the function $I_k(P_0,P)_{vac}$ does only depend on the absolute value of the momentum. This also holds true for the in-medium integrals.

We have calculated the vacuum dimer propagator and can now continue with the matching to a physical observable. We match the scattering length to the scattering amplitude $\mathscr{A}_k^{CMS}$ in the vacuum in the center of mass (CMS) frame in the limit of zero momentum. The exact matching condition we use is given by

$$a_k = -\frac{\mu_k}{2\pi}\mathscr{A}_k^{CMS}(\mathbf{p}\to 0)\,, \tag{7.4}$$

with the incoming momenta $\mathbf{p}$ and $-\mathbf{p}$. The two-body scattering amplitude can easily be obtained from the dimer propagator. This is depicted in Fig. 7.2. The dimer propagator encodes all information about the scattering process. Consequently, the two external coupling constants have to be multiplied to express arbitrary scattering processes. The two-body scattering amplitude in the vacuum center of mass frame can thus be written as

$$\begin{aligned} i\mathscr{A}_k^{CMS}(p) &= \left(-i\frac{g_k}{2}\right) iD_k(\tfrac{p^2}{2\mu_k},0)_{vac}\left(-i\frac{g_k}{2}\right) \\ &= -i\frac{g_k^2}{4\Delta_k}\left[1 - \frac{g_k^2}{4\Delta_k}\frac{\mu_k}{\pi^2}\left(-\Lambda + \frac{\pi}{2}\sqrt{-2\mu_k(\tfrac{p^2}{2\mu_k}+i\epsilon)}\right)\right]^{-1}. \end{aligned} \tag{7.5}$$

We plug Eq. (7.5) into Eq. (7.4). This yields

$$\begin{aligned} a_k &= \frac{\mu_k g_k^2}{8\pi\Delta_k}\left[1 + \frac{g_k^2\mu_k\Lambda}{4\Delta_k\pi^2}\right]^{-1} \\ \Leftrightarrow 1 + \frac{g_k^2\mu_k\Lambda}{4\Delta_k\pi^2} &= \frac{\mu_k g_k^2}{8\pi\Delta_k a_k}\,. \end{aligned} \tag{7.6}$$

Finally, we obtained the relation between the scattering length and the cutoff Λ. We continue by inserting Eq. (7.6) and Eq. (7.3) into Eq (7.1)

$$\begin{aligned} iD_k(P_0,P)_{vac} &= \frac{i}{\Delta_k}\left[1 + \frac{g_k^2\mu_k\Lambda}{4\pi^2\Delta_k} - \frac{g_k^2\mu_k}{8\pi\Delta_k}\sqrt{-b_k}\right]^{-1} \\ &= \frac{i}{\Delta_k}\left[\frac{g_k^2\mu_k}{8\pi\Delta_k a_k} - \frac{g_k^2\mu_k}{8\pi\Delta_k}\sqrt{-b_k}\right]^{-1} \\ &= \frac{8\pi i}{g_k^2\mu_k}\left[\frac{1}{a_k} - \sqrt{-b_k}\right]^{-1} = \frac{8\pi i}{g_k^2\mu_k}\left[\frac{1}{a_k} - \sqrt{-2\mu_k(P_0 - \tfrac{P^2}{2M_k} + i\epsilon)}\right]^{-1}. \end{aligned} \tag{7.7}$$

This is the final renormalized formula of the vacuum dimer propagator. One can easily recognize that the cutoff dependence has been replaced by a dependence on the scattering length.

We continue with the renormalization of the in-medium dimer propagator

$$iD_k(P_0,P) = \frac{i}{\Delta_k\left(1 - \frac{g_k^2}{4\Delta_k}I_k(P_0,P)\right)} = \frac{i}{\Delta_k\left(1 + \frac{g_k^2\mu_k\Lambda}{\Delta_k 4\pi^2} - \frac{g_k^2\mu_k}{8\Delta_k\pi^2}L_k(P_0,P)\right)}\,. \tag{7.8}$$

Here we have separated the cutoff dependence in the loop integral $I_k(P_0,P) = \frac{2\mu_k}{(2\pi)^2}(-2\Lambda + L_k(P_0,P))$. As already mentioned, the cutoff dependence is equal for the vacuum and in-medium propagator. We can now make use of the relation between the cutoff and the scattering length in Eq. (7.6). It yields

$$iD_k(P_0,P) = \frac{i8\pi}{g_k^2\mu_k}\left[\frac{1}{a_k} - \frac{1}{\pi}L_k(P_0,P)\right]^{-1} . \tag{7.9}$$

This is the final form of the in-medium dimer propagator. The function $L_k(P_0,P)$ is calculated in appendix C. The results for included hole propagation can also be found there. Note that in this case, only the function $L_k(P_0,P)$ has to be replaced by $L_k^V(P_0,P)$, which is defined in appendix C.
We explicitly state here the function $L_k(P_0,P)$. Two different results are obtained depending on the total momentum P. For real energies P_0 we get
$P \in [0, 2k_F]$:

$$\begin{aligned} L_k(P_0,P) =& + \tfrac{1}{2}P + k_F + \left(\frac{b_k - k_F^2}{4P}\frac{M_k}{\mu_k} + \tfrac{1}{4}P\right)\left(\ln\left(q_G - \sqrt{b_k}\right) + \ln\left(q_G + \sqrt{b_k}\right)\right) \\ &+ \frac{\sqrt{b_k}}{2}\left(\ln\left(\tfrac{m_i}{M_k}P + k_F - \sqrt{b_k}\right) - \ln\left(\tfrac{m_i}{M_k}P + k_F + \sqrt{b_k}\right) + \ln\left(\tfrac{m_j}{M_k}P + k_F - \sqrt{b_k}\right) - \ln\left(\tfrac{m_j}{M_k}P + k_F + \sqrt{b_k}\right)\right) \\ &- h_i\left(\ln\left(\tfrac{m_i}{M_k}P + k_F - \sqrt{b_k}\right) + \ln\left(\tfrac{m_i}{M_k}P + k_F + \sqrt{b_k}\right)\right) \\ &- h_j\left(\ln\left(\tfrac{m_j}{M_k}P + k_F - \sqrt{b_k}\right) + \ln\left(\tfrac{m_j}{M_k}P + k_F + \sqrt{b_k}\right)\right) \end{aligned} \tag{7.10}$$

$P \geq 2k_F$:

$$\begin{aligned} L_k(P_0,P) =& 2k_F + \pi\sqrt{-b_k} \\ &+ h_i\left(\ln\left(\tfrac{m_i}{M_k}P - k_F - \sqrt{b_k}\right) + \ln\left(\tfrac{m_i}{M_k}P - k_F + \sqrt{b_k}\right) - \ln\left(\tfrac{m_i}{M_k}P + k_F - \sqrt{b_k}\right) - \ln\left(\tfrac{m_i}{M_k}P + k_F + \sqrt{b_k}\right)\right) \\ &+ h_j\left(\ln\left(\tfrac{m_j}{M_k}P - k_F - \sqrt{b_k}\right) + \ln\left(\tfrac{m_j}{M_k}P - k_F + \sqrt{b_k}\right) - \ln\left(\tfrac{m_j}{M_k}P + k_F - \sqrt{b_k}\right) - \ln\left(\tfrac{m_j}{M_k}P + k_F + \sqrt{b_k}\right)\right) \\ &+ \frac{\sqrt{b_k}}{2}\left(\ln\left(\tfrac{m_i}{M_k}P + k_F - \sqrt{b_k}\right) - \ln\left(\tfrac{m_i}{M_k}P + k_F + \sqrt{b_k}\right) + \ln\left(\tfrac{m_i}{M_k}P - k_F + \sqrt{b_k}\right) - \ln\left(\tfrac{m_i}{M_k}P - k_F - \sqrt{b_k}\right)\right) \\ &+ \frac{\sqrt{b_k}}{2}\left(\ln\left(\tfrac{m_j}{M_k}P + k_F - \sqrt{b_k}\right) - \ln\left(\tfrac{m_j}{M_k}P + k_F + \sqrt{b_k}\right) + \ln\left(\tfrac{m_j}{M_k}P - k_F + \sqrt{b_k}\right) - \ln\left(\tfrac{m_j}{M_k}P - k_F - \sqrt{b_k}\right)\right) \end{aligned} \tag{7.11}$$

with

$$b_k = 2\mu_k(P_0 - \tfrac{P^2}{2M_k} + i\epsilon), \quad q_G = \sqrt{k_F^2 - \tfrac{m_i m_j}{M_k^2}P^2} \quad \text{and } h_i = \frac{b_k - k_F^2 + \frac{m_i^2}{M_k^2}P^2}{4\frac{m_i}{M_k}P} .$$

In this thesis we use the principal value of the complex logarithm, and the complex square root is defined as $\sqrt{z} = \sqrt{|z|}\exp(i\arg(z)/2)$ so that $\sqrt{z}$ lies in $\{\rho\, e^{i\phi} | \rho \in]0,\infty], \phi \in]-\pi/2, \pi/2]\}$.

We also state the result for the special case of zero total momentum $P = 0$. In this instance the boundary conditions become very simple. It yields

$$L_k(P_0, P=0) = 2k_F + \sqrt{b_k}\left(\ln(k_F - \sqrt{b_k}) - \ln(k_F + \sqrt{b_k})\right) . \tag{7.12}$$

In the three-body scattering amplitude a wave function renormalization is applied. We therefore have to compute the residue of the dimer propagator. However, the pole of the in-medium propagator can not be calculated analytically. Hence, we calculate the residue of the vacuum propagator. We refer to chapter 8.1, where we discuss to what extent this is justified.

If the scattering length a_k is positive, the vacuum dimer propagator has a pole. It is located at $P_0 = \frac{P^2}{2M_k} - \frac{1}{2\mu_k a_k^2} - i\epsilon$ for $a_k > 0$. If the scattering length is negative $a_k < 0$, there is no pole on the physical sheet of the root. On the unphysical sheet there is, however, a pole which corresponds to a virtual state. For the computation of the residue we use the formula in [48]

$$Res\left[\frac{\phi(z)}{\psi(z)}\right]_{z=z_0} = \frac{\phi(z_0)}{\psi'(z_0)} , \tag{7.13}$$

where ψ' is the derivative of ψ with respect to z. We make the choice

$$\phi(P_0) = \frac{8\pi}{g_k^2 \mu_k} \quad \text{and} \quad \psi(P_0) = \frac{1}{a_k} - \sqrt{-2\mu_k(P_0 - \frac{p^2}{2M_k} + i\epsilon)}\,. \tag{7.14}$$

The derivative is then given by

$$\psi'(P_0) = \frac{\mu_k}{\sqrt{-2\mu_k(P_0 - \frac{p^2}{2M_k} + i\epsilon)}}\,, \tag{7.15}$$

and we finally get the residue

$$Res(D_k(P_0, P)_{vac}) = \frac{8\pi}{g_k^2 \mu_k^2 a_k} := Z_k\,, \tag{7.16}$$

which we denote by Z_k.

7.2 Results

In this section the pole structure of the in-medium propagators is discussed. We begin with briefly relating the pole structure to the known two-body physics, which is necessary for the understanding of the three-body sector. For equal masses a more extensive discussion can be found in [37, 49]. Subsequently, we discuss the effect of unequal masses. Special attention is paid to the effect of including hole propagation.

7.2.1 Results without Hole Propagation

In this section the poles of the standard in-medium propagator (hole propagation not included) are examined. We begin with the equation for zero total momentum

$$\frac{1}{a_k} = \frac{1}{\pi}\left\{2k_F + \sqrt{\sigma_k}\left(\ln\left(k_F - \sqrt{\sigma_k}\right) - \ln\left(k_F + \sqrt{\sigma_k}\right)\right)\right\}\,, \tag{7.17}$$

with $\sigma_k = 2\mu_k(P_0 + i\epsilon)$. Note that the equation depends on the reduced mass μ_k, but not on the total mass M_k. Consequently, the poles for zero total momentum do not depend on the mass ratio m_i/m_j. This is due to the fact that the total mass can be expressed by the reduced mass and the mass ratio. In addition, the poles scale with $k_F^2/(2\mu_k)$. We will therefore normalize the momentum and the scattering length with the Fermi momentum and the Energy to $k_F^2/(2\mu_k)$ in order to obtain more general results. In some instances where we compare the results to the vacuum case this normalization is not applicable. In this case there is a free length scale l_0 and we express the variables in units of l_0.

Beforehand, we want to state that Eq. (7.17) for zero total momentum is the expected generalization of the equation with equal masses from my diploma thesis [37]. Hence, the same physics is obtained in this case. We will nevertheless discuss the poles for zero momentum since it is important for the understanding of the framework. For finite momenta, however, the poles depend on the mass ratio and therefore different results can be expected. In general, the dependence of the dimer poles on the Fermi momentum, scattering length and total momentum was examined for equal masses in my diploma thesis. Hole propagation was, however, not included and our results were not compared to [50].

In Fig. 7.3 the pole energies for $P = 0$ are depicted as a function of the normalized inverse scattering length. As announced, we make use of the scaling and normalize the energy E of the poles as $E_2^* = \frac{2\mu_k}{k_F^2}E$. We recap that in the vacuum we obtain poles, with energies $P_0 = \frac{p^2}{2M_k} - \frac{1}{2\mu_k a_k^2}$, only for positive scattering lengths. In contrast to the vacuum case, poles at negative scattering lengths appear, which possess a positive energy. The in-medium poles asymptotically approach the value $E_2^* = 1$ in the limit $1/a_k \to -\infty$. In unnormalized units the value 1 corresponds to $k_F^2/(2\mu_k)$. This limit can also be deduced from Eq. (7.17). In the limit $1/a_k \to -\infty$ the term $1/a_k$ can only be compensated by the term $\ln(k_F - \sqrt{\sigma_k})$, where the argument of the logarithm approaches zero. Therefore, P_0 has to approach $k_F^2/(2\mu_k)$. Note that this is the maximal kinetic energy of two particles inside the Fermi sea, which we denote by E_2^{th}. In my diploma thesis for equal masses these positive energy poles could be related to Cooper pairs. This was, amongst others, accomplished by a comparison with the textbook [46].

Forming Cooper pairs generates an energy gain. The energy gain ΔE in this framework is given by the difference between the energy of the pole and the maximal kinetic energy inside the Fermi sphere $\Delta E = k_F^2/(2\mu_k) - E$, where E is the energy of the pole. Accordingly, the energy gain decreases continuously in the limit $1/a_k \to -\infty$.

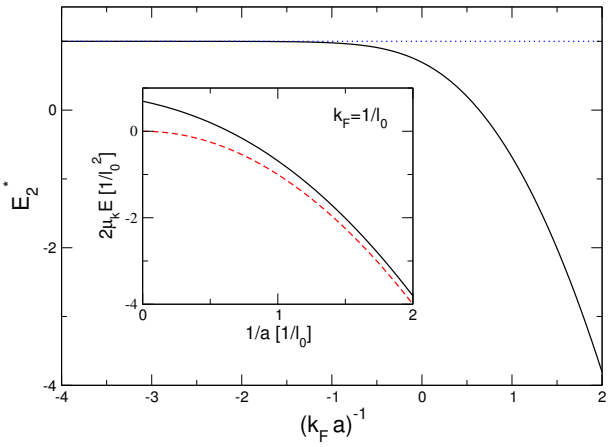

Figure 7.3.: The normalized energy $E_2^* = 2\mu_k E/k_F^2$ of the poles is depicted by the black solid line. The blue dotted line represents the boundary E_2^{th}. In the inset the pole energies, also depicted by the black solid line, are compared to the vacuum pole energies, depicted by the red dashed line, for a fixed Fermi momentum $k_F = 1\, l_0^{-1}$. In this case there is a free length scale l_0.

In the inset of Fig. 7.3 the poles were compared to the vacuum poles for positive scattering length and a fixed Fermi momentum. Note that a rescaling with k_F in this comparison is not possible since the vacuum poles do of course only exist for $k_F = 0$. It can be observed that the binding energies of the in-medium poles are reduced and that the two curves are close together if the scattering length is not too large. In this region the poles with negative binding energy can be related to bound states, e.g. diatomic molecules.

In the remainder of this thesis we denote states which are bound in position space as bound states. In this sense we do not refer to Cooper pairs as bound states. This convention enables a better linguistic distinction of Cooper pairs and bound states which are bound in position space.

In general, at $P = 0$ we can relate poles with positive energy to Cooper pairs and poles with negative energy to bound states. However, if the transition between Cooper pairs and bound dimers with zero total momentum is located at exactly zero energy, is uncertain. For finite momenta the vacuum pole energies are simply increased by the kinetic energy term $P^2/(2M_k)$. The dependence of the in-medium poles on P is more complicated as we will see in the following.

In Fig. 7.4 the pole energies are plotted against the total momentum P/k_F for various mass ratios with $k_F a = -10$. Hence, these poles are located in an area where Cooper pairs can be formed. As already identified, the curves have to start at the same value since the poles are independent of the mass ratio for zero total momentum. The curves show similar behavior for the plotted mass ratios from 1 to 10. The energy constantly rises until the threshold E_2^{th} is reached. Then the poles vanish. Consequently, the Cooper pairs can only be formed up to a certain maximal momentum. Note that in this context the maximal momenta for these curves are smaller than $2k_F$, which is the maximum total momentum for two particles inside the Fermi sphere. It can also be observed that the poles reach the threshold E_2^{th} at larger values of the total momentum if the mass ratio is increased. Hence, an increased mass ratio is associated with a larger momentum region where Cooper pairs can be formed. There is, however, a boundary.

For that purpose consider the curve with the mass ratio 20. Here, we can observe a different behavior. The energy of the pole also constantly rises, but it does not vanish when it crosses the threshold E_2^{th}. It should be pointed out that the intersection point lies outside the region $P \in [0, 2k_F]$. The curve also has an inflection point. For the mass ratios of 50 and 100 the curves have even a local minimum and maximum. Note, however, that the energy of the minimum is larger than the energy at zero momentum. The maximum energy gain is thus obtained for $P = 0$. For graphical reasons it can not be seen here that these curves also intersect the threshold E_2^{th} without vanishing afterwards. In general, we found that the poles vanish when they reach the threshold E_2^{th} in the region $P \in [0, 2k_F]$ for negative scattering lengths. This is a reasonable behavior. Two particles inside the Fermi sea have a maximum total momentum of $2k_F$ and a maximum kinetic energy of $k_F^2/(2\mu_k)$. Hence, in this framework their energy can not exceed this value. Otherwise it would cost energy to form a pair. In contrast, for momenta larger than $2k_F$ both particles can not belong to the Fermi sphere[2] and hence the kinetic energy boundary $k_F^2/(2\mu_k)$ no longer holds. There is also a boundary for these poles. If the energy reaches the value $\frac{1}{2\mu_k}(-\frac{m_j}{M}P + k_F)^2 + \frac{P^2}{2M}$ with $m_i > m_j$, the poles disappear. Using the definition of the relative momentum $\mathbf{p} = \frac{m_2}{M}\mathbf{p_1} - \frac{m_1}{M}\mathbf{p_2}$, it follows that the particle with mass m_i has the momentum $P - k_F$ and the particle with mass m_j has the momentum k_F, where both momenta are aligned and $m_i > m_j$. The interpretation of this boundary is indeed

[2] If a condensate is formed or at finite temperatures the Fermi sea smears out. However, this case is not considered here.

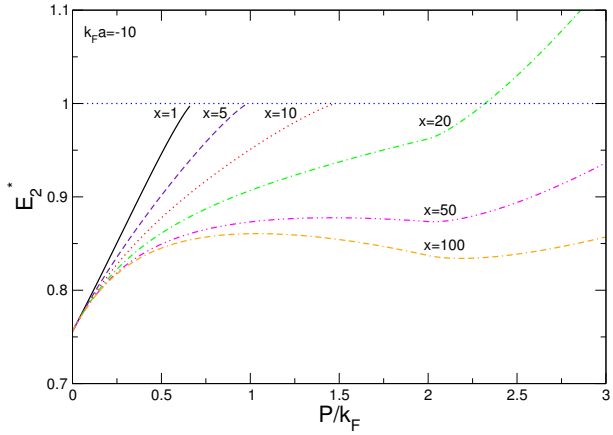

Figure 7.4.: The energy of the poles is plotted against the total momentum for various mass ratios x, which are 1, 5, 10, 20, 50 and 100. The blue dotted line represents the boundary E_2^{th} and the scattering length is given by $k_F a = -10$.

puzzling. Provided that one of the two particles is on the Fermi surface, the boundary would be the minimal kinetic energy for this configuration. Why this configuration dictates the boundary is an open question.

The appearance of these local extrema can be found in a large region of the scattering length. There are indeed two limiting cases. If the scattering length is small and negative, the pole energy is very close to the threshold at zero momentum. In this case the poles will disappear at the threshold E_2^{th} before they can develop a minimum even for high mass ratios. Certainly for very high mass ratios the pole energy for zero momentum has to be very close to the threshold so that no local extrema can be formed. Additionally, if the scattering lengths are small and positive the extrema do also disappear. In this case the binding energy becomes large and it seems that this impedes the appearance of the local extrema. Between these two regions we found the extrema to appear for mass ratios around 40 to 50. Before we continue with the next figure, we want to mention that we obtain a similar graph like Fig. 7.4 in the unitary limit $a_k \to \pm\infty$. Hence, we find the same physics to apply there.

In Fig. 7.5 the pole energies are plotted against the total momentum with the scattering length $a/l_0 = 1$ and the Fermi momentum $k_F l_0 = 1$. The mass ratios are 5 and 100. Since we also depict the kinetic energy of the center of mass $P^2/2M$ and the vacuum poles, we do not rescale with k_F. In both cases a reduced binding energy due to medium effects can be observed. For a mass ratio of 5 the in-medium and vacuum poles show a similar behavior. The binding energy is, however, reduced and the energy of the in-medium poles is distinctly smaller than the kinetic energy of the center of mass. In the graph with the mass ratio 100 the shaping of the local minimum and maximum can also be observed. For large momenta the in-medium and vacuum poles show as well the same behavior. Hence, in this region the poles can be related to bound states, independent of their mass ratio. Note that the reduced binding energy due to medium effects is a general trait of bound states in the medium.

In summary, in the region of negative scattering length and in the unitary limit there are poles with positive energy, which are Cooper pairs. Since in this region superfluid BCS phases appear, we refer to this region as BCS region[3]. On the other side for positive and not too large scattering length we have bound states with reduced binding energy. This region is referred to as BEC region. Between these two limits there is the BCS-BEC crossover region. The results in this region are indeed complicated. In this thesis we are focused on the negative scattering length region and the unitary limit $a \to \pm\infty$ and therefore will not discuss this sector. In [37] the crossover is discussed for equal masses. The situation is simpler for equal masses in the crossover region but it still conveys a good first insight. Another crucial point is that the assumption of a rigid Fermi sea is most likely justified in the BCS sector. In the BEC region bound states, which are bosons, can be formed. This formation of bound states leads to a dissolution of the Fermi sea.

Next we compare our two-body results to the two-body calculation of [43, 50] for the case of equal Fermi momenta. They found that their two-body calculations qualitatively predict main aspects of the many-body phase diagram. Since we make the assumption that our three-body calculation predicts some traits of the phase diagram concerning three-body physics, we compare the results of the two-body calculations. The assumptions on the considered system are the same. In [50] they also assume a contact interaction between two distinguishable fermions in presence of a filled Fermi sphere for each fermion species. Instead of a field theory approach, the Schrödinger equation is solved. These two applied approaches, solving the Schrödinger equation or using the EFT, are equivalent. The crucial difference is based on the assumption on the Fermi sea. In our case the Fermi sea is implemented by a restriction to the phase space.

[3] Note that in the context of BCS-BEC crossover the BCS region is usually referred to $k_F|a| \ll 1$ with $a < 0$.

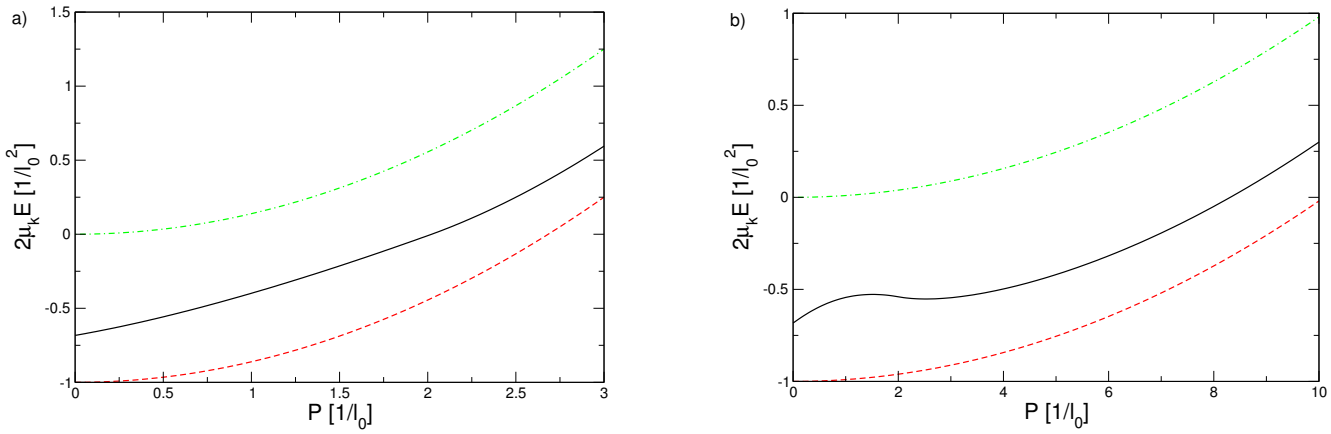

Figure 7.5.: The pole energies are plotted in dependence on the total momentum for $a = 1\ l_0$ and $k_F = 1\ l_0^{-1}$. The mass ratios are 5 (a) and 100 (b). The in-medium poles are represented by the black solid line, the vacuum poles by the red dashed line and the kinetic energy of the center of mass $P^2/(2M_k)$ (multiplied by $2\mu_k$) by the green dashed dotted line.

In [50] an approximation is used, which we will explain in the following. They define the kinetic energy as follows

$$\epsilon_i(k) = \left| \frac{k_i^2}{2m_i} - \frac{k_F^2}{2m_i} \right| , \tag{7.18}$$

where i denotes the fermion species and equal Fermi momenta are considered here. Direct restrictions to the phase space like theta functions are not included. The reference point of the kinetic energy is given by the Fermi surface. But this is only a convention. Using this scheme particles with momenta $0 < k_i < k_F$ can be added, which costs the energy $\frac{k_F^2}{2m_i} - \frac{k_i^2}{2m_i}$. This is the minimum energy one has to spend in order to replace the particle since the state inside the Fermi sphere is already occupied. This approximation indirectly includes the hole creation process. It is the main difference between our two approaches. Using theta functions instead of this kinetic energy definition the same results are obtained. Since in [50] the scattering length is considered to be in the unitary limit, we compared our results for this case. For equal Fermi momenta we observed the same qualitative behavior. However, the formation of the local minimum and maximum for large mass ratios was not detected in [50]. Vital for the phase diagram is the momentum with the largest energy gain. In the case of equal Fermi momenta the largest binding energy was found at zero momentum for both approaches.

We conclude that in the unitary limit for equal Fermi momenta the two different approaches yield comparable results concerning the phase diagram. This is our main result of this section.

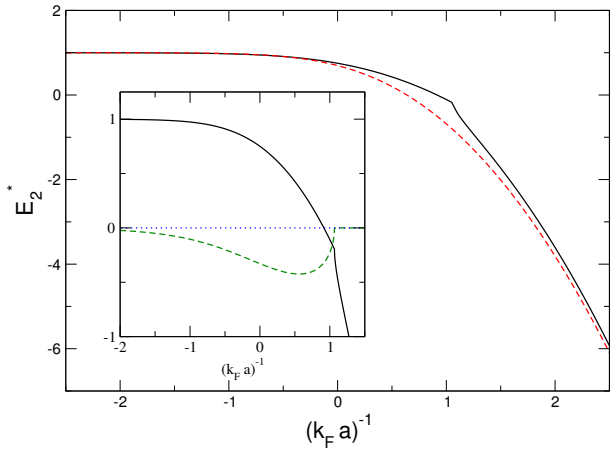

Figure 7.6.: The extended pole energies (black solid line) and the in-medium pole energies (red dashed line) are shown in dependence on $(k_F a)^{-1}$ for $P = 0$. In the inset the imaginary part of the extended poles (green dashed line) is additionally plotted. The blue dotted line represents the zero line.

In this section we discuss the poles with included hole propagation and compare them to our results without hole propagation and the results of [50]. To clarify the distinction between the two different in-medium poles, we denote the in-medium poles with included hole propagation by extended poles. The in-medium poles without hole propagation are still referred to as in-medium poles. Before we proceed, we have to discuss a general property of the extended poles. We always found two poles of the form $P_0 \pm i\Gamma$. In other words there exists a counterpart pole with reversed sign of the imaginary part for every pole. This holds for every pole with a nonzero imaginary part. Hence, the sign of the imaginary part is not fixed. In the subsequent discussion we will always use the negative imaginary part. The results of the loop integration $L_k^V(P_0, P)$ are given in appendix C. Note that for momenta larger than $2k_F$ the contribution of the hole propagation vanishes. This is evident because only hole-hole and particle-particle propagation occurs in the considered loop diagram and the maximal total momentum of two holes is $2k_F$. Hence, for $P \geq 2k_F$ the extended and in-medium poles are the same. For zero total momentum the following equation has to be solved.

$$\frac{1}{a_k} = \frac{1}{\pi}\left(4k_F + \sqrt{\sigma_k}\left(\ln(k_F - \sqrt{\sigma_k}) - \ln(k_F + \sqrt{\sigma_k})\right) + \sqrt{\overline{\sigma}_k}\left(\ln(k_F - \sqrt{\overline{\sigma}_k}) - \ln(k_F + \sqrt{\overline{\sigma}_k}) - \ln(-\sqrt{\overline{\sigma}_k}) + \ln(\sqrt{\overline{\sigma}_k})\right)\right) \tag{7.19}$$

The variable $\overline{\sigma}_k$ is given by $\overline{\sigma}_k = 2\mu_k(P_0 - i\epsilon)$. The variables σ_k and $\overline{\sigma}_k$ differ only in the sign of $i\epsilon$. We chose a form similar to the equation for in-medium poles with zero total momentum Eq. (7.17).

In Fig. 7.6 the in-medium pole and extended pole energies for zero total momentum $P = 0$ are depicted. Note that as well as in the previous case the extended poles are independent of the mass ratio for $P = 0$. The two curves lie very close together except for the crossover region. It can be observed that in this region the curve of the extended poles has a cusp in contrast to the in-medium poles. In the inset the real and imaginary part of the extended poles are shown. It becomes apparent that the cusp is located at the threshold where the imaginary part vanishes. In this framework the Cooper pairs possesses an imaginary part in contrast to bound states. The non-existent imaginary part of the bound states is not astonishing in this system since the imaginary part can be related to a decay. No other bound states are present. Therefore, no decay should appear in this non-relativistic framework. The Cooper pairs exhibit an imaginary part, which approaches zero in the limit $1/a_k \to -\infty$. The imaginary part of the Cooper pairs might be related to the picture that Cooper pairs permanently decay and new Cooper pairs between different particles are formed. Another intriguing detail is the aspect that the cusp is located in the negative energy region. Provided that all poles with an imaginary part can be identified as Cooper pairs, this would imply that Cooper pairs are not restricted to positive energy but can also a have a slightly negative energy.

Up to this point the inclusion of hole propagation seems to be a reasonable extension to our approach. However, the energies of the extended and in-medium poles are very close together in the BCS and BEC region.

We proceed with the discussion of the poles for finite momenta. In Fig. 7.7 a) the extended and in-medium poles are depicted in the unitary limit with a mass ratio of 10. It is shown that both curves vanish at the threshold E_2^{th} as expected. The form of the curves differ. One curve bears resemblance to a convex curve and the other to a concave curve at the depicted scale, except for the inset. For comparison in Fig. 7.7 b) the results of [50] for the same parameters are shown. The curve of the extended poles rather corresponds to the two-body results of [50]. Nevertheless, there is a huge

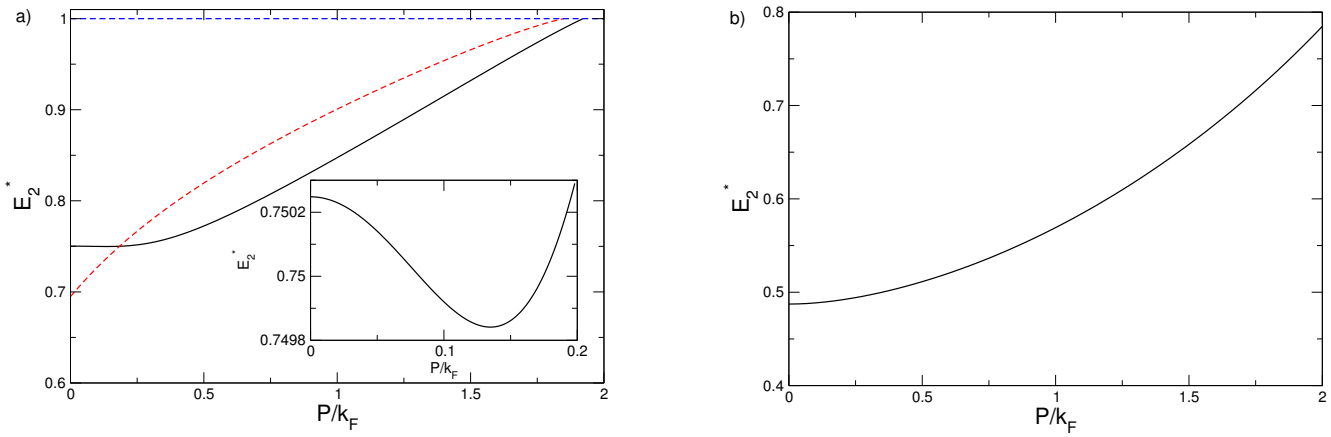

Figure 7.7.: a) In this graph the normalized energy of the extended poles (black solid line) and the in-medium poles (red dashed line) line are pictured as a function of the normalized total momentum in the unitary limit $1/a = 0$. The blue dashed line represents the threshold E_2^{th}. The mass ratio is 10. In the inset a segment of a small momentum region is shown. b) For comparison, the Cooper pair results of [50] are depicted for the same parameters. Data taken from [50].

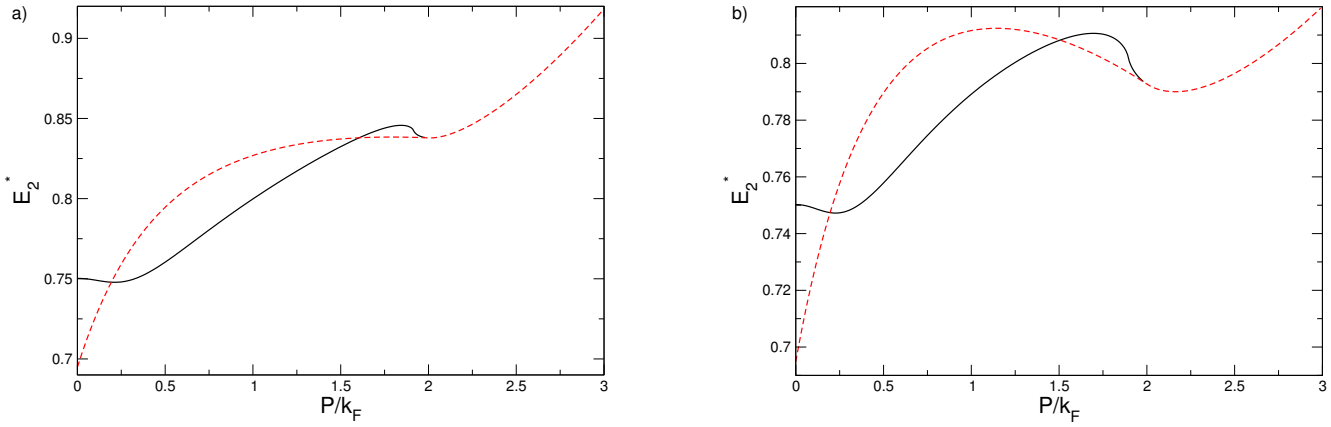

Figure 7.8.: The extended (black solid line) and in-medium pole (red dashed line) energies are plotted against the total momentum in the unitary limit. The mass ratio is 40 (a) and 80 (b). The extended poles are plotted up to $2k_F$ since the hole contribution vanishes at this point.

qualitative difference, which might be missed at first glance. In the inset, which focuses on a small momentum region near to zero, it is obvious that the curve has a absolute minimum at a nonzero momentum. Although the minimum is shallow, it is a clear contradiction to the results of [50]. Since the minimum is a total minimum, it is energetically favorable to form Cooper pairs with finite momentum. This would lead to a different phase. However, the results of [50] suggest for equal Fermi momenta a phase with zero total momentum independent of the mass ratio. Recall that the in-medium poles also develop a minimum for high mass ratios, the energy gain for zero total momentum was indeed larger. Hence, in this case a phase with $P = 0$ is still preferred.

In general, we found this global minimum for mass ratios around 6, 7 and larger for negative scattering lengths and in the unitary limit. For higher mass ratios the minima are in general more distinct. In the region of small negative scattering length, where the energy is close to the threshold, the minima can be indeed very shallow.

In Fig. 7.8 the extended and in-medium pole energies are depicted as a function of P/k_F in the unitary limit for higher mass ratios of 40 and 80. Recall that the contribution of the hole propagation vanishes at $P = 2k_F$ since the maximal momentum of a hole pair inside the Fermi sea is $2k_F$. Consequently, the curves of the extended and in-medium poles have to merge at $P = 2k_F$. The extended poles are explicitly only drawn up to $2k_F$. Related to this is the remaining presence of the local minima, which we observed in the in-medium pole section. This puzzling circumstance does not disappear. In contrast, now some kind of shallow peak can already be seen for a mass ratio of 12 in the unitary limit. The curves of the extended poles change rather rapidly near $P = 2k_F$. This could be interpreted as a hint that the hole contributions from additional Feynman graphs are missing in this region.

We also want to mention the role of the imaginary part at this point. Due to the vanishing hole contribution at $2k_F$, the imaginary part also disappears at $2k_F$. Provided that the imaginary part is an indicator of a Cooper pair, the Cooper pairs would in this context continuously merge into a different kind of state. Note that this behavior is observed in the BCS region where no bound states exist. This can be interpreted that at $P = 2k_F$ this model breaks down. However, a new kind of state could also appear at this special point at the border of the Fermi sphere.

In summary, for zero total momentum the results with included hole propagation are reasonable. The appearance of the imaginary part for Cooper pairs conveys the impression that including hole propagation is an appropriate extension. However, recall that the energy of the poles with and without included hole propagation is very close together except for the crossover region. The results for nonzero total momentum contradict the results of the in-medium case and of [50]. We found a total minimum of the energy at finite momenta for mass ratios larger than approximately 6, which would lead to a different phase. Additionally, the imaginary part of the poles vanishes for momenta $P > 2k_F$, which appears to be inconsistent. From this we draw the conclusion that the incorporation of the hole propagation in this way is not advisable. Taken into account the approximation of [50], which allows particles to infiltrate into the Fermi sea, and the results for $P = 0$, it seems to be necessary to include additional Feynman diagrams in order to get an improvement. Our results for $P = 0$ suggest that these contributions become significant for nonzero momentum. Which class of diagrams have to be included is, however, an open question just as the question if the required diagrams can be deduced from the kinetic energy approximation.

Our main result of this section is that our results contradict the results of [50] if hole propagation is included. We will therefore stick to our approach without holes in the three-body sector.

8 Three-body Scattering Amplitude

8.1 Derivation of the Scattering Amplitude

In this section we discuss the calculation of the three-body scattering amplitude in the medium. The same assumptions as in the two-body system are considered. The system is just extended to three particles. We repeat the attributes. Three distinguishable fermions are regarded in presence of a Fermi sphere for each of the fermion species. All states up to the Fermi momentum, which is the same for all three fermion species, are occupied. The three fermions do only interact among each other and are outside the Fermi sphere. An interaction between the selected particles and the Fermi sphere is not present. Due to the discussed reasons in the previous chapter, hole propagation is not considered.

The Feynman diagram of the three-particle scattering amplitude $\mathscr{A}_{ij}(\mathbf{p},\mathbf{k},E,E_i,E_j)$ for zero total momentum is shown in Fig. 8.1. We consider one incoming and one outgoing dimer as well as one incoming and one outgoing fermion. Note that the incoming and outgoing dimers do not have to be bound states. In this case the scattering amplitude is just arranged that way. To obtain the amplitude for three particles in the initial and final state, the amplitude only has to be multiplied with two vertex factors. The indices i and j denote the incoming and outgoing particles, respectively. The fermions contained in the dimer propagator are also specified by these indices. Similarly, the incoming and outgoing momenta are denoted by $\mathbf{p}$ and $\mathbf{k}$. We restrict the total momentum to be zero since otherwise the boundary conditions due to the theta functions as well as the integration in general become very difficult. The total energy is given by E.

The scattering amplitude equation is an integral equation with one inhomogeneous and two homogeneous parts. Since two different dimers can be formed in the intermediate state, we have to consider two homogeneous contributions. In chapter 8.2 we discuss the properties of the three-body scattering amplitude in the vacuum. There it is discussed why no explicit three-body force has to be incorporated. Note that the scattering amplitude depends on the cutoff due to the missing three-body force. The scattering amplitude can be written as

$$\begin{aligned} i\mathscr{A}_{ij}(\mathbf{p},\mathbf{k},E,E_i,E_j) = &-\frac{g_i g_j}{4}\frac{i\theta(|\mathbf{p}+\mathbf{k}|-k_F)}{E-E_i-E_j-\frac{(\mathbf{p}+\mathbf{k})^2}{2m_{ij}}+i\epsilon}\cdot(1-\delta_{ij}) \\ &-\sum_{k=0}^{2}\frac{g_i g_k}{4}\int_{|\mathbf{q}|<\Lambda}\frac{d^4q}{(2\pi)^4}\frac{i\theta(q-k_F)}{q_0-\frac{q^2}{2m_k}+i\epsilon}\cdot\frac{i\theta(|\mathbf{p}+\mathbf{q}|-k_F)}{E-E_i-q_0-\frac{(\mathbf{p}+\mathbf{q})^2}{2m_{ki}}+i\epsilon} \\ &\times iD_k(E-q_0,q)\cdot(1-\delta_{ik})\cdot i\mathscr{A}_{kj}(\mathbf{q},\mathbf{k},E,q_0,E_j)\,. \end{aligned} \tag{8.1}$$

We use the following notation for masses with two indices. The mass m_{ij} denotes the mass of particle k with $m_{ij}=m_k$ and $i\neq j\neq k$. We set the energies of fermions i and j, which are denoted by E_i and E_j, on shell. This yields

$$\begin{aligned} i\mathscr{A}_{ij}(\mathbf{p},\mathbf{k},E) = &-\frac{g_i g_j}{4}\frac{i\theta(|\mathbf{p}+\mathbf{k}|-k_F)}{E-\frac{p^2}{2m_i}-\frac{k^2}{2m_j}-\frac{(\mathbf{p}+\mathbf{k})^2}{2m_{ij}}+i\epsilon}\cdot(1-\delta_{ij}) \\ &-\sum_{k=0}^{2}\frac{g_i g_k}{4}\int_{|\mathbf{q}|<\Lambda}\frac{d^4q}{(2\pi)^4}\frac{i\theta(q-k_F)}{q_0-\frac{q^2}{2m_k}+i\epsilon}\cdot\frac{i\theta(|\mathbf{p}+\mathbf{q}|-k_F)}{E-\frac{p^2}{2m_i}-q_0-\frac{(\mathbf{p}+\mathbf{q})^2}{2m_{ki}}+i\epsilon} \\ &\times iD_k(E-q_0,q)\cdot(1-\delta_{ik})\cdot i\mathscr{A}_{kj}(\mathbf{q},\mathbf{k},E)\,. \end{aligned} \tag{8.2}$$

Next we perform the contour integration. The dimer propagator we have to integrate over is $D_k(E-q_0,q)$. Hence, the cuts of the dimer propagator are all in the upper complex plane. Recall that the sign of the infinitesimal $i\epsilon$ was the same in all terms of the dimer propagator. The pole of the dimer propagator can only be determined numerically. However, we always found at most one pole, which has an infinitesimal negative imaginary part. Due to the argument $E-q_0$ the pole of the dimer propagator is located in the upper complex plane. To avoid all these difficulties, we integrate over the lower complex plane, where no poles and cuts are present. At this point we also want to come back briefly to the in-medium dimer with included hole propagation and make some remarks. This dimer propagator contains the arguments b_k and $\bar{b}_k$ which originate from particle and hole contributions, respectively. The signs of the imaginary parts of b_k and $\bar{b}_k$ are different. This dimer propagator therefore has cuts in the upper as well as in the lower complex plane and would

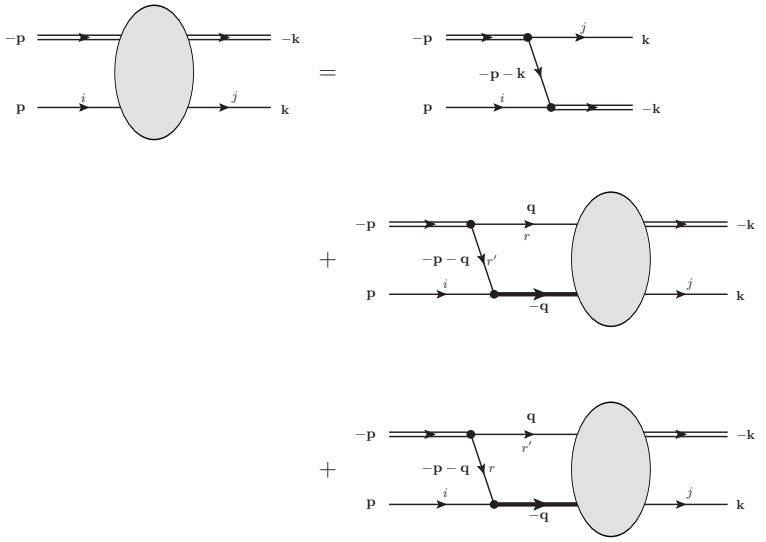

Figure 8.1.: Feynman diagram of the three-particle scattering amplitude. Figure taken from my diploma thesis [37].

make the contour integration extremely difficult. In addition, this dimer propagator also has a pole in both complex half planes, which we can only calculate numerically. Implementing the in-medium dimer propagator with hole propagation is therefore very difficult. We return to the calculation of the scattering amplitude. The contour integration gives

$$\begin{aligned} i\mathscr{A}_{ij}(\mathbf{p},\mathbf{k},E) = &-\frac{1}{4}g_i g_j \frac{i\theta(|\mathbf{p}+\mathbf{k}|-k_F)}{E-\frac{p^2}{2m_i}-\frac{k^2}{2m_j}-\frac{(\mathbf{p}+\mathbf{k})^2}{2m_{ij}}+i\epsilon}\cdot(1-\delta_{ij}) \\ &+ i\sum_{k=0}^{2}\frac{1}{4}g_i g_k \int_{|\mathbf{q}|<\Lambda}\frac{d^3q}{(2\pi)^3}\frac{\theta(q-k_F)\cdot\theta(|\mathbf{p}+\mathbf{q}|-k_F)}{E-\frac{p^2}{2m_i}-\frac{q^2}{2m_k}-\frac{(\mathbf{p}+\mathbf{q})^2}{2m_{ik}}+i\epsilon}\cdot(1-\delta_{ik}) \\ &\times D_k(E-\tfrac{q^2}{2m_k},q)\cdot\mathscr{A}_{kj}(\mathbf{q},\mathbf{k},E)\,. \end{aligned} \tag{8.3}$$

We multiply the incoming and outgoing dimers with the wave function renormalization constants $\sqrt{|Z|}$. The renormalized amplitude is then defined by

$$\mathscr{A}^R_{ij}(\mathbf{p},\mathbf{k},E) = \sqrt{|Z_i||Z_j|}\mathscr{A}_{ij}(\mathbf{p},\mathbf{k},E)\,. \tag{8.4}$$

The Z factors are the residues of the dimer propagator poles. In this thesis we are solely interested in the poles of the three-body amplitude. The renormalization of the scattering amplitude leaves the poles unaffected. Since we can not calculate the dimer propagator poles analytically, we use the residues of the vacuum poles. The benefit of the renormalization with the residues of the vacuum poles is that the amplitude becomes independent of the unphysical coupling constants. We calculated the Z-factors of the vacuum poles in chapter 7. They are given by $Z_i = \frac{8\pi}{g_i^2\mu_i^2 a_i}$.

Before we proceed, we briefly discuss the role of the incoming and outgoing states. Depending on the scattering length, we can have a cooper pair, a bound dimer or simply three free particles in the initial and final state. Accordingly, we have to consider slightly different scattering processes. However, since only the initial and final states are changed, the scattering amplitude changes only by a multiplied function. The three-body poles remain unchanged by this procedure. Consequently, the considered scattering amplitude $\mathscr{A}^R_{ij}$ contains all three-body poles of the different scattering processes.

Using (6.4) and (7.6) one can show that

$$g_k = \left(\frac{\mu_k}{4\pi a_k} - \frac{\mu_k\Lambda}{2\pi^2}\right)^{-1}\,. \tag{8.5}$$

From this follows that the coupling constants g_k are negative due to the large cutoff Λ compared to $1/a_k$. The square root $\sqrt{|Z_i||Z_j|}$ can thus be written as $8\pi/(g_i g_j \mu_i \mu_j \sqrt{|a_i||a_j|})$. Using this relation we obtain

$$\begin{aligned}
i\mathscr{A}^R_{ij}(\mathbf{p},\mathbf{k},E) =& -\frac{1}{4} g_i g_j \frac{i\theta(|\mathbf{p}+\mathbf{k}|-k_F)}{E-\frac{p^2}{2m_i}-\frac{k^2}{2m_j}-\frac{(\mathbf{p}+\mathbf{k})^2}{2m_{ij}}+i\epsilon}\cdot(1-\delta_{ij})\sqrt{|Z_i||Z_j|} \\
&+ i\sum_{k=0}^{2}\frac{1}{4} g_i g_k \int_{|\mathbf{q}|<\Lambda}\frac{d^3q}{(2\pi)^3}\frac{\theta(q-k_F)\cdot\theta(|\mathbf{p}+\mathbf{q}|-k_F)}{E-\frac{p^2}{2m_i}-\frac{q^2}{2m_k}-\frac{(\mathbf{p}+\mathbf{q})^2}{2m_{ik}}+i\epsilon}\cdot(1-\delta_{ik}) \\
&\times D_k(E-\tfrac{q^2}{2m_k},q)\cdot\mathscr{A}^R_{kj}(\mathbf{q},\mathbf{k},E)\frac{\sqrt{|Z_i||Z_j|}}{\sqrt{|Z_k||Z_j|}} \\
=& -\frac{2\pi}{\mu_i\mu_j\sqrt{|a_i||a_j|}}\frac{i\theta(|\mathbf{p}+\mathbf{k}|-k_F)}{E-\frac{p^2}{2m_i}-\frac{k^2}{2m_j}-\frac{(\mathbf{p}+\mathbf{k})^2}{2m_{ij}}+i\epsilon}\cdot(1-\delta_{ij}) \\
&+ i\sum_{k=0}^{2}\frac{2\pi\sqrt{|a_k|}}{\mu_i\sqrt{|a_i|}}\int_{|\mathbf{q}|<\Lambda}\frac{d^3q}{(2\pi)^3}\frac{\theta(q-k_F)\cdot\theta(|\mathbf{p}+\mathbf{q}|-k_F)}{E-\frac{p^2}{2m_i}-\frac{q^2}{2m_k}-\frac{(\mathbf{p}+\mathbf{q})^2}{2m_{ik}}+i\epsilon}\cdot(1-\delta_{ik}) \\
&\times\left[\frac{1}{a_k}-\frac{1}{\pi}L_k\left(E-\tfrac{q^2}{2m_k},q\right)\right]^{-1}\cdot\mathscr{A}^R_{kj}(\mathbf{q},\mathbf{k},E)\,. \qquad (8.6)
\end{aligned}$$

(8.7)

In the last equation we used the explicit form of the dimer propagator

$$iD_k(P_0,P) = i\frac{8\pi}{\mu_k g_k^2}\left[\frac{1}{a_k}-\frac{1}{\pi}L_k(P_0,P)\right]^{-1}.$$

The scattering amplitude is now independent of the coupling constants. Instead it depends on the scattering lengths. We define the following abbreviation in order to write the amplitude in a more compact way

$$\begin{aligned}
t_{ij}(p,k,\theta_k,E) =& \frac{(1-\delta_{ij})}{E-\frac{p^2}{2m_i}-\frac{k^2}{2m_j}-\frac{(\mathbf{p}+\mathbf{k})^2}{2m_{ij}}+i\epsilon} \\
=& \frac{(1-\delta_{ij})}{E-\frac{p^2}{2}(\frac{1}{m_i}+\frac{1}{m_{ij}})-\frac{k^2}{2}(\frac{1}{m_j}+\frac{1}{m_{ij}})-\frac{pk\cos\theta_k}{m_{ij}}+i\epsilon} \\
=& \frac{(1-\delta_{ij})}{E-\frac{p^2}{2\mu_j}-\frac{k^2}{2\mu_i}-\frac{pk\cos\theta_k}{m_{ij}}+i\epsilon}\,, \qquad (8.8)
\end{aligned}$$

where θ_k is the angle between $\mathbf{p}$ and $\mathbf{k}$. We also define the dimer propagator without prefactors

$$D'_k(q,E) = \left[\frac{1}{a_k}-\frac{1}{\pi}L_k\left(E-\tfrac{q^2}{2m_k},q\right)\right]^{-1}. \qquad (8.9)$$

We will now switch to spherical coordinates. We choose the z axis to be aligned parallel to $\mathbf{p}$. The amplitude depends on the absolute values of $\mathbf{p},\mathbf{q}$ and $\mathbf{k}$ as well as on the angles $\theta_q = \sphericalangle(\mathbf{p},\mathbf{q})$, $\theta_k = \sphericalangle(\mathbf{p},\mathbf{k})$ and $\tilde{\theta} = \sphericalangle(\mathbf{q},\mathbf{k})$. However, we have to explicitly integrate over the angle θ_q and thus implicitly over $\tilde{\theta}$ as well as over $|\mathbf{q}|$. The integration over ϕ_q is trivial in this case and yields 2π. In summary the amplitude depends on the absolute values $|\mathbf{p}|$, $|\mathbf{k}|$, the energy E and the angle θ_k. Certainly the scattering amplitude depends implicitly on the Fermi momentum and the cutoff. Using the above definitions we obtain

$$\begin{aligned}
i\mathscr{A}^R_{ij}(p,k,\theta_k,E) =& -\frac{2\pi i}{\mu_i\mu_j\sqrt{|a_i||a_j|}}\theta(|\mathbf{p}+\mathbf{k}|-k_F)t_{ij}(p,k,\theta_k,E) \\
&+ i\sum_{k=0}^{2}\frac{1}{2\pi\mu_i}\sqrt{\frac{|a_k|}{|a_i|}}\int_{-1}^{1}d\cos\theta_q\int_{k_F}^{\Lambda}dq\,q^2\theta(|\mathbf{p}+\mathbf{q}|-k_F) \\
&\times t_{ik}(p,q,\theta_q,E)\,D'_k(q,E)\cdot\mathscr{A}^R_{kj}(q,k,\tilde{\theta},E)\,. \qquad (8.10)
\end{aligned}$$

The lower boundary of the integral is already shifted so that the theta function $\theta(q-k_F)$ can be omitted. The three angles θ_q,θ_k and $\tilde{\theta}$ are not independent as can easily be seen by their definitions. This can cause problems within the integration. We therefore apply a partial wave decomposition to avoid this issue. The partial wave decomposition can be written as

$$\mathscr{A}_{ij}^R(p,k,\theta_k,E) = \sum_{l=0}^{\infty} (\mathscr{A}_{ij}^R)_l(p,k,E)(2l+1)P_l(\cos\theta_k)\,, \tag{8.11}$$

with the Legendre polynomials $P_l(x)$. The decomposition into partial waves is applicable if the potential is spherically symmetric. Since our Lagrangian contains only contact interactions, which correspond to delta functions in the position space, the requirement is fulfilled. In this thesis we are interested in the poles of the scattering amplitude. Therefore, we focus on zero total angular momentum. However, we first state the general case. Applying (8.11) we obtain

$$\begin{aligned} i(\mathscr{A}_{ij}^R)_l(p,k,E) = &-\frac{\pi i}{\mu_i\mu_j\sqrt{|a_i||a_j|}}\int_{-1}^{1} d\cos\theta_k\, P_l(\cos\theta_k)\,\theta(|\mathbf{p}+\mathbf{k}|-k_F)t_{ij}(p,k,\theta_k,E) \\ &+ i\sum_{k=0}^{2}\frac{1}{2\pi\mu_i}\sqrt{\frac{|a_k|}{|a_i|}}\int_{-1}^{1} d\cos\theta_q\int_{k_F}^{\Lambda} dq\, q^2 P_l(\cos\theta_q)\,\theta(|\mathbf{p}+\mathbf{q}|-k_F) \\ &\times t_{ik}(p,q,\theta_q,E)\,D_k'(q,E)\cdot(\mathscr{A}_{kj}^R)_l(q,k,E)\,. \end{aligned} \tag{8.12}$$

A derivation of this formula for equal masses can e.g. be found in [37] or for unequal masses in the vacuum in [44]. Next we discuss the boundary condition implied by the theta function $\theta(|\mathbf{p}+\mathbf{q}|-k_F)$. The integration variable q is larger than the Fermi momentum $q \geq k_F$. Hence, if $\mathbf{p}$ and $\mathbf{q}$ are aligned in the same direction, the theta function is always one. The theta function implies a restriction to the angular integration and not to the integration over q. The other theta function $\theta(|\mathbf{p}+\mathbf{k}|-k_F)$ can be treated similar. Note that the scattering fermions are outside the Fermi sphere. For the computation of the poles the inhomogeneous part of the scattering amplitude is irrelevant as we will see later.

The theta function in the homogeneous part restricts the integration over the angle θ_q. Since the theta function is one if the two momenta are aligned in the same direction, we have to determine the minimal angle. A short calculation reveals it to be

$$\cos\theta_g = \frac{k_F^2-p^2-q^2}{2pq}\,, \tag{8.13}$$

where θ_g is the limiting angle. Of course if $|p-q|>k_F$, the theta function is one for all angles. Hence, the theta function can be omitted in this case. We will now compute the angular integration separately for both cases. The boundaries are first denoted by g_1 and g_2. Subsequently, we insert the explicit values. We consider the angular integral I_l

$$\begin{aligned} I_l &= \int_{-1}^{1} d\cos\theta_q\, P_l(\cos\theta_q)t_{ik}(p,q,\theta_q,E)\Theta(|\mathbf{p}+\mathbf{q}|-k_F) \\ &= \int_{-1}^{1} d\cos\theta_q\, P_l(\cos\theta_q)\,\frac{(1-\delta_{ik})}{E-\frac{p^2}{2\mu_k}-\frac{q^2}{2\mu_i}-\frac{pq\cos\theta_q}{m_{ik}}+i\epsilon}\Theta(|\mathbf{p}+\mathbf{q}|-k_F) \\ &= \frac{m_{ik}}{pq}\int_{-1}^{1} d\cos\theta_q\, P_l(\cos\theta_q)\,\frac{(1-\delta_{ik})}{c_{ik}(p,q)-\cos\theta_q}\Theta(|\mathbf{p}+\mathbf{q}|-k_F)\,, \end{aligned} \tag{8.14}$$

with the definition

$$c_{ik}(p,q) = \frac{m_{ik}}{pq}\left(E-\frac{p^2}{2\mu_k}-\frac{q^2}{2\mu_i}+i\epsilon\right). \tag{8.15}$$

We focus on the S-wave. In this case the Legendre polynomial is simply one. In the next step the theta function is replaced by the boundaries g_1 and g_2 and we define $x=\cos\theta_q$.

$$I_0 = \frac{m_{ik}}{pq}\int_{g_1}^{g_2} dx\,\frac{(1-\delta_{ik})}{c_{ik}(p,q)-x} = -(1-\delta_{ik})\frac{m_{ik}}{pq}\left[\ln(c_{ik}(p,q)-x)\right]_{g_1}^{g_2} \tag{8.16}$$

Case $|p-q|>k_F$: $g_1=-1$ and $g_2=+1$

$$I_0 = -(1-\delta_{ik})\frac{m_{ik}}{pq}\left[\ln(c_{ik}(p,q)-x)\right]_{-1}^{+1} = (1-\delta_{ik})\frac{m_{ik}}{pq}\Big(\ln(c_{ik}(p,q)+1)-\ln(c_{ik}(p,q)-1)\Big) \tag{8.17}$$

Case $|p-q| < k_F$: $g_1 = \cos\theta_g$ and $g_2 = +1$

$$I_0 = -(1-\delta_{ik})\frac{m_{ik}}{pq}\left[\ln(c_{ik}(p,q)-x)\right]_{\cos\theta_g}^{+1} = (1-\delta_{ik})\frac{m_{ik}}{pq}\Big(\ln(c_{ik}(p,q)-\cos\theta_g)-\ln(c_{ik}(p,q)-1)\Big) \tag{8.18}$$

We merge the two cases into the variable $Q_{ik}(p,q,E)$

$$\begin{aligned} Q_{ik}(p,q,E) = \frac{m_{ik}}{pq}\Big\{&\Theta(|p-q|-k_F)\Big(\ln(c_{ik}(p,q)+1)-\ln(c_{ik}(p,q)-1)\Big) \\ &+\Theta(k_F-|p-q|)\Big(\ln(c_{ik}(p,q)-\cos\theta_g)-\ln(c_{ik}(p,q)-1)\Big)\Big\}\,, \end{aligned} \tag{8.19}$$

and finally obtain the expression for the S-wave scattering amplitude

$$\begin{aligned} i(\mathscr{A}_{ij}^R)_0(p,k,E) &= -i(1-\delta_{ij})\frac{\pi}{\mu_i\mu_j\sqrt{|a_i||a_j|}}Q_{ij}(p,k,E) \\ +i\sum_{k=0}^{2}(1-\delta_{ik})\frac{1}{2\pi\mu_i}\frac{\sqrt{|a_k|}}{\sqrt{|a_i|}}&\int_{k_F}^{\Lambda}dq\,q^2Q_{ik}(p,q,E)D_k'(q,E)(\mathscr{A}_{kj}^R)_0(q,k,E)\,. \end{aligned} \tag{8.20}$$

The scattering amplitude $(\mathscr{A}_{ij}^R)_0(p,k,E)$ contains all information about three-body observables with zero total angular momentum and zero total momentum. To determine the poles of the scattering amplitude we can simplify this equation a bit. We use the fact that the residues of the poles can be decomposed into a product of functions depending on p and q [1,51]

$$(\mathscr{A}_{ij}^R)_0(p,k,E) \longrightarrow \frac{\mathscr{B}_i^\dagger(p)\cdot\mathscr{B}_j(k)}{E+E_B} \quad \text{for } E\to -E_B\,, \tag{8.21}$$

where E_B is a pole energy of the scattering amplitude. Comparing the residues on both sides yields

$$\mathscr{B}_i^\dagger(p) = \sum_{k=0}^{2}(1-\delta_{ik})\frac{1}{2\pi\mu_i}\frac{\sqrt{|a_k|}}{\sqrt{|a_i|}}\int_{k_F}^{\Lambda}dq\,q^2Q_{ik}(p,q,E)D_k'(q,E)\,\mathscr{B}_k^\dagger(q)\,. \tag{8.22}$$

This is the final equation for the determination of the pole energies. The inhomogeneous part has disappeared and we obtained a homogeneous integral equation, which is a Fredholm equation of second kind. This equation has to be solved numerically. A numerical treatment can e.g. be found in [52].

8.2 Summary of Vacuum Results

In this section we briefly outline the characteristics of the three-body spectrum in the vacuum. An extensive presentation can be found in [1]. Primarily, in [1] three identical bosons are considered. However, the results can be applied for three distinguishable particles with equal masses and equal scattering lengths. In Fig. 8.2 the three-body spectrum in dependence on the inverse scattering lengths is depicted. The energy variable K is defined by $K = \mathrm{sgn}(E)(m|E|\hbar^2)^{1/2}$, where m is the mass of the particles. In the unitary limit, where the inverse scattering lengths are zero, the Efimov effect becomes apparent. The spectrum becomes geometric at this point and the binding energy of the Efimov trimers obeys the relation $E_T^{(n+1)}/E_T^{(n)} \to e^{-2\pi/s_0}$ as $n\to\infty$ for $a\to\pm\infty$, where s_0 is a transcendental number with $s_0 \approx 1.00624$. Hence, at zero energy we have an accumulation point of Efimov trimers and in general there are infinitely many Efimov trimers in this spectrum. The Efimov trimers vanish at two distinct thresholds, which are represented by the hatched area. For positive scattering lengths the threshold is the dimer binding energy, which is given by $\hbar^2/(ma^2)$. Hence, in this plot the dimer energy is depicted by a straight line. The trimers do also disappear for negative scattering lengths when their binding energy goes to zero. The trimers then decay into three particles. The values of $1/a$ where the trimers vanish differ by multiples of e^{π/s_0} for the atom-dimer threshold as well as the three particle threshold.

The qualitative traits of the spectrum are determined by the scattering length. However, the explicit binding energies of the trimers depend on an additional three-body parameter. Commonly, a three-body binding wave number κ^* is defined by $E_T^{(n)} \to (e^{-2\pi/s_0})^{n-n_*}\hbar^2\kappa_*^2/m$ as $n\to\infty$ for an arbitrary integer n_* so that the binding wave number is defined up to multiples e^{π/s_0}. Using κ^* there exists the following nontrivial discrete scaling symmetry

$$\kappa^* \to \kappa^* \quad , \quad a\to\lambda_0^m a \quad , \quad E\to\lambda_0^{-2m}E\,, \tag{8.23}$$

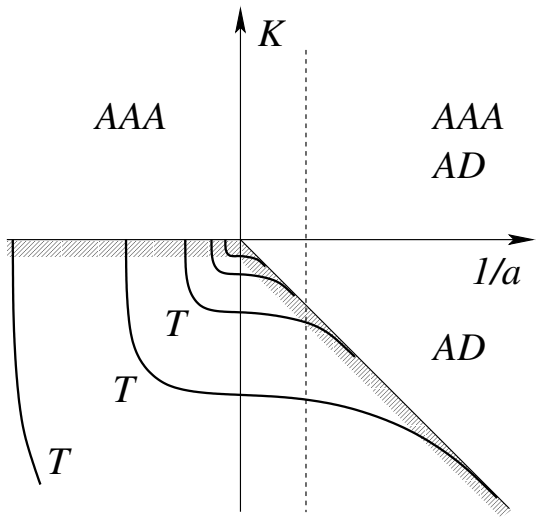

Figure 8.2.: Energy spectrum of three identical bosons. Figure taken from [53].

where λ_0 is defined by $\lambda_0 = e^{\pi/s_0} \approx 22.7$. Three-body observables scale under this transformation with integer powers of λ_0, where the power of λ_0 can be deduced by dimensional analysis. The three-body spectrum maps onto itself under this discrete scale transformation.

Calculating three-body observables numerically implies the use of a cutoff Λ. In this case only a finite number of branches is present with binding energies up to the order of Λ^2. When the cutoff is increased by multiples of λ_0 new pole branches appear. The associated limit cycle manifests itself in the three-body coupling constant g_3 of the three-body contact interaction. The functional form of the three-body coupling is given by

$$g_3(\Lambda) = -\frac{9g_2^2}{\Lambda^2} H(\Lambda) = -\frac{9g_2^2}{\Lambda^2} \cdot \frac{\cos[s_0 \ln(\Lambda/\Lambda_*) + \arctan(s_0)]}{\cos[s_0 \ln(\Lambda/\Lambda_*) - \arctan(s_0)]} \text{ as } \Lambda \to \infty, \tag{8.24}$$

where Λ_* is related to κ^* and is defined up to multiplicative factors of e^{π/s_0}. The function $H(\Lambda)$ displays the limit cycle. An important property of $H(\Lambda)$ is that it vanishes for certain values of Λ:

$$\Lambda_n = (e^{\pi/s_0})^n \exp([\tfrac{1}{2}\pi - \arctan s_0]/s_0)\,\Lambda_* \,. \tag{8.25}$$

For every three-body parameter Λ_* we can find values Λ_n of the cutoff at which $H(\Lambda)$ and consequently g_3 vanishes. This trait justifies our procedure to include only a two-body coupling and no three-body interaction. To obtain physical results in our approach the cutoff has to be matched to a three-body observable. The cutoff is then fixed and other three-body observables can be predicted. Note that the cutoff is fixed only up to multiples of λ_0. Another consequence is that the cutoff Λ in our approach can be related to a three-body coupling.

The outline considered three identical bosons and three distinguishable particles, respectively, with equal masses. The general features do also apply for three distinguishable particles with unequal masses. However, the scaling factor λ_0 changes. In Fig. 8.3 the scaling factor is depicted as a function of the mass ratio m_1/m_3 for two equal masses $m_1 = m_2$ and one different mass m_3. Keep in mind that the scaling factors approaches a value 15.7 for mass ratios m_1/m_3 smaller than one and approaches the value 1 for mass ratios larger than one.

8.3 Results

In this section the three-body in-medium pole structure is discussed. Especially, we are interested how the universal properties transfer to the medium. In the remainder of this chapter we consider two masses to be equal. Nevertheless, all three particles are assumed to be distinguishable. We use the convention that the masses of particles one and two are equal $m_1 = m_2$. The mass ratio is thus given by m_1/m_3. Similar to the two-body case but extended to three particles, we define the normalized three-body energy to be $E_3^* = E \cdot 2\mu^{(3)}/k_F^2$, where $\mu^{(3)}$ is the three particle reduced mass $\frac{1}{\mu^{(3)}} = \frac{1}{m_1} + \frac{1}{m_2} + \frac{1}{m_3}$. Recall that we refer to bound states as states which are bound in position space.

Comparison of the spectrum to the vacuum case

At the beginning of this section, we want to clarify which results were already obtained in my diploma thesis. As mentioned before, only equal masses were considered. It was examined how the energy of the bound states is changed by the

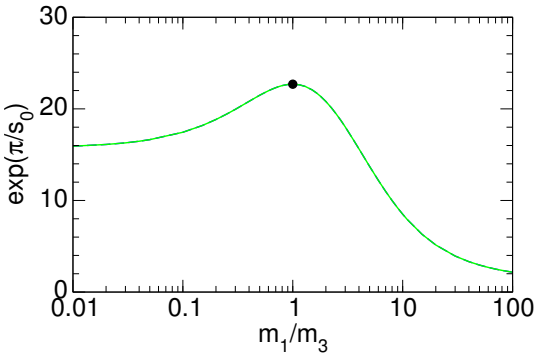

Figure 8.3.: Scaling factor as a function of the mass ratio m_1/m_3 for two equal masses m_1=m_2. The particles 1 and 2 can be identical bosons or distinguishable particles. The dot marks the point where all masses are equal. Figure taken from [53].

medium. Additionally, the appearance and properties of Cooper triples, which will be introduced in this subsection, was discussed. The dependence of the spectrum on the cutoff was not systematically investigated. A spectrum as a function of the scattering length, similar to Fig. 8.2, was also not calculated.

We begin with the discussion of the spectrum as a function of the scattering length. This is a good starting point for the comparison to the vacuum case, see Fig. 8.2 for the vacuum spectrum. In Fig. 8.4 a) the energy spectrum is depicted as a function of $1/(k_F a)$, where all three scattering lengths have the same value $a_k = a$. The mass ratio is $m_1/m_3 = 20$ and the cutoff is fixed to $\Lambda/k_F = 500$. The energy value K^* is defined as $K^* = \mathrm{sgn}(E^*)\sqrt{|E^*|}$, which is similar to the energy variable used in the vacuum spectrum in Fig. 8.2. A striking difference to the vacuum case is the appearance of poles with positive energy. In [37, 49] we reported on these positive energy poles for equal masses. Comparing these positive energy poles to the two-body results in our framework, we interpreted these poles as the equivalence to Cooper pairs in the three-body sector and referred to them as Cooper triples. The maximum energy of a Cooper triple is $k_F^2/(2\mu^{(3)})$, which is the maximal kinetic energy of three particles inside the Fermi sphere with zero total momentum. This threshold corresponds to $E_3^* = 1$ in units of the normalized energy. The energy gain of the formation of a Cooper triple is the maximum energy $E_3^* = 1$ minus the pole energy in this framework.

In the vacuum the three-body bound states vanish at the particle continuum threshold at zero energy for negative scattering lengths. In the medium the states vanish at the Cooper triple threshold $E_3^* = 1 =: E_3^{\mathrm{th}}$. This is a general result. When the scattering lengths are changed, the poles vanish at the threshold E_3^{th} for all mass ratios. For a better visualization in this instance, the vanishing points are marked with square brackets in the left graph.

In the vacuum there is another threshold at the positive scattering length side. The trimers disappear when they hit the dimer binding energy $1/(2\mu_k a^2)$. Similar to the vacuum spectrum the three-body bound state disappears in the medium at the dimer energy threshold. But in contrast to the vacuum this is not the simple in-medium dimer pole energy for zero momentum. It is a bit more complex. The in-medium threshold can be described as the two-body pole energy in the three-body system. To be more precise, it is given by the minimal pole energy of the dimer which appears in the intermediate state in the three-body scattering amplitude. In general, the threshold is determined by the pole energies of $D_k'(q = k_F, E) = D_k(E - k_F^2/(2m_k), k_F)$, which is the intermediate dimer propagator in the scattering amplitude. We see that the kinetic energy of the third particle has to be subtracted from the energy argument and due to the Fermi sphere the minimal momentum is given by k_F. However, the same effect enables the maximal three-body pole energy to be $k_F^2/(2\mu^{(3)})$, which is larger than the maximal two-body pole energy $k_F^2/(2\mu_k)$. If the dimer threshold would be simply the in-medium dimer pole energy for zero total momentum, the Cooper triple threshold $k_F^2/(2\mu^{(3)})$ could not be reached. In the vacuum the structure of the scattering amplitude is the same as in the medium. But there is no Fermi sphere. Therefore, the integration in the scattering amplitude begins at zero momentum. Hence, in the vacuum the minimal intermediate dimer pole energy coincides with the general dimer binding energy.

We turn next to the universal properties. Obviously, there does not exist an accumulation point of three-body bound states at zero energy anymore. Instead we obtain poles with positive energies. The ratio of adjacent bound states in the unitary limit approaches the value of the squared scaling factor only for deep bound states. For deep energies the effect of the Fermi sphere is reduced. Consequently, the binding energy of the in-medium bound states approaches the vacuum binding energy and the ratio of adjacent bound state energies approaches the squared scaling factor for deep energies. Next we talk about the intersection points a_* where the branches vanish at the threshold $E_3^* = 1$. The ratio of adjacent a_* is not fixed, in contrast to the vacuum case.

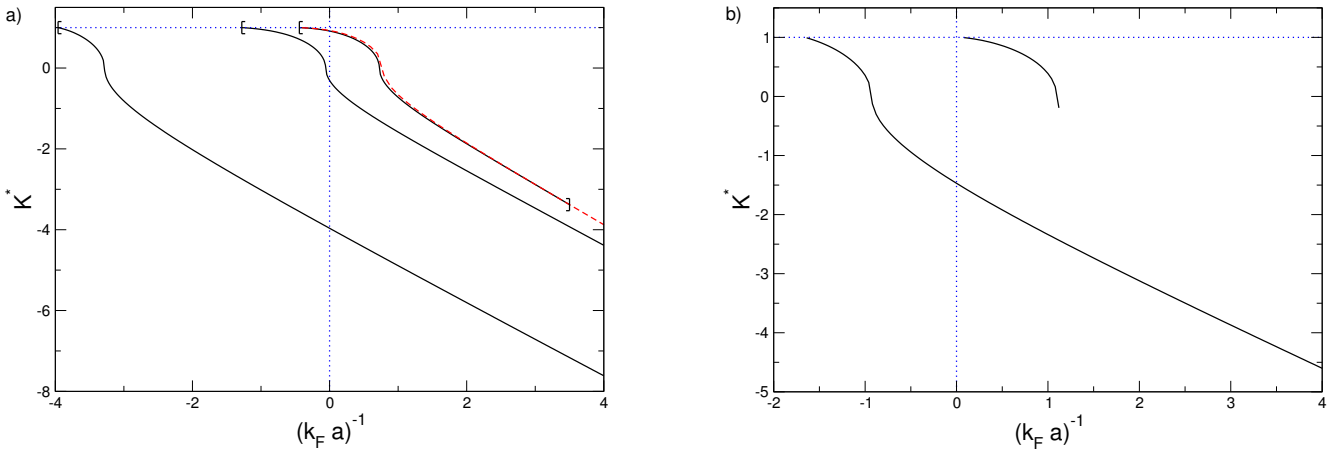

Figure 8.4.: Two spectra (black solid lines) are depicted as a function of $1/(k_F a)$, where all scattering lengths are equal. The energy variable K^* is defined by $K^* = \mathrm{sgn}(E^*)\sqrt{|E^*|}$. The blue dotted horizontal (vertical) line depicts the threshold $E_3^* = 1$ ($(k_F a)^{-1} = 0$). a) The red dashed line shows the relevant dimer threshold. For better visualization, the vanishing points are marked by square brackets in this instance. The cutoff is fixed to $\Lambda/k_F = 500$ and $m_1/m_3 = 20$. b) The parameters are $\Lambda/k_F = 250$ and $m_1/m_3 = 1$.

There is another difference related to the intersection points. In the vacuum the branches vanish at the zero energy threshold at negative scattering lengths. In general, a_* is negative in the medium, too. Consequently, the branches disappear at the threshold E_3^{th} at negative scattering lengths. However, there is an exception. For mass ratios close to one the branches first emerge at the positive scattering length side. Since the branches move to the left when the cutoff is increased, there are certain ranges of Λ/k_F where a branch vanishes at $E_3^* = 1$ at the positive scattering length side. However, the branches are rather short in this region, see Fig. 8.4 b). If the mass ratio m_i/m_j, where m_i is the largest mass and m_j is the smallest mass of the system, is larger than ≈ 3.1 the intersection points a_* are always negative. Note that this mass ratio threshold holds for both cases where the single mass is larger or smaller than the two equal masses.

Finally, we briefly discuss the shape of the branches. The course of the branches when they approach the threshold $E_3^* = 1$ is quite interesting. The form resembles a stretched inversed "S". For rather small values of $1/|k_F a|$ this form extends over a large range. If $1/|k_F a|$ becomes larger at the negative scattering length side this part of the course also becomes smaller and smaller. To detect this form of the curve in this case, one has to regard a very small interval around a_*. Otherwise it looks as if the curve goes straight towards the threshold.

Before we continue, we want to stress the restrictions of our approach. We assume three rigid Fermi spheres. This assumption can be justified in the BCS region, where Cooper pairs can be formed. However, in the positive scattering length region where dimers can be formed the physical meaning of these results is doubtful.

In summary, the spectrum is significantly altered in the medium. The most important change is the appearance of Cooper triples, which are the three-body equivalent of Cooper pairs. They vanish at the threshold $k_F^2/(2\mu^{(3)})$ when the scattering length is varied. Also the accumulation point of bound states at zero energy is not present anymore.

Comparison of the spectrum to the results of Nygaard and Zinner in Ref. [54]

In addition, we compare our spectrum to the spectrum presented in Ref. [54] by Nygaard and Zinner, where the same assumptions on the system are made. However, there is one difference. In [54] only one Fermi sea instead of three is considered and the spectrum is depicted for equal masses. To improve the comparability of the spectra, we change the normalization and the powers of the energy and scattering length on the axes in Fig. 8.5. On the horizontal axis $\mathrm{sgn}(a)/a^2$ and on the vertical axis $\mathrm{sgn}(E)|2\mu^{(3)}E|^{1/8}$ is plotted. The quantities are not normalized to the Fermi momentum, which is fixed and set to $k_F = 0.5/l_0$. The energy is, however, divided by the mass dependence. Note that the dimensions of the quantities are now powers of the free length scale l_0. The powers of the scattering length and energy on the axes are chosen consistent with [54]. Because the first three-body branch is very close to the atom-dimer threshold, we enlarged the region around $\mathrm{sgn}(a)/a^2 = 0$ in the right plot. The mass ratio is the same as in Fig. 8.4.

The spectra display significant differences. In Fig. [54] a small region could be identified, where the Fermi sea significantly modifies the spectrum. The states disappear when they reach the zero energy threshold and the lowest trimer can also vanish through the three-body continuum threshold at positive scattering lengths. Including three Fermi spheres alters the spectrum to a much larger extent. In our case the states vanish through the normalized threshold $E_3^* = 1$

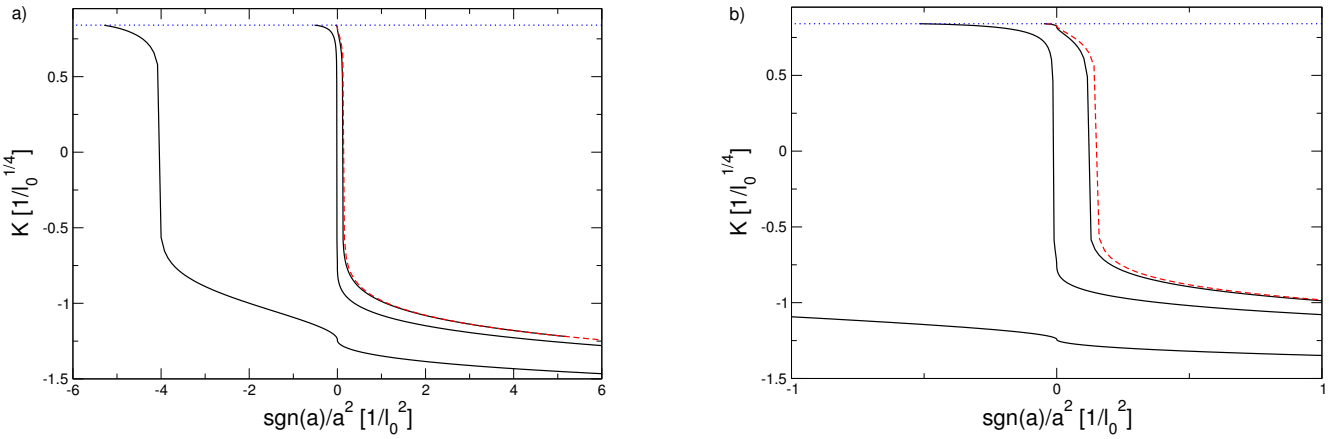

Figure 8.5.: The energy spectrum is plotted against $(\mathrm{sgn}(a)/a^2)$, where for all scattering lengths $a_k = a$ holds. The energy variable K is defined by $K = \mathrm{sgn}(E)|2\mu^{(3)}E|^{1/8}$. The cutoff is fixed to $\Lambda = 300\ l_0^{-1}$, the mass ratio is $m_1/m_3 = 20$ and the Fermi momentum is given by $k_F = 0.5/l_0$. The red dashed lines represents the relevant dimer threshold and the blue dotted line represents the threshold E_3^{th}. Graph b) focuses on a smaller interval.

instead of zero. It is therefore evident that the spectrum is modified for all scattering lengths and not only in a small region. The Cooper triples are also not present in [54]. However, this missing of Cooper triples is plausible because only one Fermi sea is included. As already mentioned, the vanishing point of the lowest state at the three-body continuum threshold can be at positive scattering lengths for mass ratios close to one. Thus, this feature remains for three Fermi seas to some extent, at least for equal masses. Indeed, the form of the atom-dimer threshold is totally different in our case as well as the form of the three-body branch near the three-body continuum threshold. The additional step of the deepest bound state close to the unitary limit seems to be caused by this kind of representation. So far we have considered the scattering length dependence of the spectrum. In the remainder of this chapter we will focus on the unitary limit.

Briefly summarized, the spectrum is significantly changed if only one Fermi sphere instead of three is considered. The main difference is that no Cooper triples are present in the case of one Fermi sphere.

Implications of the cutoff and the scaling factor

Next we discuss the dependence on the cutoff. In Fig 8.6 the spectrum is depicted as a function of the cutoff divided by the Fermi momentum Λ/k_F with a mass ratio $m_1/m_3 = 10$ in the unitary limit. Graph b) just focuses on a smaller energy region. All parameters are the same in both graphs. In Fig. 8.6 the emergence of new branches as well as the log-periodic behavior, which indicates the limit cycle, can be observed. This log-periodic behavior of the spectrum is similar to the vacuum case. When the cutoff is increased new branches of bound states appear. The distance between the branches is given by the scaling factor. The extracted scaling factor is the same as in the vacuum. This seems to be a general result which we could confirm for different mass ratios.

Note that the poles do not emerge at the threshold E_3^{th} in the right graph, but rather at a slightly smaller energy. This behavior in the unitary limit is related to the above mentioned behavior of the intersection points. If the energy threshold in the unitary limit is smaller than one, the intersection points a_* are always negative. Recall that the branches always vanish at the threshold $E_3^* = 1$ and move to the left in Fig. 8.4 when the normalized cutoff is increased. Thus, if the maximum energy value at the point $1/(k_F a) = 0$ is smaller than one, a_* can not cross the point $1/(k_F a) = 0$ and thus a_* is always negative. Since we found that the intersection points can only be positive if the mass ratio is smaller than ≈ 3.1, the maximal energy threshold in the unitary limit equals E_3^{th} only when the mass ratio is smaller than ≈ 3.1.

Since the scaling factors are the same as in the vacuum, Fig. 8.3 is an important reference point for our considerations. A crucial fact is that the curve of the scaling factor as a function of the mass ratio is not symmetric. Whereas the scaling factor approaches the value 15.7 on one side, it approaches the value 1 on the other side. This implies that the states can become arbitrarily close to each other.

The implications of this behavior are further demonstrated in Fig. 8.7. In this graph the spectrum of the poles is depicted as a function of the mass ratio. The energy variable is switched to $|E_3^* - 1|$ in order for a logarithmic representation to be applicable. The cutoff is fixed at $\Lambda/k_F = 500$ and the scattering lengths are in the unitary limit. We observe a different behavior depending if the mass ratio is smaller or larger than one. At a mass ratio of one there are two poles present. But with increasing mass ratio we obtain more and more branches. Since the quotient Λ/k_F is fixed, the emergence of new branches is exclusively caused by the changed mass ratio. This can be explained as follows. When

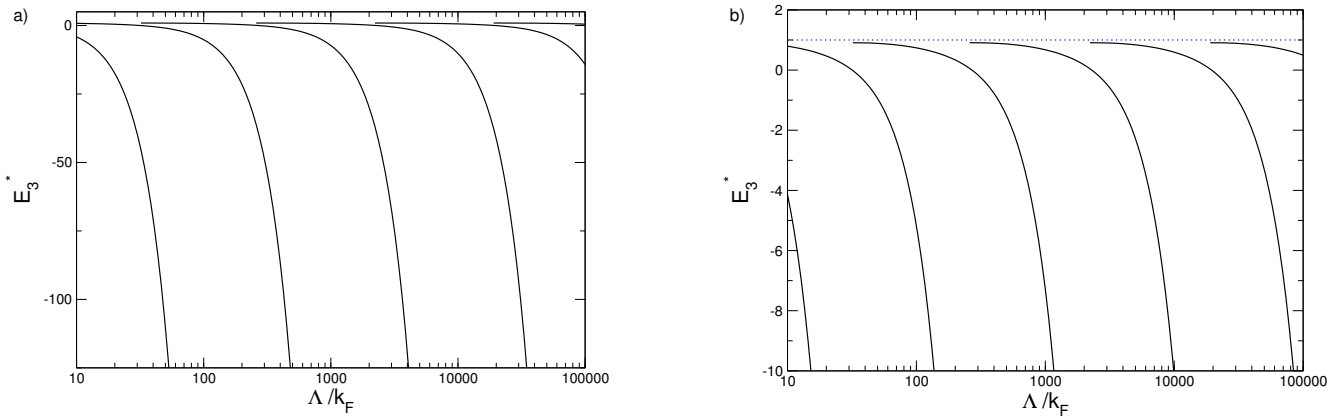

Figure 8.6.: Spectrum of the three-body states depicted as a function of Λ/k_F for a mass ratio of $m_1/m_3 = 10$. The energy is normalized according to $E_3^* = 2\mu^{(3)}E/k_F^2$. The scattering lengths are in the unitary limit $1/a_k = 0$. Graph b) focuses on a smaller energy range. The horizontal dotted line represents the threshold $E_3^* = 1$.

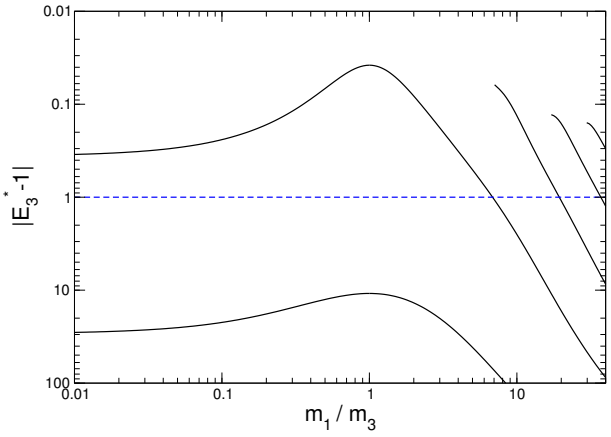

Figure 8.7.: In this graph the three-body spectrum is depicted as a function of the mass ratio m_1/m_3. The cutoff is fixed to $\Lambda/k_F = 500$ and the scattering lengths are in the unitary limit. The blue horizontal line depicts the threshold $|E_3^* - 1| = 1$, which corresponds to $E_3^* = 0$ and distinguishes negative and positive energy poles.

the cutoff is increased by the scaling factor, a new branch appears. Since the scaling factor is significantly smaller for larger mass ratios, more branches appeared up to this chosen cutoff of $\Lambda/k_F = 500$ for larger mass ratios. Although, the ratio of adjacent bound state energies approaches the scaling relation for large negative energies, we observe that the states become more dense in the depicted energy region. For example, we observe the simultaneous existence of two Cooper triple states. Note that the positive energy region is represented by energies smaller than one in this graph. It is also possible to obtain more simultaneous Cooper triple states in the spectrum. Additionally, the above mentioned appearance of branches at smaller energies with increasing mass ratio in the unitary limit can be observed.

For mass ratios m_1/m_3 smaller than one we observe a different behavior. For these ratios the scaling factor is only slightly reduced and approaches a fixed value, see Fig 8.3. Correspondingly, we also varied the mass ratio down to $m_1/m_3 = 0.01$. In contrast to the other side the number of branches remains constant. It is also obvious that the branches approach a fixed value. This holds for the bound state as well as the Cooper triple state. Hence, this behavior is understandable by considering the scaling factor.

We recap the most important results: The spectrum is a log-periodic function of the normalized cutoff and the scaling factor is the same as in the vacuum. Therefore, when the spectrum is considered as a function of the mass ratio, we observe a different behavior for the two cases $m_1/m_3 < 1$ and $m_1/m_3 > 1$.

Considerations concerning the phase structure

Until now, we have discussed general results of the pole structure in the medium. Next we will turn to the implications for the phase structure. Of particular interest are mixtures of ultracold Fermi gases, which serve also as a test field

for theoretical approaches. These mixtures range from atoms in different hyperfine states up to mixtures of different elements. The pairing properties and phase structures in the BCS region are thereby aspects of special attention. However, three-body physics can become important in these systems. An example is the formation of three-body bound states, which results in an instable system. Due to large binding energies and the related release of kinetic energy, it is possible that particles can escape the trap in an experiment. This can lead to high loss rates and may empty the trap.

We apply our framework regarding the question how three-body physics can alter the phase structure. Although our approach in the medium is of qualitative nature, we expect our framework to give insights concerning this question for systems with three distinguishable particle species and two different masses in the negative scattering length region. Recall that we already discussed this in the two-body chapter.

We start with the discussion of three-body bound states. In the vacuum there do not exist two-body bound states if the scattering length is negative. As opposed to this three-body bound states can in principle occur in every region. There is no domain of scattering lengths in the vacuum where bound states are generally forbidden[1]. In the medium we have seen that there exist three-body bound states as well as Cooper triples. In this context we want to repeat the EFT boundaries. The applied effective field theory describes low-energy observables in a given system. For large momenta or high energies the theory breaks down. Therefore, deep bound states in our framework have to be regarded as unphysical predictions. A sharp criterion which bound state is to be considered as deep and therefore as unphysical can not be given. In general, it depends on the physical system and the associated scales where the effective theory breaks down, e.g. the van der Waals length in atomic gases. If the energies approach these scales the theory certainly breaks down. Hence, in the remainder of this section we focus on more general results concerning the phase structure. However, for a given system, where the required quantities are known, more explicit results can be calculated.

Next we discuss the role of the Cooper triples. Consider a physical system to be located in a region, where Cooper triples but no bound states can be formed. If the energy gain for the Cooper pairs is larger than the energy gain for the Cooper triples, we expect the Cooper pairs to build a condensate. The situation where the energy gain of Cooper triples is larger is more complicated. Since a Cooper triple is a fermion in contrast to a Cooper pair, it can not condense in a simple manner. It is an open question if a Cooper pair condensate is still formed. However, we assume that the three-body physics of Cooper triples plays an important role in this case.

In order to detect regions of Cooper pair and Cooper triple physics we should therefore identify the regions in our framework where Cooper triples are present and the remaining bound states exhibit deep binding energies.

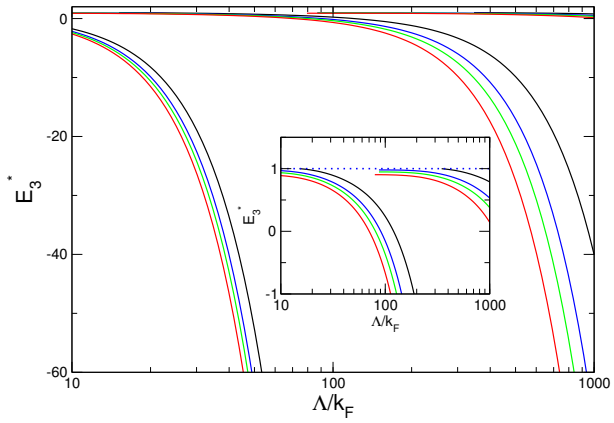

Figure 8.8.: The energy spectrum is shown as a function of Λ/k_F for selected mass ratios of m_1/m_3=1 (black), m_1/m_3=1/5 (blue), m_1/m_3=1/10 (green) and m_1/m_3=1/100 (red). The scattering lengths are in the unitary limit and the inset zooms in on the energy region from -1 to 1. The horizontal dotted line shows the energy threshold E_3^{th}. The energy E_3^* is defined as $E_3^* = E \cdot 2\mu^{(3)}/k_F^2$, where E is the pole energy.

We will now regard the energy spectrum as a function of Λ/k_F for different mass ratios in the unitary limit. In Fig. 8.8 the spectrum is depicted for four different mass ratios $m_1/m_3 = 1,\ 1/5,\ 1/10$ and $1/100$. Note that we have reduced the presented range of Λ/k_F because the spectra are log-periodic. The graph as well as the inset clearly demonstrate that there exist distinct bands, where the states are located. Keep in mind that for a mass ratio of $m_1/m_3 = 1/100$ the scaling factor is already close to the limit value. Hence, the depicted bands basically cover the entire area, where the poles appear, if the mass ratio is smaller than one. One can clearly identify regions where a state with positive energy and a deep bound state is present. In order to obtain measurable results, a three-body observable has to be matched to its physical value in the considered system. This procedure determines the cutoff. However, the Fermi momentum, which corresponds to the density, is in principle a tunable quantity. Neglecting experimental limitations, it should be possible to

[1] Note that there are certain limitations for the appearance of the Efimov effect for identical fermions.

shift the system horizontally to a desired point in the presented spectra by adjusting the Fermi momentum. Hence, from this graph density ranges can in principle be extracted, where the physics of Cooper pairs and Cooper triples should be dominant. In this case the range is to a large extent insensitive to the mass ratio.

In Fig. 8.9 we compare the energy gain of the Cooper triples to the energy gain of the Cooper pairs with zero total momentum for one of the previously selected mass ratios, $m_1/m_3 = 1/5$. Since in this three-body system three different Cooper pairs can be formed, we choose the Cooper pair with the largest energy gain. The energy gain of a Cooper triple is defined by $\Delta E = k_F^2/(2\mu^{(3)}) - E$ and for Cooper pairs $\Delta E = k_F^2/(2\mu_k) - E$, where E is the pole energy. We observe regions where the energy gain of Cooper triples is larger as well as regions where the Cooper pairs are energetically favorable.

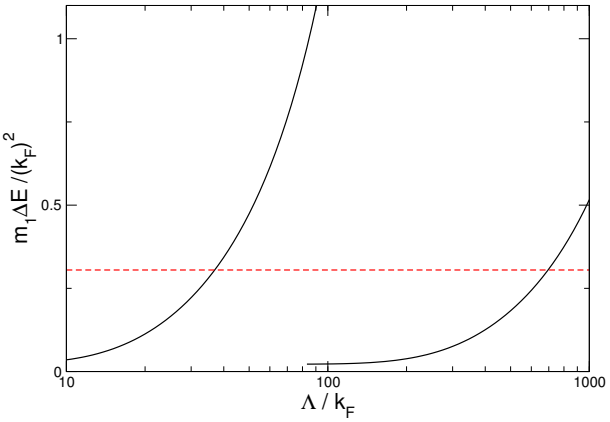

Figure 8.9.: The energy gain of Cooper triples (black solid line) and Cooper pairs (red dashed line) is compared in dependence on Λ/k_F for the mass ratio of $m_1/m_3 = 1/5$ in the unitary limit. The Cooper pair with zero total momentum and the largest energy gain in this system is chosen. For the three-body poles the energy gain is given by $\Delta E = k_F^2/(2\mu^{(3)}) - E$ and for the two body poles by $\Delta E = k_F^2/(2\mu_k) - E$, where E is the pole energy. The energy gain is only depicted for three-body poles with positive energy.

We move on to the case where the mass ratio m_1/m_3 is larger than one. In Fig. 8.10 the spectrum is depicted for the mass ratios $m_1/m_3 = 1$, 5, 10 and 20. The distinct band structure is gone and a more complex behavior shows up. This behavior is related to the rapid change of the scaling factor with the mass ratio. The order of the branch appearance for different masses is not given anymore. Due to the smaller scaling factor the branches of poles with large mass ratio appear more frequent than branches with small mass ratios. This destroys the well arranged band structure. As a result, the spectrum is very sensitive to the mass ratio.

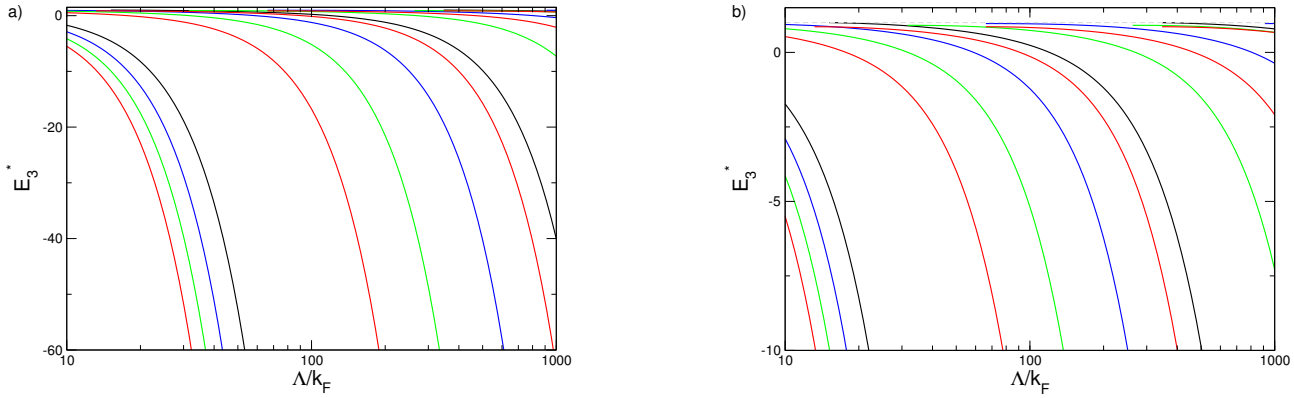

Figure 8.10.: The energy spectrum depicted as a function of Λ/k_F for chosen mass ratios of m_1/m_3=1 (black), m_1/m_3=5 (blue), m_1/m_3=10 (green) and m_1/m_3=20 (red). The scattering lengths are $1/a_k = 0$ and graph b) shows a smaller energy interval.

We focus for a moment on the red branches with the mass ratio of $m_1/m_3 = 20$. It is difficult to find a configuration of Cooper triples and deep bound states. From this we infer that smaller mass ratios should be preferred in order to avoid the appearance of bound states in this case. Due to the sensitivity on the mass ratio, general results can not be given for this case with $m_1 > m_3$.

In Fig. 8.11 we have exemplary plotted the regions of bound states as well as the regions of Cooper pairs and Cooper triples in the unitary limit. We considered the deep binding energy threshold E_l (imposed by the van der Waals length)

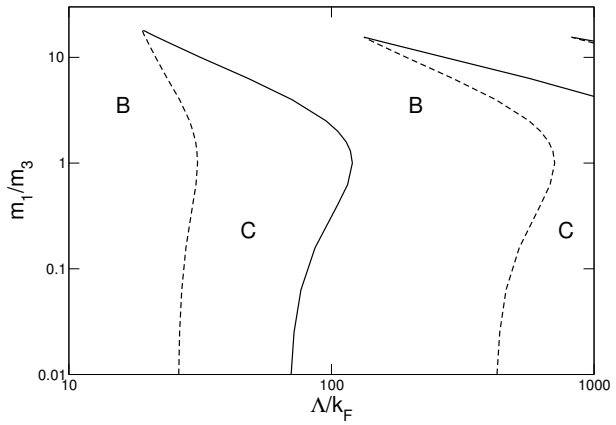

Figure 8.11.: In this graph the regions of bound states as well as Cooper pairs and triples are depicted in the plane of the normalized cutoff and the mass ratio m_1/m_3. The region where bound states exist is marked with the letter "B". In contrast, the region where Cooper pairs and triples but no bound states are present is marked with the letter "C". In this graph bound states with a binding energy larger than $E_l = 20 \cdot k_F^2/(2\mu^{(3)})$ are considered to be unphysical. The dashed line corresponds to the E_l threshold and the solid line to the zero energy threshold. The scattering lengths are in the unitary limit. Also note that this graph is of qualitative nature.

to be $E_l = 20 \cdot k_F^2/(2\mu^{(3)})$ and then determined the regions where bound states exist in the plane of the normalized cutoff and the mass ratio. To be more precise, we considered all bound states with a binding energy larger than $|E_3^*| = 20$ to be unphysical. Hence, all poles with an energy between 0 and $-E_l$ are regarded as bound states. The chosen value of E_l is of course only an example. The region where bound states exist is marked by the letter "B" in Fig. 8.11. As discussed above, in this region the Fermi gas is considered to be unstable due to the formation of bound states. The region where Cooper triples and Cooper pairs but no bound states are present is marked by the letter "C". In the remainder of this chapter we will denote this region as Cooper triple region. In this region we expect the phase structure to be determined by Cooper pair and Cooper triple physics.
Before we proceed with the discussion, we want to stress that the graph is of qualitative nature. The values of the graph were extracted from the energy spectra as a function of the normalized cutoff for different mass ratios, like the spectra in Fig. 8.8 or Fig. 8.10.

For small mass ratios we again observe that the Cooper triple regions are to a large extent insensitive to the ratio m_1/m_3 in Fig. 8.11. When the mass ratio becomes considerably larger than one, the Cooper triple regions become smaller until finally the regions disappear for large mass ratios. In this case there are always bound states present. Note that if a different van der Waals length (and the corresponding energy threshold E_l) is considered, only the dashed line is changed since this line corresponds to the threshold E_l. The solid line corresponds to the threshold of zero energy. When a different E_l is considered, the solid line of course becomes shorter or longer due to the changed intersection point.

At the end of this chapter we summarize the results related to the phase structure. We can find regions of bound states as well as regions of Cooper pairs and triples. In the bound state region we expect the Fermi gas to be unstable due to the formation of bound states. In contrast, in the Cooper triple region Cooper pairs and Cooper triples but no physical bound states are present. Therefore, we expect the phase structure to be determined by the formation of Cooper triples and Cooper pairs in this region. We found that the energy gain of forming Cooper triples can be larger or smaller than the energy gain of forming Cooper pairs. It is, however, an open question how Cooper triples affect the phase structure. In general, it is more likely to find Cooper triple regions for small mass ratios m_1/m_3 than for large ones. For large mass ratios there can be no Cooper triple region at all.

9 Summary and Outlook

In this thesis we investigated *Limit Cycles in Quantum Systems*. Limit cycles are an RG topology. When degrees of freedom are integrated out, the coupling constant flows periodically in a closed curve. The presence of limit cycles is restricted by the necessary condition of discrete scale invariance. A signature of discrete scale invariance and limit cycles is log-periodic behavior.

The first part of this thesis, *Limit Cycles and SRG*, was concerned with the search for signatures of limit cycles in SRG evolved potentials. We examined two different systems, which exhibit the limit cycle. The $1/R^2$ potential in a two-body system as well as a three-body system with a separable two-body interaction and large scattering lengths were considered. We applied the kinetic energy, the exponential and the inverse generator in the SRG evolution of the $1/R^2$ potential. For all generators we observed the emerging and vanishing of structures in the potential plots, which suggest the appearance of a limit cycle. However, we were not able to extract a signal of the limit cycle when the T generator was employed. Using the exponential or inverse generator, a signature of the limit cycle could be detected. In the diagonal elements of the evolved potential $V(p, p, \lambda)$ we found oscillations for momenta p close to the generator parameter σ. The number of observable oscillations depends strongly on the parameter σ. Small values of σ have to be chosen in order to see a larger number of oscillations. These oscillations are not completely regular. However, it is possible to state an interval of the periods which is in agreement with the periods of the limit cycle in the RG approach. In particular, this holds for larger values of the potential parameter ν so that a sufficient number of oscillations can be observed.

In the three-body system we considered two different cases. In the first case we neglected the induced three-body potentials and in the second case we included them. If the three-body potentials are neglected, the transformation is no longer unitary and thus the three-body binding energies change during the flow. We detected loops when the binding energies were plotted against each other during the evolution if the exponential and inverse generators were applied. For the T generator these loops were not observed.

In the second case where induced three-body potentials were included, we were not able to detect signals of the limit cycle. We assume that we have to evolve to larger values of the flow parameter s. However, there are two principal obstacles which prevented us from evolving further. The problems are the computational runtime and the deviation of the binding energies from the initial values. We suppose numerical errors and in particular the interpolations to be the reason for the large deviations of the binding energies.

Though we could extract a signal of the limit cycle for the $1/R^2$ potential if the inverse or exponential generator were employed, there are still open questions and further studies are needed. It is especially puzzling why we could not extract a signature for the T generator, although the plots of the evolved potential indicate the presence of the limit cycle. Perhaps an alternative extraction method leads to success or there is some fundamental obstacle, which prevents us from detecting the signal. In this context it would be useful to know the reason for the observation of the oscillations, when the exponential and inverse generator are applied. Up to now we can only make an educated guess. This knowledge may also lead to the extraction of a more precise signal. The application of a generator which is particularly tailored to this problem may also result in an improvement of the extraction of limit cycle signals. Nevertheless, a better insight into limit cycles and SRG is needed for this approach.

We consider detecting signatures of the limit cycle in the examined three-body system to be difficult. This assessment is mainly based on the aforementioned reasons. One option to avoid the problem of the limited evolution range could be to consider a slightly different system. The scaling factor in this system depends on the mass ratios. Therefore, by tuning the mass ratios in a bosonic system with large scattering length the scaling factor can be decreased to a desired value. Perhaps several cycles are then completed at the maximal evolution point and it would be possible to detect a signature of the limit cycle. An alternative approach could be to find and employ a different basis, which avoids some of the numerical problems. A hyperspherical momentum representation is for example used in [55]. However, our assumption that in principle it should be easier to detect the limit cycle in the three-body system than in the examined two-body system if numerical problems are not present, could turn out wrong.

In the second part of this thesis, *Limit Cycles at Finite Density*, we examined the pole structure of the scattering amplitude of distinguishable fermions with unequal masses in presence of a Fermi sea for each fermion species at zero temperature. We focused on the region with negative scattering lengths and on the unitary limit. In the two-body system we compared two different cases. In the first case we assumed a Fermi sphere, which is filled up to the Fermi momentum k_F, without the implementation of holes. In the second case we relaxed the restriction of a rigid Fermi sea by including hole propagation. We found that the first case is better suited to describe this system. This becomes apparent when the poles are considered as a function of the total momentum of the pair. When the mass ratio exceeds a certain value, we

found the energy minimum to be located at a nonzero total momentum if hole propagation is included. This implies a preferred nonzero momentum of the Cooper pairs. Hence, the corresponding phase is no longer a standard BCS phase, which contradicts the results of [50].

Therefore, we considered only the first case in the three-body system, where the limit cycle occurs in the vacuum for large scattering lengths. Of special interest were the general properties of the spectrum as well as properties related to the phase structure of a three-component Fermi gas. The three-body spectrum is considerably modified by the medium. For example, the accumulation point of three-body bound states at zero energy for the unitary limit is not present anymore. The most obvious change is that the poles do not vanish at zero energy. Instead they disappear at the threshold $k_F^2/(2\mu^{(3)})$ when the spectrum is regarded as a function of the scattering length. We found that the states with positive energy, referred to as Cooper triples, are generalized in systems with unequal masses as expected.

Furthermore, we examined the dependence of the spectrum on the cutoff Λ, which plays the role of a three-body force. When the energies and momenta are normalized to the Fermi momentum, we observed a log-periodic dependence of the spectrum on Λ/k_F in the unitary limit. We found that the scaling factors remain the same in the medium. The conserved scaling factors have implications on the spectrum. For the case of two equal masses $m_1 = m_2$ and one different mass m_3 in the unitary limit, we found that the spectrum is rather insensitive to the mass ratio if the mass ratios are small with $m_1/m_3 < 1$. In contrast, for mass ratios $m_1/m_3 > 1$ we observed a strong dependence of the spectrum on the mass ratio and the appearance of more pole branches due to the significantly reduced scaling factor.

Turning to the implications on the phase structure in the unitary limit, we were able to find regions in the spectrum where only deep bound states and Cooper triples are present. In these regions it is most likely to observe Cooper pair and Cooper triple physics since deep bound states have to be considered unphysical in our framework. Additionally, we compared the energy gain of Cooper pairs and Cooper triples. We found that the energy gain of the Cooper pair as well as the Cooper triple can be larger.

In future work a more physical scenario of the interaction of the fermions and the Fermi sphere should be considered. Since we only incorporated the Pauli blocking so far, it is interesting how our findings are altered in a more realistic scenario. In the two-body system we saw that including only hole propagation in the considered Feynman diagram did not lead to success. Hence, more Feynman diagrams with included hole propagation should be incorporated. Which of these diagrams are most relevant and should be summed up is an interesting question. Astonishing in this context is that the simple approximation regarding the Fermi sea and the kinetic energy in [43] yields such good results. It would be advantageous if this approximation could be related to a set of Feynman diagrams.

An open question is how the Cooper triples affect the phase structure. As already mentioned, we found regions where the energy gain of the Cooper triples is larger than the Cooper pairs. Since the Cooper triples are fermions, they can not condense in a simple manner. However, a Fermi gas of Cooper triples could be formed. Therefore, it is important that three-body physics of Cooper triples is considered in phase structure calculations in three-component Fermi gases. Such calculations could shed light on the question how the phase structure is influenced by Cooper triples. Possible candidates are Monte-Carlo simulations as well as mean-field approaches.

Certainly, the experimental study of the Cooper triple influence on the phase structure in three-component Fermi gases with different spin states or different masses would be desirable. In ^{6}Li, for example, mixtures of three hyperfine states have been realized [56–59]. Also mixtures consisting of two different atoms like ^{6}Li and ^{40}K [60–62] are experimentally accessible.

A Permutation Operator

For the SRG evolution as well as the Faddeev equations we require the matrix elements of the permutation operators, defined in chapter 5.1.2. In this chapter we state the matrix element of the permutation operator P in the partial wave basis

$$\langle pq\alpha|P|p'q'\alpha'\rangle = \langle pq\alpha|P_{12}P_{23} + P_{13}P_{23}|p'q'\alpha'\rangle \,. \tag{A.1}$$

Note that in the case of nonzero spins the spin coupling has also to be considered. We have already proven the relation

$$\langle pq\alpha|P_{12}P_{23}|p'q'\alpha'\rangle = \langle pq\alpha|P_{13}P_{23}|p'q'\alpha'\rangle \,. \tag{A.2}$$

Thus, it is sufficient to calculate the matrix element $\langle pq\alpha|P_{12}P_{23}|p'q'\alpha'\rangle$. The matrix element of P is then simply $\langle pq\alpha|P|p'q'\alpha'\rangle = 2\langle pq\alpha|P_{12}P_{23}|p'q'\alpha'\rangle$. We define X_{12} to be

$$X_{12} = {}_1\langle pq\,(lj)LM|p'q'\,(l'j')L'M'\rangle_2 = {}_1\langle pq\,(lj)LM|P_{12}P_{23}|p'q'\,(l'j')L'M'\rangle_1. \tag{A.3}$$

The calculation of this matrix element is presented in [30]. The result is given by

$$\begin{aligned} X_{12} = \delta_{LL'}\delta_{MM'} \sum_k g_k \sum_{l_1+l_2=l} \sum_{l_1'+l_2'=l'} q^{l_2+l_2'}\,(q')^{l_1+l_1'}(-1)^{l'}\sqrt{[l][j][l'][j']}\;[k](\tfrac{1}{2})^{l_2+l_1'+1} \\ \sqrt{\frac{(2l+1)!}{(2l_1)!(2l_2)!}}\sqrt{\frac{(2l'+1)!}{(2l_1')!(2l_2')!}} \sum_{ff'} \begin{Bmatrix} l_1 & l_2 & l \\ j & L & f \end{Bmatrix} \begin{bmatrix} l_2 & j & f \\ 0 & 0 & 0 \end{bmatrix} \begin{Bmatrix} l_2' & l_1' & l' \\ j' & L & f' \end{Bmatrix} \begin{bmatrix} l_1' & j' & f' \\ 0 & 0 & 0 \end{bmatrix} \begin{Bmatrix} f & l_1 & L \\ f' & l_2' & k \end{Bmatrix} \\ \begin{bmatrix} k & l_1 & f' \\ 0 & 0 & 0 \end{bmatrix} \begin{bmatrix} k & l_2' & f \\ 0 & 0 & 0 \end{bmatrix} \end{aligned} \tag{A.4}$$

with

$$g_k = \int_{-1}^{1} dx\, P_k(x) \frac{\delta(p - \sqrt{\frac{1}{4}q^2 + q'^2 + qq'x}}{p^{l+2}} \frac{\delta(p' - \sqrt{\frac{1}{4}q'^2 + q^2 + qq'x})}{(p')^{l'+2}} \,. \tag{A.5}$$

In this formula and in the following some angular momentum related functions are used, which are

- $\begin{bmatrix} l_1 & l_2 & l \\ m_1 & m_2 & m \end{bmatrix} = \langle l_1\, l_2\, l\, m|l_1\, l_2\, m_1\, m_2\rangle =$ Clebsch-Gordan coefficient where l_1 and l_2 couple to l.
- $\begin{Bmatrix} j_1 & j_2 & j_3 \\ j_4 & j_5 & j_6 \end{Bmatrix} =$ Wigner's $6j$ symbol
- $\begin{Bmatrix} l_1 & j_1 & f_1 \\ l_2 & j_2 & f_2 \\ l & j & L \end{Bmatrix} =$ Wigner's $9j$ symbol
- $P_l(x) =$ Legendre polynomial
- $[l] = (2l+1)$,

where the definition of the notation of the Clebsch-Gordan coefficient can be found in [63] and of the Wigner symbols in [64]. Additionally, we define the following functions

$$\begin{aligned} \tilde{\pi}_1(q,q',x) &= \sqrt{\tfrac{1}{4}q^2 + q'^2 + qq'x} \\ \tilde{\pi}_2(q,q',x) &= \sqrt{\tfrac{1}{4}q'^2 + q^2 + qq'x} \\ \pi_1(p',q',x) &= \sqrt{\tfrac{1}{4}p'^2 + \tfrac{3}{4}p'q'x + \tfrac{9}{16}q'^2} \\ \pi_2(p',q',x) &= \sqrt{p'^2 - p'q'x + \tfrac{1}{4}q'^2} \,. \end{aligned} \tag{A.6}$$

Thus, g_k can be written as follows

$$g_k = \int_{-1}^{1} dx\, P_k(x) \frac{\delta(p - \tilde{\pi}_1(q,q',x))}{p^{l+2}} \frac{\delta(p' - \tilde{\pi}_2(q,q',x))}{(p')^{l'+2}} \,. \tag{A.7}$$

The delta functions act on the momentum variables p and p'. For the SRG equations we also require an expression of this matrix element where the delta functions act on p and q. This expression can be written as

$$\begin{aligned} X_{12} = \delta_{LL'}\delta_{MM'}(-1)^l \sum_{l_1+l_2=l} \left(\tfrac{1}{2}p'\right)^{l_1} \left(\tfrac{3}{4}q'\right)^{l_2} \sqrt{\frac{4\pi[l]!}{[l_1]![l_2]!}} \sum_{j_1+j_2=j} (p')^{j_1} \left(\tfrac{1}{2}q'\right)^{j_2} \\ \sqrt{\frac{4\pi[j]!}{[j_1]![j_2]!}}(-1)^{j_2} \sum_{f_1,f_2} \frac{1}{4\pi} \sqrt{[l_1][l_2][j_1][j_2][l][j]} \begin{bmatrix} l_1 & j_1 & f_1 \\ 0 & 0 & 0 \end{bmatrix} \begin{bmatrix} l_2 & j_2 & f_2 \\ 0 & 0 & 0 \end{bmatrix} \begin{Bmatrix} l_1 & j_1 & f_1 \\ l_2 & j_2 & f_2 \\ l & j & L \end{Bmatrix} \\ \sum_k 2\pi[k](-1)^k \overline{g_k} \frac{\sqrt{[l'][j']}}{4\pi} \begin{bmatrix} k & l' & f_1 \\ 0 & 0 & 0 \end{bmatrix} \begin{bmatrix} k & j' & f_2 \\ 0 & 0 & 0 \end{bmatrix} (-1)^{j'+f_1+k+L} \begin{Bmatrix} f_2 & j' & k \\ l' & f_1 & L \end{Bmatrix} , \end{aligned} \tag{A.8}$$

with

$$\begin{aligned} \overline{g_k} &= \int_{-1}^{1} dx\, P_k(x) \frac{\delta\left(p - \sqrt{\frac{1}{4}p'^2 + \frac{3}{4}p'q'x + \frac{9}{16}q'^2}\right)}{p^{l+2}} \frac{\delta\left(q - \sqrt{p'^2 - p'q'x + \frac{1}{4}q'^2}\right)}{q^{j+2}} \\ &= \int_{-1}^{1} dx\, P_k(x) \frac{\delta\left(p - \pi_1(p',q',x)\right)}{p^{l+2}} \frac{\delta\left(q - \pi_2(p',q',x)\right)}{q^{j+2}} \,. \end{aligned} \tag{A.9}$$

The matrix elements X_{12} are calculated for arbitrary angular momentum variables. In this thesis we consider simple conditions for the angular momentum variables. The total angular momentum L of the spinless bosonic system is set to zero and we take only S-wave two-body potentials into consideration. Due to the bosonic nature of the system l and l' are even. For these conditions we determined X_{12} to be

$$\begin{aligned} \langle pq\,(00)L=0|P_{12}P_{23}|p'q'\,(l'j')L'=0\rangle &= \tfrac{1}{2}\sqrt{[l']}\,\delta_{l'j'}\,\overline{g_{l'}} \\ &= \tfrac{1}{2}\sqrt{[l']}\delta_{l'j'} \int_{-1}^{1} dx\, P_{l'}(x) \frac{\delta(p - \pi_1(p',q',x))\delta(q - \pi_2(p',q',x))}{p^2q^2} \,. \end{aligned} \tag{A.10}$$

For the different form of X_{12} we found

$$\langle pq\,(00)L=0|P_{12}P_{23}|p'q'\,(l'j')L'=0\rangle = \delta_{l'j'} \int_{-1}^{1} dx\, b_{l'}(q,q',p',x) \frac{\delta(p - \tilde{\pi}_1(q,q',x))\delta(p' - \tilde{\pi}_2(q,q',x))}{p^2p'^2} \,, \tag{A.11}$$

with

$$b_{l'}(q,q',p',x) = \frac{1}{(p')^{l'}} \sum_{l'_1+l'_2=l'} P_{l'_2}(x)(q)^{l'_2}(q')^{l'_1}(\tfrac{1}{2})^{l'_1+1} \sqrt{\frac{(2l'+1)!}{(2l'_1)!(2l'_2)!}}(-1)^{l'_2} \begin{bmatrix} l'_1 & l' & l'_2 \\ 0 & 0 & 0 \end{bmatrix} \sqrt{\frac{[l']}{[l'_2]}} \,. \tag{A.12}$$

For angular momenta up to $l' = 6$ we state the function

$$\begin{aligned} b_0(q,q',p',x) &= \tfrac{1}{2} \\ b_2(q,q',p',x) &= \tfrac{1}{p'^2}\left(\tfrac{1}{2}\sqrt{5}q^2P_2(x) + \tfrac{1}{2}\sqrt{5}qq'P_1(x) + (q')^2\tfrac{1}{8}\sqrt{5}P_0(x)\right) \\ b_4(q,q',p',x) &= \tfrac{1}{p'^4}\left(\tfrac{3}{2}P_4(x)q^4 + 3P_3(x)q^3q' + \tfrac{9}{4}P_2(x)q^2(q')^2 + \tfrac{3}{4}P_1(x)q(q')^3 + \tfrac{3}{32}P_0(x)(q')^4\right) \\ b_6(q,q',p',x) &= \tfrac{1}{p'^6}\sqrt{13}\left(\tfrac{1}{2}P_6(x)q^6 + \tfrac{3}{2}P_5(x)q^5q' + \tfrac{15}{8}P_4(x)q^4(q')^2 + \tfrac{5}{4}P_3(x)q^3(q')^3 + \right. \\ &\quad \left. + \tfrac{15}{32}P_2(x)q^2(q')^4 + \tfrac{3}{32}P_1(x)q(q')^5 + (\tfrac{1}{2})^7(q')^6P_0(x)\right) \,. \end{aligned} \tag{A.13}$$

For the calculation of (A.10) and (A.11) the following relations [64] were used.
Clebsch-Gordan coefficients:

$$\begin{bmatrix} a & b & 0 \\ \alpha & \beta & 0 \end{bmatrix} = (-1)^{a-\alpha} \frac{\delta_{ab}\delta_{\alpha,-\beta}}{\sqrt{[a]}}$$
$$\begin{bmatrix} a & 0 & c \\ \alpha & 0 & \gamma \end{bmatrix} = \delta_{ac}\delta_{\alpha\gamma} \tag{A.14}$$

6j-Symbols:

$$\begin{Bmatrix} 0 & b & c \\ d & e & f \end{Bmatrix} = (-1)^{b+e+d} \frac{\delta_{bc}\delta_{ef}}{\sqrt{[b][e]}}$$
$$\begin{Bmatrix} a & 0 & c \\ d & e & f \end{Bmatrix} = (-1)^{a+d+e} \frac{\delta_{ac}\delta_{df}}{\sqrt{[a][d]}}$$
$$\begin{Bmatrix} a & b & c \\ d & 0 & f \end{Bmatrix} = (-1)^{a+b+d} \frac{\delta_{af}\delta_{cd}}{\sqrt{[a][c]}} \tag{A.15}$$

9j-symbols :

$$\begin{Bmatrix} a & b & c \\ d & e & f \\ 0 & 0 & 0 \end{Bmatrix} = \frac{\delta_{ad}\delta_{be}\delta_{cf}}{\sqrt{[a][b][c]}} \tag{A.16}$$

$$\begin{Bmatrix} a & b & c \\ d & e & f \\ g & h & 0 \end{Bmatrix} = \delta_{cf}\delta_{gh} \frac{(-1)^{b+c+d+g}}{\sqrt{[c][g]}} \begin{Bmatrix} a & b & c \\ e & d & g \end{Bmatrix} \tag{A.17}$$

B Faddeev Equations

The Faddeev equations can be used to calculate three-body binding energies. In the Faddeev equations the three-body wave function is decomposed into Faddeev components in order to avoid disconnected contributions. Derivations of the Faddeev equations can e.g. be found in [30, 32, 35], where we mainly follow the derivation in [32]. The starting point is the Schrödinger equation in the three-body system. It can be rewritten into

$$|\Psi\rangle = \frac{1}{E - H_0}\left(\sum_{i=1}^{3} V_2^{(i)} + V_3\right)|\Psi\rangle = G_0\left(\sum_{i=1}^{3} V_2^{(i)} + V_3\right)|\Psi\rangle\,, \tag{B.1}$$

with the two-body potentials $V_2^{(i)}$, the three-body potential V_3, the kinetic energy H_0 and the resolvent $G_0 = (E - H_0)^{-1}$. We now define the Faddeev components by

$$\begin{aligned} |\psi_2^{(i)}\rangle &= G_0 V_2^{(i)}|\Psi\rangle \\ |\psi_3\rangle &= G_0 V_3|\Psi\rangle\,, \end{aligned} \tag{B.2}$$

where we have included an extra Faddeev component for the three-body interaction. From this definition follows

$$|\Psi\rangle = \sum_{i=1}^{3}|\psi_2^{(i)}\rangle + |\psi_3\rangle\,. \tag{B.3}$$

According to this (B.2) can be rewritten as

$$|\psi_2^{(i)}\rangle = G_0 V_2^{(i)}\left(\sum_{i=1}^{3}|\psi_2^{(i)}\rangle + |\psi_3\rangle\right) \tag{B.4}$$

$$|\psi_3\rangle = G_0 V_3\left(\sum_{i=1}^{3}|\psi_2^{(i)}\rangle + |\psi_3\rangle\right)\,. \tag{B.5}$$

Next we introduce the operators

$$\begin{aligned} t_2^{(i)} &= V_2^{(i)} + V_2^{(i)} G_0 t_2^{(i)} \\ t_3 &= V_3 + V_3 G_0 t_3\,. \end{aligned} \tag{B.6}$$

From this one can easily deduce

$$(1 - G_0 V_2^{(i)})^{-1} G_0 V_2^{(i)} = G_0 t_2^{(i)} \tag{B.7}$$

$$(1 - G_0 V_3)^{-1} G_0 V_3 = G_0 t_3\,. \tag{B.8}$$

As throughout this thesis, we define the Faddeev component 1 to be the standard component and thus omit the index 1. In the next step we move the $|\psi_2\rangle$ term to the left side in (B.5)

$$\left(1 - G_0 V_2\right)|\psi_2\rangle = G_0 V_2\left(\sum_{i=2}^{3}|\psi_2^{(i)}\rangle| + |\psi_3\rangle\right)\,. \tag{B.9}$$

By multiplying $(1 - G_0 V_2)^{-1}$ from the left, we obtain

$$|\psi_2\rangle = G_0 t_2\left(\sum_{i=2}^{3}|\psi_2^{(i)}\rangle| + |\psi_3\rangle\right)\,. \tag{B.10}$$

Similarly holds

$$|\psi_3\rangle = G_0 t_3\left(\sum_{i=1}^{3}|\psi_2^{(i)}\rangle\right)\,. \tag{B.11}$$

Plugging (B.11) into (B.10), it yields

$$|\psi_2\rangle = G_0 t_2 \left(\sum_{i=2}^{3} |\psi_2^{(i)}\rangle + G_0 t_3 \left(\sum_{i=1}^{3} |\psi_2^{(i)}\rangle \right) \right) . \tag{B.12}$$

Using the permutation operators the two remaining Faddeev components can be expressed by

$$\begin{aligned} |\psi_2^{(2)}\rangle =& P_{12} P_{23} |\psi_2\rangle \\ |\psi_2^{(3)}\rangle =& P_{13} P_{23} |\psi_2\rangle . \end{aligned} \tag{B.13}$$

Using these relations we finally obtain

$$|\psi_2\rangle = G_0 t_2 P |\psi_2\rangle + G_0 t_2 G_0 t_3 (1+P) |\psi_2\rangle \quad , \tag{B.14}$$

where $P = P_{12}P_{23} + P_{13}P_{23}$. Next we determine the matrix elements of the Faddeev equations in the case of a pure S-wave two-body interaction and for zero total momentum $L = 0$. Hence, in the remainder of this section we assume V_2 to be zero for all partial waves except for the S-wave. It is easy to verify that

$$\langle pq\,(l) | \psi_2 \rangle = 0 \qquad \text{for } l \neq 0 . \tag{B.15}$$

Recall that we defined the basis states for these angular momentum conditions in the following way $|pq\,(l\; j = l) L = 0\, M = 0\rangle := |pq\,(l)\rangle$ and $|p\, l = 0\, m = 0\rangle = |p\rangle$. Since we consider a pure S-wave potential $V_2^{(i)}$,

$$\langle p\, l m_l | t_2 | p' l' m_{l'} \rangle = 0 \qquad \text{for } l \neq 0 \vee l' \neq 0 \tag{B.16}$$

holds. In the three-body space the matrix elements of t_2 have to be diagonal in the quantum numbers of the spectator particle. Therefore, the following relation holds for the operator t_2 in our case

$$\langle pq\,(l) | t_2(E) | p' q'\,(l') \rangle = \langle p | \hat{t}_2(E - \tfrac{3}{4}q^2) | p' \rangle \frac{\delta(q-q')}{qq'} \delta_{l0} \delta_{l'0} , \tag{B.17}$$

with

$$\langle p | \hat{t}_2(E) | p' \rangle = \langle p | V_2 | p' \rangle + \langle p | V_2 G_0(E) \hat{t}_2(E) | p' \rangle . \tag{B.18}$$

We define the matrix elements

$$\begin{aligned} I_1 :=& \langle pq\,(0) | G_0 t_2 P | \psi_2 \rangle \\ I_2 :=& \langle pq\,(0) | G_0 t_2 G_0 t_3 (1+P) | \psi_2 \rangle , \end{aligned} \tag{B.19}$$

such that Eq. (B.14) can be written as $\langle pq\,(0) | \psi_2 \rangle = I_1 + I_2$ with

$$I_1 = \frac{1}{E - p^2 - \frac{3}{4}q^2} \int_0^\infty dp'' p''^2 \int_{-1}^{1} dx \langle p | \hat{t}_2(E - \tfrac{3}{4}q^2) | p'' \rangle \langle \pi_1(p'', q, x)\, \pi_2(p'', q, x)\,(0) | \psi_2 \rangle \tag{B.20}$$

and

$$\begin{aligned} I_2 =& \frac{1}{E - p^2 - \frac{3}{4}q^2} \int_0^\infty dp'' p''^2 \langle p | \hat{t}_2(E - \tfrac{3}{4}q^2) | p'' \rangle \frac{1}{E - p''^2 - \frac{3}{4}q^2} \int_0^\infty \int_0^\infty dp_3 dq_3\; p_3^2 q_3^2 \cdot \\ & \Big[\langle p'' q\,(0) | t_3 | p_3 q_3\,(0) \rangle \langle p_3 q_3\,(0) | \psi_2 \rangle + \sum_{l_2} \int_{-1}^{1} dx \sqrt{[l_2]} P_{l_2}(x) \langle p'' q\,(0) | t_3 | p_3 q_3\,(l_2) \rangle \cdot \\ & \langle \pi_1(p_3, q_3, x)\, \pi_2(p_3, q_3, x)\,(0) | \psi_2 \rangle \Big] , \end{aligned} \tag{B.21}$$

where the sum over l_2 runs effectively only over even indices because we consider identical bosons and the wave function is otherwise zero.

C Finite Density Loop Integrals

In this chapter the calculation of the loop integral, defined in (7.2), will be explained in detail. This loop integral is needed for the computation of the full dimer propagator, which is an essential ingredient for the computation of the three-body scattering amplitude. We indicate that this loop integral was already calculated for equal masses in my diploma thesis [37]. However, due to the implementation of different masses, the boundary conditions become far more complex. The loop integral for the case of included hole propagation was not calculated in my diploma thesis. In section C.1 we begin with the computation of the in-medium loop integral without hole propagation. The calculation of the loop integral with included hole propagation I_k^V is given in section C.2. Due to the similarity of the derivations, we will discuss the first derivation in detail and outline the second one.

C.1 Loop Integration without Hole Propagation

In this section we consider the loop integral without hole propagation as can easily be seen by the theta functions. The loop integral is defined as follows

$$iI_k(P_0,\mathbf{P}) = \int_{|\mathbf{q}|<\Lambda} \frac{d^4q}{(2\pi)^4} \left(\frac{i\Theta\left(\left|\frac{m_i}{M_k}\mathbf{P}+\mathbf{q}\right|-k_F\right)}{\frac{m_i}{M_k}P_0+q_0-\frac{1}{2m_i}\left(\frac{m_i}{M_k}\mathbf{P}+\mathbf{q}\right)^2+i\epsilon} \frac{i\Theta\left(\left|\frac{m_j}{M_k}\mathbf{P}-\mathbf{q}\right|-k_F\right)}{\frac{m_j}{M_k}P_0-q_0-\frac{1}{2m_j}\left(\frac{m_j}{M_k}\mathbf{P}-\mathbf{q}\right)^2+i\epsilon} \right) . \tag{C.1}$$

This particular choice of the propagator momenta leads to a separation of the kinetic energy into the center of mass and relative kinetic energy as can be seen in the following. We introduce a cutoff Λ since the integral is divergent. This cutoff will vanish after the renormalization of the two-body system.

The first step is to perform a contour integration, where one pole is located in the upper and lower complex half-plane. We obtain

$$iI_k(P_0,\mathbf{P}) = i\int_{|\mathbf{q}|<\Lambda} \frac{d^3q}{(2\pi)^3} \frac{\Theta\left(\left|\frac{m_i}{M_k}\mathbf{P}+\mathbf{q}\right|-k_F\right)\Theta\left(\left|\frac{m_j}{M_k}\mathbf{P}-\mathbf{q}\right|-k_F\right)}{\frac{m_i}{M_k}P_0+\frac{m_j}{M_k}P_0-\frac{1}{2m_j}\left(\frac{m_j}{M_k}\mathbf{P}-\mathbf{q}\right)^2-\frac{1}{2m_i}\left(\frac{m_i}{M_k}\mathbf{P}+\mathbf{q}\right)^2+i\epsilon} . \tag{C.2}$$

The integral can be further simplified to

$$iI_k(P_0,\mathbf{P}) = i\int_{|\mathbf{q}|<\Lambda} \frac{d^3q}{(2\pi)^3} \frac{\Theta\left(\left|\frac{m_i}{M_k}\mathbf{P}+\mathbf{q}\right|-k_F\right)\Theta\left(\left|\frac{m_j}{M_k}\mathbf{P}-\mathbf{q}\right|-k_F\right)}{P_0-\frac{p^2}{2M_k}-\frac{q^2}{2\mu_k}+i\epsilon} . \tag{C.3}$$

The kinetic energy is now separated and the angle dependence disappeared in the denominator. Certainly, the theta functions still depend on the angle between the momenta $\mathbf{P}$ and $\mathbf{q}$. We switch to spherical coordinates and perform the ϕ integration, which yields a factor of 2π. Additionally, we introduce the abbreviation $b_k = 2\mu_k(P_0-\frac{p^2}{2M_k}+i\epsilon)$. This leads to

$$iI_k(P_0,\mathbf{P}) = \frac{2i\mu_k}{(2\pi)^2}\int_0^\Lambda\int_{-1}^1 dqdx \frac{q^2\Theta\left(\left|\frac{m_i}{M_k}\mathbf{P}+\mathbf{q}\right|-k_F\right)\Theta\left(\left|\frac{m_j}{M_k}\mathbf{P}-\mathbf{q}\right|-k_F\right)}{b_k-q^2} . \tag{C.4}$$

The variable x denotes $x := \cos\theta$ with the angle $\theta = \sphericalangle(\mathbf{P},\mathbf{q})$. The integrand is independent of the angle, but the theta functions imply boundary conditions for the angle and the q integration.

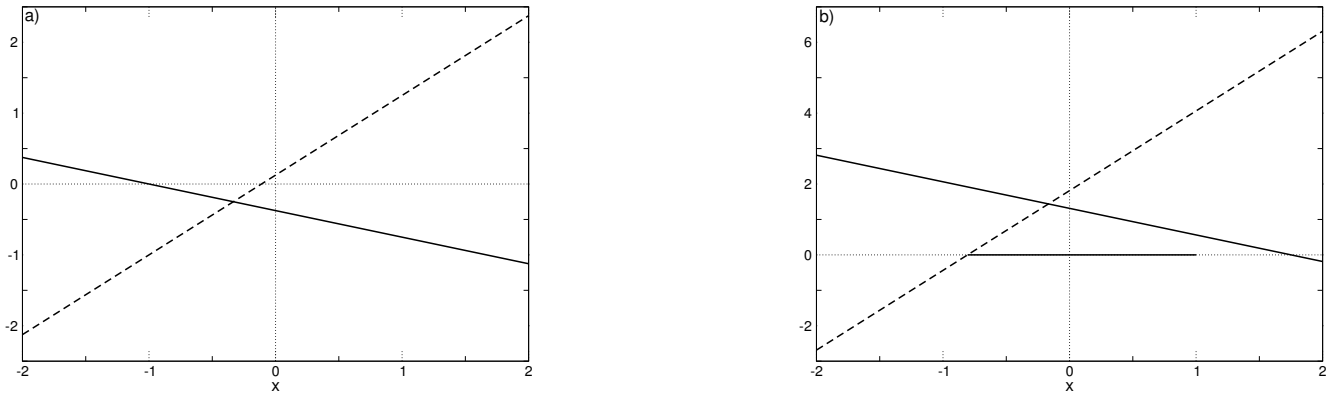

Figure C.1.: In this graph the straight lines g_1 and g_2 are exemplary depicted for two different values of q. The dashed line is g_1 and the solid line is g_2. In b) the x integration region is additionally represented by the horizontal solid line.

C.1.1 Boundary Conditions

This section is concerned with the boundary conditions of the integral, which are imposed by the theta functions. For convenience we change the notation a bit in this chapter. Without loss of generality we assume $m_i \geq m_j$ and denote $m_1 := m_i$ and $m_2 := m_j$. In addition, we omit the subscripts of M_k and b_k. Thus, using this notation $m_1 \geq m_2$, $M = m_1 + m_2$, $b = 2\mu(P_0 - P^2/(2M) + i\epsilon)$ and $1/\mu = 1/m_1 + 1/m_2$ holds. Effectively, we consider only two particles in this notation. At the end of this section we will return to the standard notation for three particles.

After these preliminary remarks we turn to the discussion of the boundary conditions. One directly recognizes that we only obtain a contribution to the integral if the two inequalities given by the theta functions are fulfilled at the same time. The two inequalities can be written as

$$\begin{aligned} g_1(x) &:= \left(\tfrac{m_1}{M}P\right)^2 + 2\tfrac{m_1}{M}Pqx + q^2 - k_F^2 > 0 \\ g_2(x) &:= \left(\tfrac{m_2}{M}P\right)^2 - 2\tfrac{m_2}{M}Pqx + q^2 - k_F^2 > 0\,, \end{aligned}$$

where we define the two functions g_1 and g_2. We consider g_1 and g_2 to be functions of the angle x. Hence, the two functions are straight lines with the parameters P and q. This implies that we first perform the x integration in dependence on q and P and then integrate over the loop momentum q, where we have to distinguish different cases depending on the total momentum P. The main task is now to determine when both lines have positive values, where one has to keep in mind that the maximal integration region of x is $[-1,+1]$.

Since the integration regions are not obvious for unequal masses, we first compute all relevant information to solve this problem. Subsequently, we determine the different integration regions. In Fig. C.1 the two straight lines and the integration region are exemplary depicted. Note that the only parameter which is different between the two graphs is the loop momentum q. One recognizes that the intersection point of g_1 and g_2 has to lie above the x axis. Otherwise there exists no region in which both lines have a positive value. If the intersection point is above the x axis, the root of g_1 is always smaller than the root of g_2. Also important to note is that g_1 has always a positive and g_2 always a negative slope. In Fig. C.1 b) the integration region is explicitly marked. In this example the integration region is not simply the range between the two roots. As mentioned above, it has to be considered that the maximal integration region ranges from -1 to 1 since x is the cosine of the angle between $\mathbf{P}$ and $\mathbf{q}$.

We proceed with the determination of the roots. We obtain

$$x_1 = \frac{k_F^2 - q^2 - \frac{m_1^2}{M^2}P^2}{2\frac{m_1}{M}Pq} \quad \text{and} \quad x_2 = \frac{-k_F^2 + q^2 + \frac{m_2^2}{M^2}P^2}{2\frac{m_2}{M}Pq}\,, \tag{C.5}$$

where x_1 denotes the root of $g_1(x)$ and x_2 the root of $g_2(x)$. It is also necessary to know when the roots have the value -1 or $+1$.

$$\begin{aligned} x_1 = 1 \Longrightarrow q = -\tfrac{m_1}{M}P \pm k_F \quad &, \quad x_1 = -1 \Longrightarrow q = +\tfrac{m_1}{M}P \pm k_F \\ x_2 = 1 \Longrightarrow q = +\tfrac{m_2}{M}P \pm k_F \quad &, \quad x_2 = -1 \Longrightarrow q = -\tfrac{m_2}{M}P \pm k_F \end{aligned} \tag{C.6}$$

In principle we find for every root two possible solutions for q. However, q has to be larger than zero. Consequently, it depends on the relation between P and k_F which solutions are valid. In this context the two boundaries $\frac{M}{m_1}k_F$ and $\frac{M}{m_2}k_F$ for the total momentum P have to be distinguished. In the next step we compute the intersection point of g_1 and g_2

$$g_1(x) = g_2(x) \Longrightarrow x_S = \frac{(m_2 - m_1)}{(m_2 + m_1)} \frac{P}{2q} , \tag{C.7}$$

where x_S denotes the x value of the intersection point. Since we assumed m_1 to be larger than m_2, it follows that x_S is smaller than zero. The intersection point has to be above the x axis in order to obtain a contribution to the integral. Hence, we evaluate g_1 at the intersection point

$$g_1(x_S) = \frac{m_1 m_2}{M^2} P^2 + q^2 - k_F^2 . \tag{C.8}$$

The function value of the straight lines at the intersection point is monotonically increasing with q. We only have to determine when the intersection point lies on the x axis, $g_1(x_S) = 0$. Subsequently, we can state the range of q in which the intersection point is above the x axis. Notice that for $P > \frac{M}{\sqrt{m_1 m_2}}k_F$ the intersection point is always positive. The boundary value q_G is given by

$$g_1(x_S) = 0 \Longrightarrow \quad q = \sqrt{k_F^2 - \frac{m_1 m_2}{M^2} P^2} := q_G . \tag{C.9}$$

If $q > q_G$, the intersection point lies above the x axis. A second boundary for the total momentum appears here. For $P < \frac{M}{\sqrt{m_1 m_2}}k_F$ the square root is real and the q integration begins at the first at q_G. If $P > \frac{M}{\sqrt{m_1 m_2}}k_F$, the intersection point is positive for all q. In this case the q integration can in principle start at $q = 0$.

Nevertheless, the region between x_1 and x_2 does not overlap with the interval $[-1, +1]$ in every case. In this instance there is of course no contribution to the integral. Hence, it is crucial to know if $x_S(q_G)$ lies in the interval $[-1, +1]$. It shows that $x_S(q_G) \in [-1, 0]$ for $P \leq 2k_F$ and $x_S(q_G) \in [-\infty, -1]$ for $P \geq 2k_F$. In other words, if $P < 2k_F$, the intersection point on the x axis lies inside the maximum integration region. If $P > 2k_F$, it lies outside.

Up to this point we have found four different boundaries for the total momentum P: $\frac{M}{m_1}k_F$, $\frac{M}{m_2}k_F$, $\frac{M}{\sqrt{m_1 m_2}}k_F$ and $2k_F$. They can be ordered in the following way

$$0 < \frac{M}{m_1}k_F \leq 2k_F \leq \frac{M}{\sqrt{m_1 m_2}}k_F \leq \frac{M}{m_2}k_F . \tag{C.10}$$

These boundaries impose many different distinctions. Thus, the boundary conditions seem to become very complicated. Fortunately, some distinctions can be consolidated as we will see in the following. We orientate us by the roots of the straight lines and distinguish three different cases for the total momentum P

$$\begin{aligned} A: &\quad P \in [0, \tfrac{M}{m_1}k_F] \\ B: &\quad P \in [\tfrac{M}{m_1}k_F, \tfrac{M}{m_2}k_F] \\ C: &\quad P > \tfrac{M}{m_2}k_F . \end{aligned} \tag{C.11}$$

Region A:

We start with summarizing the roots of Eq. (C.6) for $P \in [0, \frac{M}{m_1}k_F]$

$$\begin{aligned} x_1 = 1 \Longrightarrow q = -\tfrac{m_1}{M}P + k_F \quad , \quad x_1 = -1 \Longrightarrow q = +\tfrac{m_1}{M}P + k_F \\ x_2 = 1 \Longrightarrow q = +\tfrac{m_2}{M}P + k_F \quad , \quad x_2 = -1 \Longrightarrow q = -\tfrac{m_2}{M}P + k_F . \end{aligned}$$

We have determined the q values at which the roots enter or leave the region $[-1, +1]$. In the next step we consider the general course of the roots. Since we integrate over x in dependence on the loop momentum q, we consider the roots $x_1(q)$ and $x_2(q)$ to be functions of q. For small or large momenta the roots go to $\pm\infty$. There are two possible cases for the functions $x_1(q)$ and $x_2(q)$. Either the functions decrease or increase monotonically or there is one extremum and the functions have the same limit for small and large momenta. In region A we obtain

$$\begin{aligned} x_1(q \to 0) \to +\infty \quad &\text{and} \quad x_1(q \to \infty) \to -\infty \\ x_2(q \to 0) \to -\infty \quad &\text{and} \quad x_2(q \to \infty) \to +\infty . \end{aligned} \tag{C.12}$$

The course of x_1 and x_2 in this instance is monotone, the intersection point is positive for $q > q_G$ and $x_S(q_G) \in [-1,0]$. The integration regions can now be stated in the following way

$$\begin{aligned} [x_1, x_2] \quad &\text{for} \quad q_G \leq q \leq \tfrac{m_2}{M} P + k_F \\ [x_1, 1] \quad &\text{for} \quad \tfrac{m_2}{M} P + k_F \leq q \leq \tfrac{m_1}{M} P + k_F \\ [-1, 1] \quad &\text{for} \quad \tfrac{m_1}{M} P + k_F \leq q \leq \Lambda \,. \end{aligned} \tag{C.13}$$

Region B:

We consider region B, where the range of the total momentum is $P \in [\frac{M}{m_1} k_F, \frac{M}{m_2} k_F]$. As in the previous case, we state the roots

$$\begin{aligned} x_1 = 1 \Longrightarrow q = \not{z} \quad , \qquad & x_1 = -1 \Longrightarrow q = +\tfrac{m_1}{M} P \pm k_F \\ x_2 = 1 \Longrightarrow q = +\tfrac{m_2}{M} P + k_F \quad , \quad & x_2 = -1 \Longrightarrow q = -\tfrac{m_2}{M} P + k_F \,, \end{aligned}$$

where in this instance x_1 never attains the value $+1$ and hence there is no corresponding q value. The limits for large and small momenta are given by

$$\begin{aligned} x_1(q \to 0) \to -\infty \quad &\text{and} \quad x_1(q \to \infty) \to -\infty \\ x_2(q \to 0) \to -\infty \quad &\text{and} \quad x_2(q \to \infty) \to +\infty \,. \end{aligned} \tag{C.14}$$

Since the boundary $2k_F$ is located in region B, we further have to discern whether the total momentum P is larger or smaller than $2k_F$. For $P < 2k_F$ still holds $x_S(q_G) \in [-1,0]$. This leads to the same integration region as in region A since all relevant roots remain the same. Still left to consider is the subregion $P \in [2k_F, \frac{M}{m_2} k_F]$. In this region $x_S(q_G) \in [-\infty, -1]$ holds. Consequently, the integration does not begin at $q = q_G$. It starts when x_2 reaches the value -1. The lowest boundary for the q integration is then $-\frac{m_2}{M} P + k_F$. In this connection another boundary value for the total momentum disappears. Since the q integration starts at $-\frac{m_2}{M} P + k_F$, it is no longer necessary to distinguish if the intersection point is positive for all momenta q or only for momenta $q > q_G$. The boundary $\frac{M}{\sqrt{m_1 m_2}} k_F$ is hence of no significance.

Next we have to determine the order of the relevant roots because it is essential to know in which sequence the roots enter of leave the region $[-1,+1]$. For $P \geq 2k_F$ we obtain

$$-\tfrac{m_2}{M} P + k_F < \tfrac{m_1}{M} P - k_F \gtreqless \tfrac{m_2}{M} P + k_F < \tfrac{m_1}{M} P + k_F \,. \tag{C.15}$$

It depends on the momentum P if $\frac{m_1}{M} P - k_F$ or $\frac{m_2}{M} P + k_F$ is larger. Nevertheless, the order of these two boundaries is irrelevant for the computation of the loop integral. We demonstrate this by a short calculation. To improve readability, we abbreviate the limits of the q integration with a, b, c and d. We evaluate the relevant integral for two cases, where we interchange the middle limits b and c. The outer limits are kept constant. In a sloppy notation we get the two cases

$$\begin{aligned} (i) &:= \left(\int_a^b \int_{-1}^{x_2} + \int_b^c \int_{x_1}^{x_2} + \int_c^d \int_{x_1}^{1} \right) \cdot f(q)\, dx dq \\ (ii) &:= \left(\int_a^c \int_{-1}^{x_2} + \int_c^b \int_{-1}^{1} + \int_b^d \int_{x_1}^{1} \right) \cdot f(q)\, dx dq \,. \end{aligned} \tag{C.16}$$

The integrand is abbreviated by $f(q)$ in order to keep the calculation focused on the relevant aspects. When we interchange the middle q integral limits, the limits of the x integration also have to be modified in the appropriate way. This is due to the fact that interchanging the order of the q limits is related to a new order of the roots leaving or entering the maximum integration region. The integrand depends on q only and we get

$$\begin{aligned} (i) &= \int_a^b dq\, (x_2 + 1) f(q) + \int_b^c dq\, (x_2 - x_1) f(q) + \int_c^d dq\, (1 - x_1) f(q) \\ (ii) &= \int_a^c dq\, (x_2 + 1) f(q) + \int_c^b dq\, 2 f(q) + \int_b^d dq\, (1 - x_1) f(q) \,. \end{aligned} \tag{C.17}$$

According to the definitions in the next section, we denote the antiderivatives in the following way: $F_2(q) = \int dq\, x_2 f(q)$, $F_1(q) = \int dq\, x_1 f(q)$ and $F_0(q) = \int dq\, f(q)$. We express the integrals by the primitive integrals and summarize them. Finally we get

$$\begin{aligned}(i) =& -F_2(a) - F_1(d) + F_0(d) - F_0(a) + F_0(b) + F_1(b) + F_2(c) - F_0(c)\\ (ii) =& -F_2(a) - F_1(d) + F_0(d) - F_0(a) + F_0(b) + F_1(b) + F_2(c) - F_0(c)\,.\end{aligned} \tag{C.18}$$

The same result is obtained for both cases. Hence, we have shown that the order of the two boundaries $\frac{m_1}{M}P - k_F$ and $\frac{m_2}{M}P + k_F$ does not have to be distinguished. We make a choice for the order and summarize for $P \in [2k_F, \frac{M}{m_2}k_F]$

$$\begin{aligned}[-1, x_2] \quad &\text{for} \quad -\tfrac{m_2}{M}P + k_F \le q \le \tfrac{m_1}{M}P - k_F\\ [x_1, x_2] \quad &\text{for} \quad \tfrac{m_1}{M}P - k_F \le q \le \tfrac{m_2}{M}P + k_F\\ [x_1, 1] \quad &\text{for} \quad \tfrac{m_2}{M}P + k_F \le q \le \tfrac{m_1}{M}P + k_F\\ [-1, 1] \quad &\text{for} \quad \tfrac{m_1}{M}P + k_F \le q \le \Lambda\,.\end{aligned} \tag{C.19}$$

As a reminder, for $P \in [\frac{M}{m_1}k_F, 2k_F]$ we get same boundary conditions as in region A.

Region C:

The last region to consider is $P > \frac{M}{m_2}k_F$. The roots and limits in this case are

$$\begin{aligned}x_1 = 1 \Longrightarrow q = \lightning \quad , \qquad & x_1 = -1 \Longrightarrow q = +\tfrac{m_1}{M}P \pm k_F\\ x_2 = 1 \Longrightarrow q = +\tfrac{m_2}{M}P \pm k_F \quad , \quad & x_2 = -1 \Longrightarrow q = \lightning\end{aligned}$$

$$\begin{aligned}x_1(q \to 0) \to -\infty \quad &\text{and} \quad x_1(q \to \infty) \to -\infty\\ x_2(q \to 0) \to +\infty \quad &\text{and} \quad x_2(q \to \infty) \to +\infty\,.\end{aligned} \tag{C.20}$$

The order of the q values is

$$\tfrac{m_2}{M}P - k_F < \tfrac{m_2}{M}P + k_F \gtreqless \tfrac{m_1}{M}P - k_F < \tfrac{m_1}{M}P + k_F\,. \tag{C.21}$$

We obtain the same middle limits as in the previous case. Their order is thus not relevant for the integration. Due to the limits of x_1 and x_2 for small and large momenta as well as the fact that the intersection point is always positive, it follows that the q integration in this region begins at 0. Consequently, the boundary conditions can be written as

$$\begin{aligned}[-1, 1] \quad &\text{for} \quad 0 \le q \le \tfrac{m_2}{M}P - k_F\\ [-1, x_2] \quad &\text{for} \quad \tfrac{m_2}{M}P - k_F \le q \le \tfrac{m_2}{M}P + k_F\\ [-1, 1] \quad &\text{for} \quad \tfrac{m_2}{M}P + k_F \le q \le \tfrac{m_1}{M}P - k_F\\ [x_1, 1] \quad &\text{for} \quad \tfrac{m_1}{M}P - k_F \le q \le \tfrac{m_1}{M}P + k_F\\ [-1, 1] \quad &\text{for} \quad \tfrac{m_1}{M}P + k_F \le q \le \Lambda\,.\end{aligned} \tag{C.22}$$

Summary:

All boundary conditions are now determined. We were able to reduce the number of cases to three: $P \in [0, 2k_F]$, $P \in [2k_F, \frac{M}{m_2}k_F]$ and $P > \frac{M}{m_2}k_F$, which we summarize here.

$P \in [0, 2k_F]$:

$$\begin{aligned}[x_1, x_2] \quad &\text{for} \quad q_G \le q \le \tfrac{m_2}{M}P + k_F\\ [x_1, 1] \quad &\text{for} \quad \tfrac{m_2}{M}P + k_F \le q \le \tfrac{m_1}{M}P + k_F\\ [-1, 1] \quad &\text{for} \quad \tfrac{m_1}{M}P + k_F \le q \le \Lambda\end{aligned} \tag{C.23}$$

$P \in [2k_F, \frac{M}{m_2}k_F]$:

$$\begin{aligned}
[-1, x_2] \quad &\text{for} \quad -\tfrac{m_2}{M}P + k_F \leq q \leq \tfrac{m_1}{M}P - k_F \\
[x_1, x_2] \quad &\text{for} \quad \tfrac{m_1}{M}P - k_F \leq q \leq \tfrac{m_2}{M}P + k_F \\
[x_1, 1] \quad &\text{for} \quad \tfrac{m_2}{M}P + k_F \leq q \leq \tfrac{m_1}{M}P + k_F \\
[-1, 1] \quad &\text{for} \quad \tfrac{m_1}{M}P + k_F \leq q \leq \Lambda
\end{aligned} \tag{C.24}$$

$P > \frac{M}{m_2}k_F$:

$$\begin{aligned}
[-1, 1] \quad &\text{for} \quad 0 \leq q \leq \tfrac{m_2}{M}P - k_F \\
[-1, x_2] \quad &\text{for} \quad \tfrac{m_2}{M}P - k_F \leq q \leq \tfrac{m_2}{M}P + k_F \\
[-1, 1] \quad &\text{for} \quad \tfrac{m_2}{M}P + k_F \leq q \leq \tfrac{m_1}{M}P - k_F \\
[x_1, 1] \quad &\text{for} \quad \tfrac{m_1}{M}P - k_F \leq q \leq \tfrac{m_1}{M}P + k_F \\
[-1, 1] \quad &\text{for} \quad \tfrac{m_1}{M}P + k_F \leq q \leq \Lambda
\end{aligned} \tag{C.25}$$

We proceed with the evaluation of the integral.

C.1.2 Integration

As we have seen in the previous section, we obtained many boundaries for three different cases of the total momentum P. To ease the computation, we first calculate the indefinite integrals and then insert the boundaries. There are in total three different integrals. The first integral we consider is

$$\begin{aligned}
F_0(q) := I_1 &= \int dq\, \frac{q^2}{b - q^2} = \int dq \left(-1 - \frac{\sqrt{b}}{2} \left(\frac{1}{q - \sqrt{b}} - \frac{1}{q + \sqrt{b}} \right) \right) \\
&= -q - \frac{\sqrt{b}}{2} \left(\ln(q - \sqrt{b}) - \ln(q + \sqrt{b}) \right) ,
\end{aligned} \tag{C.26}$$

where we have used an expansion into partial fractions in the first step. The two remaining integrals are of the form $\int dq\, x_1 f(q)$ as well as $\int dq\, x_2 f(q)$ with $f(q) := \frac{q^2}{b-q^2}$. They are explicitly given by

$$\int dq\, \frac{-q^2 + k_F^2 - \frac{m_1^2 P^2}{M^2}}{2\frac{m_1}{M}pq} \frac{q^2}{b - q^2} \quad \text{and} \quad \int dq\, \frac{q^2 - k_F^2 + \frac{m_2^2 P^2}{M^2}}{2\frac{m_2}{M}pq} \frac{q^2}{b - q^2} . \tag{C.27}$$

Besides the overall sign and the particle index the two integrals are equal. Therefore, we introduce the variable $\bar{P} = \frac{m}{M}P$ with the general mass m and compute the integral with this momentum variable. The integral I_2 is defined as follows

$$I_2 := \int dq\, \frac{q^2}{b - q^2} \frac{-q^2 + k_F^2 - \bar{P}^2}{2\bar{P}q} = \frac{1}{2\bar{P}} \int dq\, q \frac{-q^2 + k_F^2 - \bar{P}^2}{b - q^2} . \tag{C.28}$$

This integral can be solved using partial integration and the partial fraction decomposition $\int dq\, \frac{1}{b-q^2} = \frac{1}{2\sqrt{b}}(\frac{1}{q+\sqrt{b}} - \frac{1}{q-\sqrt{b}})$.

$$\begin{aligned}
I_2 =& \frac{1}{2\bar{P}} \left[q \left(q + \frac{\sqrt{b}}{2} \left(\ln(q - \sqrt{b}) - \ln(q + \sqrt{b}) \right) - \frac{k_F^2 - \bar{P}^2}{2\sqrt{b}} \left(\ln(q - \sqrt{b}) - \ln(q + \sqrt{b}) \right) \right) \right. \\
& \left. - \int dq \left(q + \frac{\sqrt{b}}{2} \left(\ln(q - \sqrt{b}) - \ln(q + \sqrt{b}) \right) - \frac{k_F^2 - \bar{P}^2}{2\sqrt{b}} \left(\ln(q - \sqrt{b}) - \ln(q + \sqrt{b}) \right) \right) \right] \\
I_2 =& \frac{1}{2\bar{P}} \left[q^2 + q \frac{\sqrt{b}}{2} \left(\ln(q - \sqrt{b}) - \ln(q + \sqrt{b}) \right) + q \frac{-k_F^2 + \bar{P}^2}{2\sqrt{b}} \left(\ln(q - \sqrt{b}) - \ln(q + \sqrt{b}) \right) \right. \\
& \left. - \frac{q^2}{2} - \left(\frac{\sqrt{b}}{2} + \frac{-k_F^2 + \bar{P}^2}{2\sqrt{b}} \right) \left((q - \sqrt{b}) \ln(q - \sqrt{b}) - (q + \sqrt{b}) \ln(q + \sqrt{b}) \right) \right] \\
I_2 =& \frac{1}{2\bar{P}} \left[\frac{q^2}{2} + \sqrt{b} \left(\frac{\sqrt{b}}{2} + \frac{-k_F^2 + \bar{P}}{2\sqrt{b}} \right) \left(\ln(q - \sqrt{b}) + \ln(q + \sqrt{b}) \right) \right] \\
I_2 =& \frac{q^2}{4\bar{P}} + \frac{b - k_F^2 + \bar{P}^2}{4\bar{P}} \left(\ln(q - \sqrt{b}) + \ln(q + \sqrt{b}) \right)
\end{aligned} \tag{C.29}$$

From this result we can deduce

$$F_2(q) := \int dq\, \frac{q^2}{b-q^2}\, x_2 = -\int dq\, \frac{q^2}{b-q^2}\, \frac{k_F^2 - q^2 - \frac{m_2^2}{M^2}P^2}{2\frac{m_2}{M}Pq}$$
$$= -\frac{q^2}{4\frac{m_2}{M}P} - \frac{b - k_F^2 + \frac{m_2^2}{M^2}P^2}{4\frac{m_2}{M}P}\left(\ln(q-\sqrt{b}) + \ln(q+\sqrt{b})\right), \tag{C.30}$$

as well as

$$F_1(q) := \int dq\, \frac{q^2}{b-q^2}\, x_1 = \int dq\, \frac{q^2}{b-q^2}\, \frac{k_F^2 - q^2 - \frac{m_1^2}{M^2}P^2}{2\frac{m_1}{M}Pq}\,.$$
$$= \frac{q^2}{4\frac{m_1}{M}P} + \frac{b - k_F^2 + \frac{m_1^2}{M^2}P^2}{4\frac{m_1}{M}P}\left(\ln(q-\sqrt{b}) + \ln(q+\sqrt{b})\right). \tag{C.31}$$

All necessary primitive integrals and boundary conditions are now determined. Before we continue, we want to briefly state the used definitions of the complex root and logarithm. In this thesis we use the principle value of the complex logarithm. This means for $z \in \mathbb{C} \neq 0$ $\ln(z) = \ln|z| + i\arg(z)$ with $\arg(z) \in]-\pi, \pi]$. The complex square root is defined as $\sqrt{z} = \sqrt{|z|}\exp(i\arg(z)/2)$ so that $\sqrt{z}$ lies in $\{\rho\, e^{i\phi} | \rho \in]0,\infty], \phi \in]-\pi/2, \pi/2]\}$.

We proceed with the calculation of the loop integral for the three different cases and define

$$H_k(P_0, P) := \frac{2\pi^2}{\mu_k} I_k(P_0, P)\,. \tag{C.32}$$

Recall that $f(q)$ is defined as $f(q) := \frac{q^2}{b-q^2}$.
Case $P < 2k_F$:

$$H_k(P_0,P) = \int_{q_G}^{\frac{m_2}{M}P+k_F}\int_{x_1}^{x_2} dq dx\, f(q) + \int_{\frac{m_2}{M}P+k_F}^{\frac{m_1}{M}P+k_F}\int_{x_1}^{1} dq dx\, f(q) + \int_{\frac{m_1}{M}P+k_F}^{\Lambda}\int_{-1}^{1} dq dx\, f(q)$$
$$= \int_{q_G}^{\frac{m_2}{M}P+k_F} dq\,(x_2 - x_1) f(q) + \int_{\frac{m_2}{M}P+k_F}^{\frac{m_1}{M}P+k_F} dq\,(1-x_1) f(q) + \int_{\frac{m_1}{M}P+k_F}^{\Lambda} dq\, 2f(q)$$
$$= F_2(\tfrac{m_2}{M}P + k_F) - F_2(q_G) + F_1(q_G) - F_0(\tfrac{m_2}{M}P + k_F) - F_1(\tfrac{m_1}{M}P + k_F) + 2F_0(\Lambda) - F_0(\tfrac{m_1}{M}P + k_F) \tag{C.33}$$

Inserting the different terms leads to

$$H_k(P_0,P) = 2F_0(\Lambda) + \tfrac{1}{2}P + k_F + \left(\frac{b-k_F^2}{4P}\frac{M}{\mu} + \tfrac{1}{4}P\right)\left(\ln(q_G - \sqrt{b}) + \ln(q_G + \sqrt{b})\right)$$
$$+ \frac{\sqrt{b}}{2}\left(\ln(\tfrac{m_2}{M}P + k_F - \sqrt{b}) - \ln(\tfrac{m_2}{M}P + k_F + \sqrt{b}) + \ln(\tfrac{m_1}{M}P + k_F - \sqrt{b}) - \ln(\tfrac{m_1}{M}P + k_F + \sqrt{b})\right)$$
$$- h_2\left(\ln(\tfrac{m_2}{M}P + k_F - \sqrt{b}) + \ln(\tfrac{m_2}{M}P + k_F + \sqrt{b})\right)$$
$$- h_1\left(\ln(\tfrac{m_1}{M}P + k_F - \sqrt{b}) + \ln(\tfrac{m_1}{M}P + k_F + \sqrt{b})\right), \tag{C.34}$$

where μ is the reduced mass of m_1 and m_2. Additionally, we introduced

$$h_i := \frac{b - k_F^2 + \frac{m_i^2}{M^2}P^2}{4\frac{m_i}{M}P}\,. \tag{C.35}$$

Case $P \in [2k_F, \frac{M}{m_2}k_F]$:

We move on to the second case.

$$
\begin{aligned}
H_k(P_0,P) =& \int_{-\frac{m_2}{M}P+k_F}^{\frac{m_1}{M}P-k_F}\int_{-1}^{x_2} dqdx\, f(q) + \int_{\frac{m_1}{M}P-k_F}^{\frac{m_2}{M}P+k_F}\int_{x_1}^{x_2} dqdx\, f(q) + \int_{\frac{m_2}{M}P+k_F}^{\frac{m_1}{M}P+k_F}\int_{x_1}^{1} dqdx\, f(q) \\
&+ \int_{\frac{m_1}{M}P+k_F}^{\Lambda}\int_{-1}^{1} dqdx\, f(q) \\
=& \int_{-\frac{m_2}{M}P+k_F}^{\frac{m_1}{M}P-k_F} dq\,(x_2+1)f(q) + \int_{\frac{m_1}{M}P-k_F}^{\frac{m_2}{M}P+k_F} dq\,(x_2-x_1)f(q) + \int_{\frac{m_2}{M}P+k_F}^{\frac{m_1}{M}P+k_F}(1-x_1)dq\, f(q) \\
&+ \int_{\frac{m_1}{M}P+k_F}^{\Lambda} dq\, 2f(q) \\
=& 2F_0(\Lambda) - F_2(-\tfrac{m_2}{M}P+k_F) + F_0(\tfrac{m_1}{M}P-k_F) - F_0(-\tfrac{m_2}{M}P+k_F) + F_1(\tfrac{m_1}{M}P-k_F) \\
&- F_1(\tfrac{m_1}{M}P+k_F) - F_0(\tfrac{m_1}{M}P+k_F) + F_2(\tfrac{m_2}{M}P+k_F) - F_0(\tfrac{m_2}{M}P+k_F) \\
=& 2F_0(\Lambda) + 2k_F + \frac{\sqrt{b}}{2}\left(\ln(\tfrac{m_1}{M}P-k_F+\sqrt{b}) - \ln(\tfrac{m_1}{M}P-k_F-\sqrt{b})\right) \\
&+ \frac{\sqrt{b}}{2}\left(\ln(\tfrac{m_1}{M}P+k_F-\sqrt{b}) - \ln(\tfrac{m_1}{M}P+k_F+\sqrt{b})\right) \\
&+ \frac{\sqrt{b}}{2}\left(\ln(-\tfrac{m_2}{M}P+k_F-\sqrt{b}) - \ln(-\tfrac{m_2}{M}P+k_F+\sqrt{b})\right) \\
&+ \frac{\sqrt{b}}{2}\left(\ln(\tfrac{m_2}{M}P+k_F-\sqrt{b}) - \ln(\tfrac{m_2}{M}P+k_F+\sqrt{b})\right) \\
&+ h_2\left(\ln(-\tfrac{m_2}{M}P+k_F-\sqrt{b}) + \ln(-\tfrac{m_2}{M}P+k_F+\sqrt{b}) - \ln(\tfrac{m_2}{M}P+k_F-\sqrt{b}) - \ln(\tfrac{m_2}{M}P+k_F+\sqrt{b})\right) \\
&+ h_1\left(\ln(\tfrac{m_1}{M}P-k_F-\sqrt{b}) + \ln(\tfrac{m_1}{M}P-k_F+\sqrt{b}) - \ln(\tfrac{m_1}{M}P+k_F-\sqrt{b}) - \ln(\tfrac{m_1}{M}P+k_F+\sqrt{b})\right) \qquad \text{(C.36)}
\end{aligned}
$$

Case $P \geq \frac{M}{m_2}k_F$:

The remaining case yields

$$
\begin{aligned}
H_k(P_0,P) =& \int_{0}^{\frac{m_2}{M}P-k_F}\int_{-1}^{1} dxdq\, f(q) + \int_{\frac{m_2}{M}P-k_F}^{\frac{m_2}{M}P+k_F}\int_{-1}^{x_2} dxdq\, f(q) + \int_{\frac{m_2}{M}P+k_F}^{\frac{m_1}{M}P-k_F}\int_{-1}^{1} dxdq\, f(q) \\
&+ \int_{\frac{m_1}{M}P-k_F}^{\frac{m_1}{M}P+k_F}\int_{x_1}^{1} dxdq\, f(q) + \int_{\frac{m_1}{M}P+k_F}^{\Lambda}\int_{-1}^{1} dxdq\, f(q) \\
=& 2F_0(\Lambda) - 2F_0(0) + F_0(\tfrac{m_2}{M}P-k_F) + F_2(\tfrac{m_2}{M}P+k_F) - F_2(\tfrac{m_2}{M}P-k_F) + F_0(\tfrac{m_1}{M}P-k_F) \\
&- F_0(\tfrac{m_2}{M}P+k_F) - F_1(\tfrac{m_1}{M}P+k_F) + F_1(\tfrac{m_1}{M}P-k_F) - F_0(\tfrac{m_1}{M}P+k_F) \\
H_k(P_0,P) =& 2k_F + 2F_0(\Lambda) - 2F_0(0) \\
&+ h_2\left(\ln(\tfrac{m_2}{M}P-k_F-\sqrt{b}) + \ln(\tfrac{m_2}{M}P-k_F+\sqrt{b}) - \ln(\tfrac{m_2}{M}P+k_F-\sqrt{b}) - \ln(\tfrac{m_2}{M}P+k_F+\sqrt{b})\right) \\
&+ h_1\left(\ln(\tfrac{m_1}{M}P-k_F-\sqrt{b}) + \ln(\tfrac{m_1}{M}P-k_F+\sqrt{b}) - \ln(\tfrac{m_1}{M}P+k_F-\sqrt{b}) - \ln(\tfrac{m_1}{M}P+k_F+\sqrt{b})\right) \\
&+ \tfrac{\sqrt{b}}{2}\left(\ln(\tfrac{m_2}{M}P+k_F-\sqrt{b}) - \ln(\tfrac{m_2}{M}P+k_F+\sqrt{b}) + \ln(\tfrac{m_2}{M}P-k_F+\sqrt{b}) - \ln(\tfrac{m_2}{M}P-k_F-\sqrt{b})\right) \\
&+ \tfrac{\sqrt{b}}{2}\left(\ln(\tfrac{m_1}{M}P+k_F-\sqrt{b}) - \ln(\tfrac{m_1}{M}P+k_F+\sqrt{b}) + \ln(\tfrac{m_1}{M}P-k_F+\sqrt{b}) - \ln(\tfrac{m_1}{M}P-k_F-\sqrt{b})\right). \qquad \text{(C.37)}
\end{aligned}
$$

Summary:

We return to the original notation of the masses. Still left to compute are the two terms $F_0(\Lambda)$ and $F_0(0)$

$$F_0(\Lambda) = -\Lambda - \frac{\sqrt{b_k}}{2}\left(\ln(\Lambda - \sqrt{b_k}) - \ln(\Lambda + \sqrt{b_k})\right) = -\Lambda - \frac{\sqrt{b_k}}{2}\left(\ln(|\Lambda|) - \ln(|\Lambda|)\right) = -\Lambda\,, \tag{C.38}$$

where we have used $\Lambda \gg |\sqrt{b_k}|$. For the computation of $F_0(0)$ we have to recall that $b_k = 2\mu_k(P_0 - \frac{P^2}{2M_k} + i\epsilon)$ with the real energy P_0 and momentum P.

$$\begin{aligned} F_0(0) =& -\frac{\sqrt{b_k}}{2}\left(\ln(-\sqrt{b_k}) - \ln(\sqrt{b_k})\right) = -\frac{\sqrt{b_k}}{2}\left(i\,\mathrm{Arg}(-\sqrt{b_k}) - i\,\mathrm{Arg}(\sqrt{b_k})\right) \\ =& i\pi\frac{\sqrt{b_k}}{2} = -\frac{\pi}{2}\sqrt{-b_k}\,. \end{aligned} \tag{C.39}$$

In the last step we have used $i\sqrt{b_k} = -\sqrt{-b_k}$ since the imaginary part of b_k is positive. One can show that the two cases for $P > 2k_F$ exhibit the same result. For the numerical implementation it is, nevertheless, useful to keep this distinction. We therefore state all of them.

In all three cases we obtain the same cutoff dependence 2Λ. The cutoff Λ will vanish after the renormalization procedure. Therefore, we define

$$H_k(P_0, P) = -2\Lambda + L_k(P_0, P)\,. \tag{C.40}$$

We summarize the three cases in the original notation of the masses for three particles. It still holds without loss of generality $m_i > m_j$.
$P < 2k_F$:

$$\begin{aligned} L_k(P_0,P) =& +\tfrac{1}{2}P + k_F + \left(\frac{b_k - k_F^2}{4P}\frac{M_k}{\mu_k} + \tfrac{1}{4}P\right)\left(\ln(q_G - \sqrt{b_k}) + \ln(q_G + \sqrt{b_k})\right) \\ &+ \frac{\sqrt{b_k}}{2}\left(\ln(\tfrac{m_i}{M_k}P + k_F - \sqrt{b_k}) - \ln(\tfrac{m_i}{M_k}P + k_F + \sqrt{b_k}) + \ln(\tfrac{m_j}{M_k}P + k_F - \sqrt{b_k}) - \ln(\tfrac{m_j}{M_k}P + k_F + \sqrt{b_k})\right) \\ &- h_i\left(\ln(\tfrac{m_i}{M_k}P + k_F - \sqrt{b_k}) + \ln(\tfrac{m_i}{M_k}P + k_F + \sqrt{b_k})\right) \\ &- h_j\left(\ln(\tfrac{m_j}{M_k}P + k_F - \sqrt{b_k}) + \ln(\tfrac{m_j}{M_k}P + k_F + \sqrt{b_k})\right) \end{aligned} \tag{C.41}$$

$P \in [2k_F, \frac{M_k}{m_j}k_F]$:

$$\begin{aligned} L_k(P_0,P) =& 2k_F \\ &+ \frac{\sqrt{b_k}}{2}\left(\ln(\tfrac{m_i}{M_k}P + k_F - \sqrt{b_k}) - \ln(\tfrac{m_i}{M_k}P + k_F + \sqrt{b_k}) + \ln(\tfrac{m_i}{M_k}P - k_F + \sqrt{b_k}) - \ln(\tfrac{m_i}{M_k}P - k_F - \sqrt{b_k})\right) \\ &+ \frac{\sqrt{b_k}}{2}\left(\ln(-\tfrac{m_j}{M_k}P + k_F - \sqrt{b_k}) - \ln(-\tfrac{m_j}{M_k}P + k_F + \sqrt{b_k}) + \ln(\tfrac{m_j}{M_k}P + k_F - \sqrt{b_k}) - \ln(\tfrac{m_j}{M_k}P + k_F + \sqrt{b_k})\right) \\ &+ h_i\left(\ln(\tfrac{m_i}{M_k}P - k_F - \sqrt{b_k}) + \ln(\tfrac{m_i}{M_k}P - k_F + \sqrt{b_k}) - \ln(\tfrac{m_i}{M_k}P + k_F - \sqrt{b_k}) - \ln(\tfrac{m_i}{M_k}P + k_F + \sqrt{b_k})\right) \\ &+ h_j\left(\ln(-\tfrac{m_j}{M_k}P + k_F - \sqrt{b_k}) + \ln(-\tfrac{m_j}{M_k}P + k_F + \sqrt{b_k}) - \ln(\tfrac{m_j}{M_k}P + k_F - \sqrt{b_k}) - \ln(\tfrac{m_j}{M_k}P + k_F + \sqrt{b_k})\right) \end{aligned} \tag{C.42}$$

$P > \frac{M_k}{m_j}k_F$:

$$\begin{aligned} L_k(P_0,P) =& 2k_F + \pi\sqrt{-b_k} \\ &+ h_i\left(\ln(\tfrac{m_i}{M_k}P - k_F - \sqrt{b_k}) + \ln(\tfrac{m_i}{M_k}P - k_F + \sqrt{b_k}) - \ln(\tfrac{m_i}{M_k}P + k_F - \sqrt{b_k}) - \ln(\tfrac{m_i}{M_k}P + k_F + \sqrt{b_k})\right) \\ &+ h_j\left(\ln(\tfrac{m_j}{M_k}P - k_F - \sqrt{b_k}) + \ln(\tfrac{m_j}{M_k}P - k_F + \sqrt{b_k}) - \ln(\tfrac{m_j}{M_k}P + k_F - \sqrt{b_k}) - \ln(\tfrac{m_j}{M_k}P + k_F + \sqrt{b_k})\right) \\ &+ \frac{\sqrt{b_k}}{2}\left(\ln(\tfrac{m_i}{M_k}P + k_F - \sqrt{b_k}) - \ln(\tfrac{m_i}{M_k}P + k_F + \sqrt{b_k}) + \ln(\tfrac{m_i}{M_k}P - k_F + \sqrt{b_k}) - \ln(\tfrac{m_i}{M_k}P - k_F - \sqrt{b_k})\right) \\ &+ \frac{\sqrt{b_k}}{2}\left(\ln(\tfrac{m_j}{M_k}P + k_F - \sqrt{b_k}) - \ln(\tfrac{m_j}{M_k}P + k_F + \sqrt{b_k}) + \ln(\tfrac{m_j}{M_k}P - k_F + \sqrt{b_k}) - \ln(\tfrac{m_j}{M_k}P - k_F - \sqrt{b_k})\right) \end{aligned} \tag{C.43}$$

with

$$b_k = 2\mu_k(P_0 - \tfrac{P^2}{2M_k} + i\epsilon), \quad q_G = \sqrt{k_F^2 - \tfrac{m_i m_j}{M_k^2}P^2} \quad \text{and } h_i = \frac{b_k - k_F^2 + \frac{m_i^2}{M_k^2}P^2}{4\frac{m_i}{M_k}P}\,.$$

Note that in the first and the last case the function $L_k(P_0, P)$ is symmetric under the interchange of m_i and m_j. Since the second and the third case are equal, the postulation $m_i > m_j$ is no longer necessary. Thus, the full dimer propagator is symmetric under the interchange of the two particles.

C.2 Loop Integration with included Hole Propagation

In this section we consider the loop integral with included hole and particle propagation. We therefore have to use the general in-medium propagators. The loop integral $I_k^V(P_0, \mathbf{P})$ is given by

$$\begin{aligned} iI_k^V(P_0,\mathbf{P}) = \int_{|\mathbf{q}|<\Lambda} \frac{d^4q}{(2\pi)^4} \left(\frac{i\Theta\left(\left|\frac{m_i}{M_k}\mathbf{P}+\mathbf{q}\right| - k_F\right)}{\frac{m_i}{M_k}P_0 + q_0 - \frac{1}{2m_i}\left(\frac{m_i}{M_k}\mathbf{P}+\mathbf{q}\right)^2 + i\epsilon} + \frac{i\Theta\left(k_F - \left|\frac{m_i}{M_k}\mathbf{P}+\mathbf{q}\right|\right)}{\frac{m_i}{M_k}P_0 + q_0 - \frac{1}{2m_i}\left(\frac{m_i}{M_k}\mathbf{P}+\mathbf{q}\right)^2 - i\epsilon} \right) \\ \times \left(\frac{i\Theta\left(\left|\frac{m_j}{M_k}\mathbf{P}-\mathbf{q}\right| - k_F\right)}{\frac{m_j}{M_k}P_0 - q_0 - \frac{1}{2m_j}\left(\frac{m_j}{M_k}\mathbf{P}-\mathbf{q}\right)^2 + i\epsilon} + \frac{i\Theta\left(k_F - \left|\frac{m_j}{M_k}\mathbf{P}-\mathbf{q}\right|\right)}{\frac{m_j}{M_k}P_0 - q_0 - \frac{1}{2m_j}\left(\frac{m_j}{M_k}\mathbf{P}-\mathbf{q}\right)^2 - i\epsilon} \right). \end{aligned} \tag{C.44}$$

The integral can be divided into two different contributions, hole-hole and particle-particle contribution. We have already calculated the particle-particle contribution in the previous section. Particle-hole contributions do not exist because in this case both poles lie in the same complex half-plane. Consequently, these contributions vanish after the q_0 integration. We now consider the hole-hole contribution and denote it with $iI_k^L(P_0, \mathbf{P})$

$$iI_k^L(P_0,\mathbf{P}) = \int_{|\mathbf{q}|<\Lambda} \frac{d^4q}{(2\pi)^4} \frac{i\Theta\left(k_F - \left|\frac{m_i}{M_k}\mathbf{P}+\mathbf{q}\right|\right)}{\frac{m_i}{M_k}P_0 + q_0 - \frac{1}{2m_i}\left(\frac{m_i}{M_k}\mathbf{P}+\mathbf{q}\right)^2 - i\epsilon} \frac{i\Theta\left(k_F - \left|\frac{m_j}{M_k}\mathbf{P}-\mathbf{q}\right|\right)}{\frac{m_j}{M_k}P_0 - q_0 - \frac{1}{2m_j}\left(\frac{m_j}{M_k}\mathbf{P}-\mathbf{q}\right)^2 - i\epsilon}\,. \tag{C.45}$$

For the total loop integral then yields

$$iI_k^V(P_0,\mathbf{P}) = iI_k(P_0,\mathbf{P}) + iI_k^L(P_0,\mathbf{P})\,. \tag{C.46}$$

We carry out the contour integration for the hole contribution and obtain

$$iI_k^L(P_0,\mathbf{P}) = -i\int_{|\mathbf{q}|<\Lambda} \frac{d^3q}{(2\pi)^3} \frac{\Theta\left(k_F - \left|\frac{m_i}{M_k}\mathbf{P}+\mathbf{q}\right|\right)\Theta\left(k_F - \left|\frac{m_j}{M_k}\mathbf{P}-\mathbf{q}\right|\right)}{P_0 - \frac{P^2}{2M_k} - \frac{q^2}{2\mu_k} - i\epsilon}\,. \tag{C.47}$$

The integral has the same form as the particle integral $iI_k(P_0, \mathbf{P})$. The integrals differ only in the theta functions, the overall sign and the sign of $i\epsilon$. After switching to spherical coordinates and carrying out the ϕ integration we get

$$iI_k^L(P_0,\mathbf{P}) = \frac{-i\mu_k}{2\pi^2}\int_0^\Lambda dq\, q^2 \int_{-1}^1 dx \frac{\Theta\left(k_F - \left|\frac{m_i}{M_k}\mathbf{P}+\mathbf{q}\right|\right)\Theta\left(k_F - \left|\frac{m_j}{M_k}\mathbf{P}-\mathbf{q}\right|\right)}{\overline{b}_k - q^2}\,, \tag{C.48}$$

where $x = \cos\theta$ with the angle $\theta = \sphericalangle(\mathbf{P}, \mathbf{q})$ and the abbreviation $\overline{b}_k = 2\mu_k(P_0 - \frac{P^2}{2M_k} - i\epsilon)$. Note that $\overline{b}_k$ and b_k differ only in the sign of $i\epsilon$. Analog to the previous section, we define

$$H_k^L(P_0,P) := -\frac{2\pi^2}{\mu_k} I_k^L(P_0,P)\,. \tag{C.49}$$

The total integral $iI_k^V(P_0, P)$ can be decomposed into

$$I_k^V(P_0,P) := \frac{\mu_k}{2\pi^2} H_k^V(P_0,P) = \frac{\mu_k}{2\pi^2}(H_k(P_0,P) - H_k^L(P_0,P))\,, \tag{C.50}$$

where we have defined $H_k^V = H_k - H_k^L$ as particle contribution minus hole contribution. Since the calculations are very similar to the particle case, we will shorten the derivation.

We start with the boundary conditions. All calculated results of the previous section can be further used. Therefore, we apply again the modified mass notation. As a reminder, we denote $m_1 = m_i$ and $m_2 = m_j$ with $m_1 \geq m_2$. All other particle indices will be omitted. The two straight lines are again defined as

$$\begin{aligned} g_1(x) &:= \left(\tfrac{m_1}{M}P\right)^2 + 2\tfrac{m_1}{M}Pqx + q^2 - k_F^2 < 0 \\ g_2(x) &:= \left(\tfrac{m_2}{M}P\right)^2 - 2\tfrac{m_2}{M}Pqx + q^2 - k_F^2 < 0\,, \end{aligned}$$

where in this case the theta functions imply that both lines have to be below the x axis. In contrast to the particle case, the intersection point has to lie below the x axis now. From this follows that the maximal loop momentum is q_G since for $q > q_G$ the intersection point lies above the x axis. Similarly, the maximal total momentum is $\frac{M}{\sqrt{m_1 m_2}}k_F$. From the already obtained results we distinguish the three regions for P: $[0, \frac{M}{m_1}k_F]$, $[\frac{M}{m_1}k_F, 2k_F]$ and $[2k_F, \frac{M}{\sqrt{m_1 m_2}}k_F]$.

The roots and limits can simply be employed from the previous section. For the region $P \in [0, \frac{M}{m_1}k_F]$ they are

$$\begin{aligned} x_1 = 1 &\Longrightarrow q = -\tfrac{m_1}{M}P + k_F \quad , & x_1 = -1 &\Longrightarrow q = +\tfrac{m_1}{M}P + k_F \\ x_2 = 1 &\Longrightarrow q = +\tfrac{m_2}{M}P + k_F \quad , & x_2 = -1 &\Longrightarrow q = -\tfrac{m_2}{M}P + k_F \end{aligned}$$

$$\begin{aligned} x_1(q \to 0) &\to +\infty \quad \text{and} \quad x_1(q \to \infty) \to -\infty \\ x_2(q \to 0) &\to -\infty \quad \text{and} \quad x_2(q \to \infty) \to +\infty\,. \end{aligned} \tag{C.51}$$

However, note that the order of x_1 and x_2 is changed when the intersection point lies under the x axis. From the limits of x_1 and x_2 as well as the fact that $q < q_G$, it follows that the integration already begins at $q = 0$. Also keep in mind that the intersection point lies in $x_S(q_G) \in [-1, 0]$ because $P < 2k_F$. Using this information we get the following boundary conditions

$$\begin{aligned} [-1, +1] \quad &\text{for} \quad 0 \leq q \leq -\tfrac{m_1}{M}P + k_F \\ [-1, x_1] \quad &\text{for} \quad -\tfrac{m_1}{M}P + k_F \leq q \leq -\tfrac{m_2}{M}P + k_F \\ [x_2, x_1] \quad &\text{for} \quad -\tfrac{m_2}{M}P + k_F \leq q \leq q_G\,. \end{aligned} \tag{C.52}$$

We now consider the case $P \in [\frac{M}{m_1}k_F, 2k_F]$ and repeat the results

$$\begin{aligned} x_1 = +1 &\to q = \not{\iota}\,, & x_1 = -1 &\to q = +\tfrac{m_1}{M}P \pm k_F \\ x_2 = +1 &\to q = +\tfrac{m_2}{M}P + k_F \quad , & x_2 = -1 &\to q = -\tfrac{m_2}{M}P + k_F \end{aligned}$$

$$\begin{aligned} x_1(q \to 0) &\to -\infty \quad \text{and} \quad x_1(q \to \infty) \to -\infty \\ x_2(q \to 0) &\to -\infty \quad \text{and} \quad x_2(q \to \infty) \to +\infty\,. \end{aligned} \tag{C.53}$$

The limits for small momenta have changed so that the q integration no longer starts at $q = 0$. The integration region in this case is

$$\begin{aligned} [-1, x_1] \quad &\text{for} \quad \tfrac{m_1}{M}P - k_F \leq q \leq -\tfrac{m_2}{M}P + k_F \\ [x_2, x_1] \quad &\text{for} \quad -\tfrac{m_2}{M}P + k_F \leq q \leq q_G\,. \end{aligned} \tag{C.54}$$

Next we examine the remaining region $P \in [2k_F, \frac{M}{\sqrt{m_1 m_2}}k_F]$. However, in this region $x_2 \leq x_1 \leq -1$ holds for all $q \leq q_G$. In other words the region between the roots does not overlap with the maximum integration region $[-1, +1]$. Hence, there is no contribution to the loop integral. The maximal total momentum for the hole integral is consequently $2k_F$. This result is not surprising since two holes in the Fermi sea can only have a maximal total momentum of $2k_F$.

The boundary conditions are determined. Thus, the next step is to carry out the integration. As mentioned above, the same integrals appear. Only the variable b_k has to be replaced by $\overline{b}_k$. Since the integration is analog, we skip the details

and directly state the results. It becomes apparent that the two cases for the total momentum yield the same results. We therefore choose one form and obtain

$$\begin{aligned}
H_k^L(P_0,P) =& \tfrac{1}{2}P - k_F + \left(\frac{\bar{b}_k - k_F^2}{4P}\frac{M_k}{\mu_k} + \tfrac{1}{4}P\right)\left(\ln(q_G - \sqrt{\bar{b}_k}) + \ln(q_G + \sqrt{\bar{b}_k})\right) + \sqrt{\bar{b}_k}\left(\ln(-\sqrt{\bar{b}_k}) - \ln(+\sqrt{\bar{b}_k})\right) \\
&- \tfrac{\sqrt{\bar{b}_k}}{2}\left(\ln(-\tfrac{m_i}{M_k}P + k_F - \sqrt{\bar{b}_k}) - \ln(-\tfrac{m_i}{M_k}P + k_F + \sqrt{\bar{b}_k}) + \ln(-\tfrac{m_j}{M_k}P + k_F - \sqrt{\bar{b}_k}) - \ln(-\tfrac{m_j}{M_k}P + k_F + \sqrt{\bar{b}_k})\right) \\
&- \bar{h}_i\left(\ln(-\tfrac{m_i}{M_k}P + k_F - \sqrt{\bar{b}_k}) + \ln(-\tfrac{m_i}{M_k}P + k_F + \sqrt{\bar{b}_k})\right) \\
&- \bar{h}_j\left(\ln(-\tfrac{m_j}{M_k}P + k_F - \sqrt{\bar{b}_k}) + \ln(-\tfrac{m_j}{M_k}P + k_F + \sqrt{\bar{b}_k})\right), \qquad \text{(C.55)}
\end{aligned}$$

where we have returned to the general notation. The high momentum contributions of the total loop integral are contained in the particle integral. We therefore analogously subtract the cutoff

$$H_k^V = -2\Lambda + L_k^V(P_0,P). \qquad \text{(C.56)}$$

The hole and particle integrals have to be subtracted in order to obtain the full integral, see Eq. (C.50). The final result for $L_k^V(P_0,P)$ with included hole and particle propagation for $P \leq 2k_F$ is

$$\begin{aligned}
L_k^V(P_0,P) =& 2k_F + \left(\frac{b_k - k_F^2}{4P}\frac{M_k}{\mu_k} + \tfrac{1}{4}P\right)\left(\ln(q_G - \sqrt{b_k}) + \ln(q_G + \sqrt{b_k})\right) \\
&+ \tfrac{\sqrt{b_k}}{2}\left(\ln(\tfrac{m_i}{M_k}P + k_F - \sqrt{b_k}) - \ln(\tfrac{m_i}{M_k}P + k_F + \sqrt{b_k}) + \ln(\tfrac{m_j}{M_k}P + k_F - \sqrt{b_k}) - \ln(\tfrac{m_j}{M_k}P + k_F + \sqrt{b_k})\right) \\
&- h_i\left(\ln(\tfrac{m_i}{M_k}P + k_F - \sqrt{b_k}) + \ln(\tfrac{m_i}{M_k}P + k_F + \sqrt{b_k})\right) \\
&- h_j\left(\ln(\tfrac{m_j}{M_k}P + k_F - \sqrt{b_k}) + \ln(\tfrac{m_j}{M_k}P + k_F + \sqrt{b_k})\right) \\
&- \left(\frac{\bar{b}_k - k_F^2}{4P}\frac{M_k}{\mu_k} + \tfrac{1}{4}P\right)\left(\ln(q_G - \sqrt{\bar{b}_k}) + \ln(q_G + \sqrt{\bar{b}_k})\right) - \sqrt{\bar{b}_k}\left(\ln(-\sqrt{\bar{b}_k}) - \ln(+\sqrt{\bar{b}_k})\right) \\
&+ \tfrac{\sqrt{\bar{b}_k}}{2}\left(\ln(-\tfrac{m_i}{M_k}P + k_F - \sqrt{\bar{b}_k}) - \ln(-\tfrac{m_i}{M_k}P + k_F + \sqrt{\bar{b}_k}) + \ln(-\tfrac{m_j}{M_k}P + k_F - \sqrt{\bar{b}_k}) - \ln(-\tfrac{m_j}{M_k}P + k_F + \sqrt{\bar{b}_k})\right) \\
&+ \bar{h}_i\left(\ln(-\tfrac{m_i}{M_k}P + k_F - \sqrt{\bar{b}_k}) + \ln(-\tfrac{m_i}{M_k}P + k_F + \sqrt{\bar{b}_k})\right) \\
&+ \bar{h}_j\left(\ln(-\tfrac{m_j}{M_k}P + k_F - \sqrt{\bar{b}_k}) + \ln(-\tfrac{m_j}{M_k}P + k_F + \sqrt{\bar{b}_k})\right) \qquad \text{(C.57)}
\end{aligned}$$

with

$$\begin{aligned}
b_k = 2\mu_k(P_0 - \tfrac{P^2}{2M_k} + i\epsilon) \quad , \quad q_G = \sqrt{k_F^2 - \tfrac{m_i m_j}{M_k^2}P^2} \quad , \quad h_i = \frac{b_k - k_F^2 + \frac{m_i^2}{M_k^2}P^2}{4\frac{m_i}{M_k}P} \quad , \\
\bar{b}_k = 2\mu_k(P_0 - \tfrac{P^2}{2M_k} - i\epsilon) \quad \text{and} \quad \bar{h}_i = \frac{\bar{b}_k - k_F^2 + \frac{m_i^2}{M_k^2}P^2}{4\frac{m_i}{M_k}P}. \qquad \text{(C.58)}
\end{aligned}$$

At the end we want to note that for the total momentum $P > 2k_F$ the total integral is given by the particle integral since the hole contribution vanishes.

Bibliography

[1] E. Braaten and H.-W. Hammer, Universality in few-body systems with large scattering length, Phys. Rep. **428**, 259 (2006), arXiv:cond-mat/0410417 [cond-mat.other].

[2] V. Efimov, Energy Levels Arising from Resonant Two-body Forces in a Three- body System, Phys. Lett. B **33**, 563 (1970).

[3] D. Sornette, Discrete-scale invariance and complex dimensions, Phys. Rep. **297**, 239 (1998), arXiv:cond-mat/9707012 [cond-mat.stat-mech].

[4] R. F. Mohr, R. J. Furnstahl, H.-W. Hammer, R. J. Perry, and K. G. Wilson, Precise numerical results for limit cycles in the quantum three-body problem, Ann. Phys. **321**, 225 (2006), arXiv:nucl-th/0509076.

[5] T. Barford and M. C. Birse, Effective theories of scattering with an attractive inverse-square potential and the three-body problem, J. Phys. A **38**, 697 (2005), arXiv:nucl-th/0406008.

[6] S. Moroz, S. Floerchinger, R. Schmidt, and C. Wetterich, Efimov effect from functional renormalization, Phys. Rev. A **79**, 042705 (2009), arXiv:0812.0528 [cond-mat.stat-mech].

[7] S. Floerchinger, R. Schmidt, S. Moroz, and C. Wetterich, Functional renormalization for trion formation in ultracold fermion gases, Phys. Rev. A **79**, 013603 (2009), arXiv:0809.1675 [cond-mat.supr-con].

[8] A. LeClair, J. M. Roman, and G. Sierra, Russian doll renormalization group and superconductivity, Phys. Rev. B **69**, 020505 (2004), arXiv:cond-mat/0211338 [cond-mat.supr-con].

[9] K. G. Wilson, Renormalization Group and Strong Interactions, Phys. Rev. D **3**, 1818 (1971).

[10] A. B. Zamolodchikov, "Irreversibility" of the flux of the renormalization group in a 2 D field theory, JETP Lett. **43** (1986).

[11] A. LeClair, J. M. Roman, and G. Sierra, Russian doll renormalization group and Kosterlitz–Thouless flows, Nucl. Phys. B **675**, 584 (2003), arXiv:hep-th/0301042.

[12] H.-W. Hammer and B. G. Swingle, On the limit cycle for the 1/r2 potential in momentum space, Ann. Phys. **321**, 306 (2006), arXiv:quant-ph/0503074.

[13] S. D. Glazek and K. G. Wilson, Limit Cycles in Quantum Theories, Phys. Rev. Lett. **89**, 230401 (2002), arXiv:hep-th/0203088.

[14] S. D. Glazek and K. G. Wilson, Universality, marginal operators, and limit cycles, Phys. Rev. B **69**, 094304 (2004), arXiv:cond-mat/0303297.

[15] D. Bernard and A. LeClair, Strong–weak coupling duality in anisotropic current interactions, Phys. Lett. B **512**, 78 (2001), arXiv:hep-th/0103096.

[16] A. LeClair and G. Sierra, Renormalization group limit cycles and field theories for elliptic S -matrices, J. Stat. Mech. Theor. Exp. **0408**, P004 (2004), arXiv:hep-th/0403178.

[17] A. LeClair, J. M. Roman, and G. Sierra, Log-periodic behavior of finite size effects in field theories with RG limit cycles, Nucl. Phys. B **700**, 407 (2004), arXiv:hep-th/0312141.

[18] J. von Delft and D. C. Ralph, Spectroscopy of discrete energy levels in ultrasmall metallic grains, Phys. Rep. **345**, 61 (2001), arXiv:cond-mat/0101019 [cond-mat.mes-hall].

[19] F. Wegener, Flow-equations for Hamiltonians, Ann. Phys. (Leipzig) **3**, 77 (1994).

[20] S. D. Glazek and K. G. Wilson, Renormalization of Hamiltonians, Phys. Rev. D **48**, 5863 (1993).

[21] S. D. Glazek and K. G. Wilson, Perturbative renormalization group for Hamiltonians, Phys. Rev. D **49**, 4214 (1994).

[22] S. Kehrein, *The Flow Equation Approach to Many-Particle Systems*, Springer, 2006.

[23] E. Jurgenson, *Applications of the Similarity Renormalization Group to the Nuclear Interaction*, PhD thesis, Ohio State University, 2009, arXiv:0912.2937 [nucl-th].

[24] E. D. Jurgenson, P. Navrátil, and R. J. Furnstahl, Evolving nuclear many-body forces with the similarity renormalization group, Phys. Rev. C **83**, 034301 (2011), arXiv:1011.4085 [nucl-th].

[25] S. K. Bogner, R. J. Furnstahl, and R. J. Perry, Similarity renormalization group for nucleon-nucleon interactions, Phys. Rev. C **75**, 061001 (2007), arXiv:nucl-th/0611045.

[26] S. K. Bogner, T. T. S. Kuo, and A. Schwenk, Model-independent low momentum nucleon interaction from phase shift equivalence, Phys. Rep. **386**, 1 (2003), arXiv:nucl-th/0305035.

[27] W. Li, E. R. Anderson, and R. J. Furnstahl, Similarity renormalization group with novel generators, Phys. Rev. C **84**, 054002 (2011), arXiv:1106.2835 [nucl-th].

[28] W. Frank, D. Land, and R. Spector, Singular Potentials, Rev. Mod. Phys. **43**, 36 (1971).

[29] S. D. Glazek, Limit cycles of effective theories, Phys. Rev. D **75**, 025005 (2007), arXiv:hep-th/0611015.

[30] W. Glöckle, *The Quantum Mechanical Few-Body Problem*, Springer, 1983.

[31] O. Åkerlund, E. J. Lindgren, J. Bergsten, B. Grevholm, P. Lerner, R. Linscott, C. Forssén, and L. Platter, The similarity renormalization group for three-body interactions in one dimension, Eur. Phys. J. A **47**, 122 (2011), arXiv:1107.3064 [nucl-th].

[32] O. Åkerlund, J. Lindgren, P. Lerner, R. Linscott, B. Grevholm, and J. Bergsten, The Similarity Renormalization Group- for three bosons in one-dimensional momentum space, Bachelor thesis, Chalmers University of Technology, 2011.

[33] D. Furnstahl, R. Perry, and K. Hebeler, private communication (2012).

[34] W. Glöckle, G. Hasberg, and A. R. Neghabian, Numerical treatment of few body equations in momentum space by the Spline method, Zeitschrift für Physik A Atoms and Nuclei **305**, 217 (1982).

[35] L. Platter, *From cold atoms to light nuclei: The four-body Problem in an effective theory with contact interactions*, PhD thesis, Universität Bonn, 2005.

[36] A. C. Phillips, Consistency of the Low-energy Three-nucleon Observables and the Separable Interaction Model, Nucl. Phys. A **107**, 209 (1968).

[37] P. Niemann, Wenigteilcheneffekte im Medium, Diploma thesis, Universität Bonn, 2010.

[38] F. Chevy and C. Mora, Ultra-cold polarized Fermi gases, Rep. Prog. Phys. **73**, 112401 (2010), arXiv:1003.0801 [cond-mat.quant-gas].

[39] T. Paananen, J.-P. Martikainen, and P. Törmä, Pairing in a three-component Fermi gas, Phys. Rev. A **73**, 053606 (2006), arXiv:cond-mat/0603498 [cond-mat.supr-con].

[40] P. F. Bedaque and J. P. D'Incao, Superfluid phases of the three-species fermion gas, Ann. Phys. **324**, 1763 (2009), arXiv:cond-mat/0602525 [cond-mat.other].

[41] B. Errea, J. Dukelsky, and G. Ortiz, Breached pairing in trapped three-color atomic Fermi gases, Phys. Rev. A **79**, 051603 (2009), arXiv:0812.2395 [cond-mat.supr-con].

[42] G. Catelani and E. A. Yuzbashyan, Phase diagram, extended domain walls, and soft collective modes in a three-component fermionic superfluid, Phys. Rev. A **78**, 033615 (2008), arXiv:0805.3663 [cond-mat.other].

[43] D. Roscher, J. Braun, and J. E. Drut, Inhomogeneous phases in one-dimensional mass- and spin-imbalanced Fermi gases, Phys. Rev. A **89**, 063609 (2014), arXiv:1311.0179 [cond-mat.quant-gas].

[44] P. Hagen, Y(4660) in effektiver Feldtheorie, Diploma thesis, Universität Bonn, 2010.

[45] M. Peskin, D. Schroeder, *An introduction to Quantum Field Theory*, Westview, 1995.

[46] A.L. Fetter and J.D. Walecka, *Quantum Theory of Many-Particle Systems*, Dover Publications, 2003.

[47] W. Nolting, *Grundkurs Theoretische Physik 7: Viel-Teilchen-Theorie*, Springer, 2005.

[48] I.N. Bronstein, K.A. Semendjajew, G. Musiol, H. Mühlig, *Taschenbuch der Mathematik*, Verlag Harri Deutsch, 2006.

[49] P. Niemann and H.-W. Hammer, Pauli-blocking effects and Cooper triples in three-component Fermi gases, Phys. Rev. A **86**, 013628 (2012), arXiv:1203.1824 [cond-mat.quant-gas].

[50] D. Roscher and J. Braun, private communication (2014).

[51] D. Lurié, *Particles and Fields*, Interscience Publishers, 1968.

[52] W. H. Press, S. A. Teukolsky, W. T. Vetterling and B. P. Flannery , *Numercial Recipes in C*, Cambridge University Press, 1995.

[53] Reprinted from Physics Reports, Volume 428, Eric Braaten and H.-W. Hammer, Universality in few-body systems with large scattering length, Pages 259 - 390, Copyright (2006), with permission from Elsevier.

[54] N. G. Nygaard and N. T. Zinner, Efimov three-body states on top of a Fermi sea, New J. Phys. **16**, 023026 (2014), arXiv:1110.5854 [cond-mat.quant-gas].

[55] K. A. Wendt, Similarity renormalization group evolution of three-nucleon forces in a hyperspherical momentum representation, Phys. Rev. C **87**, 061001 (2013), arXiv:1304.1431 [nucl-th].

[56] T. B. Ottenstein, T. Lompe, M. Kohnen, A. N. Wenz, and S. Jochim, Collisional Stability of a Three-Component Degenerate Fermi Gas, Phys. Rev. Lett. **101**, 203202 (2008), arXiv:0806.0587 [cond-mat.other].

[57] J. H. Huckans, J. R. Williams, E. L. Hazlett, R. W. Stites, and K. M. O'Hara, Three-Body Recombination in a Three-State Fermi Gas with Widely Tunable Interactions, Phys. Rev. Lett. **102**, 165302 (2009), arXiv:0810.3288 [physics.atom-ph].

[58] T. Lompe, T. B. Ottenstein, F. Serwane, A. N. Wenz, G. Zürn, and S. Jochim, Radio-Frequency Association of Efimov Trimers, Science **330**, 940 (2010), arXiv:1006.2241 [cond-mat.quant-gas].

[59] S. Nakajima, M. Horikoshi, T. Mukaiyama, P. Naidon, and M. Ueda, Measurement of an Efimov Trimer Binding Energy in a Three-Component Mixture of ^{6}Li, Phys. Rev. Lett. **106**, 143201 (2011), arXiv:1010.1954 [cond-mat.quant-gas].

[60] E. Wille, F. M. Spiegelhalder, G. Kerner, D. Naik, A. Trenkwalder, G. Hendl, F. Schreck, R. Grimm, T. G. Tiecke, J. T. M. Walraven, S. J. J. M. F. Kokkelmans, E. Tiesinga, and P. S. Julienne, Exploring an Ultracold Fermi-Fermi Mixture: Interspecies Feshbach Resonances and Scattering Properties of ^{6}Li and ^{40}K, Phys. Rev. Lett. **100**, 053201 (2008), arXiv:0711.2916 [cond-mat.other].

[61] L. Costa, J. Brachmann, A.-C. Voigt, C. Hahn, M. Taglieber, T. W. Hänsch, and K. Dieckmann, *s*-Wave Interaction in a Two-Species Fermi-Fermi Mixture at a Narrow Feshbach Resonance, Phys. Rev. Lett. **105**, 123201 (2010).

[62] A. Trenkwalder, C. Kohstall, M. Zaccanti, D. Naik, A. I. Sidorov, F. Schreck, and R. Grimm, Hydrodynamic Expansion of a Strongly Interacting Fermi-Fermi Mixture, Phys. Rev. Lett. **106**, 115304 (2011), arXiv:1011.5192 [cond-mat.quant-gas].

[63] V. Devanathan, *Angular Momentum Techniques in Quantum Mechanics*, Springer, 2002.

[64] D.A. Varshalovich, A.N. Moskalev and V.K. Khersonskii, *Quantum Theory of Angular Momentum*, World Scientific, 1988.

Danksagung

Abschließend möchte ich mich bei allen bedanken, die mich unterstützt und zum Gelingen dieser Arbeit beigetragen haben.

Großer Dank gilt dabei Prof. Dr. Hans-Werner Hammer für die hervorragende Betreuung und insbesondere die ständige Ansprechbarkeit.

Des Weiteren möchte ich mich bei Prof. Dr. Jens Braun für die freundliche Übernahme des Koreferats bedanken.

Außerdem danke ich Prof. Dr. Jens Braun und Dietrich Roscher für die Zusammenarbeit, die mir neue Einsichten in ein spannendes Feld vermittelt hat.

Der gesamten Arbeitsgruppe danke ich für die angenehme Arbeitsatmosphäre, die ständige Hilfsbereitschaft, die physikalischen Diskussionen, die zu neuen Denkanstößen führten, sowie den interessanten Diskussionen ohne physikalischen Bezug.

Für das Korrekturlesen dieser Arbeit bin ich Dietrich Roscher, Max Jansen und Konstantin Ottnad zu besonderem Dank verpflichtet.

Erklärung zur Dissertation

Hiermit versichere ich, die vorliegende Dissertation ohne Hilfe Dritter nur mit den angegebenen Quellen und Hilfsmitteln angefertigt zu haben. Alle Stellen, die aus Quellen entnommen wurden, sind als solche kenntlich gemacht. Diese Arbeit hat in gleicher oder ähnlicher Form noch keiner Prüfungsbehörde vorgelegen.

Darmstadt, den 21. Januar 2015

(Patrick Niemann)